University of California
Santa Barbara

Using momentum-resolved optical spectroscopies to quantify anisotropic and multipolar phenomena in organic and hybrid organic-inorganic semiconductors

A dissertation submitted in partial satisfaction
of the requirements for the degree

Doctor of Philosophy
in
Physics

by

Ryan Anthony DeCrescent

Committee in charge:

Professor Jon Schuller, Co-Chair
Professor Mark Sherwin, Co-Chair
Professor Phillip Pincus

September 2020

The Dissertation of Ryan Anthony DeCrescent is approved.

Professor Phillip Pincus

Professor Mark Sherwin, Committee Co-Chair

Professor Jon Schuller, Committee Co-Chair

August 2020

Using momentum-resolved optical spectroscopies to quantify anisotropic and multipolar phenomena in organic and hybrid organic-inorganic semiconductors

by

Ryan Anthony DeCrescent

This thesis is dedicated to everybody who has supported me, including my father, mother, sister, B.S. and Ph. D. advisors, and friends.

Acknowledgements

I would like to thank everybody who has supported me — intellectually, physically, emotionally and spiritually — throughout my life. This includes, generally, old friends from my hometown and new friends in Santa Barbara who kept me on the rocks (climbing, that is). Specifically, I'd like to thank:

My father, Roland DeCrescent, who unconditionally dedicated his life to support me in all endeavors, through health or illness (of which there was much). He led by example, always holding a positive and calm attitude even in the midst of hard work.

My mother, Wendy DeCrescent, who would have done the same, but could not beyond her passing in 2006.

My Ph. D. advisor, Jon Schuller, who provided me the opportunity and freedom to experiment, and trusted me to do so. His intuition of physics and eye for succinct argumentation played a major role in my intellectual development throughout my Ph. D. education.

My lab and research partners. Steven Brown constructed the home-built Fourier spectrometer that was the primary instrument for *all* of my experimental papers. He always offered mentorship with great patience. I also worked closely with Prasad Iyer on a few "alternative" projects not discussed in this thesis. He was a seemingly endless source of unconventional ideas and proposals. While I rejected many at my best discretion, a few of them blossomed into some beautiful science papers. He urged me to think outside of the box and to keep my eyes open for new ideas. I didn't work as closely or personally with the other lab members (Tanya Das, Nikita Butakov, and Tomer Lewi), but I would like to thank them all for their patience and for setting good examples of work ethic. I also had the privilege of working very closely with members of the group of Prof. Michael Chabinyc. Prof. Chabinyc is an exceptional model of a good PI, is always

focused, is dedicated to his students' progress, and is honest about scientific knowns and unknowns. He has an awe-inspiring general knowledge of the field. Naveen Venkatesan, Dr. Clayton Dahlman, and Rhys Kennard were wonderful research partners and were absolutely instrumental in my later studies on perovskites.

Prof. Rashid Zia gracefully dedicated his time to become my second informal advisor for a short period during my work with multipolar emission from perovskites. Every conversation with him was incredibly educational, in terms of both fundamental physics and scientific etiquette.

My advising committee members (Profs. Mark Sherwin and Phillip Pincus), who enthusiastically dedicated their time to engage in intellectually stimulating discussions. They both are regular sources of the simple but critical questions.

Lab managers at the MRL (Amanda Strom) and the optical characterization facility (Alexander Mikhailovsky) for enabling much of my research also with a very positive attitude.

Professors from outside our direct collaboration circle who were willing to communicate in person or via email. This includes Profs. Chris Van de Walle, Michael Flatté, Hemamala Karunadasa, Mercouri Kanatzidis, and André Schleife.

Curriculum Vitæ

Ryan Anthony DeCrescent

Education

2020	Ph.D. in Physics (Expected), University of California, Santa Barbara.
2017	M.A. in Physics, University of California, Santa Barbara.
2014	B.S. in Physics, *summa cum laude*, University of California, Santa Cruz.

Awards/Honors

2014	*summa cum laude*, University of California, Santa Cruz.
2011	Regents Scholarship recipient, University of California, Santa Cruz.

Leadership/Teaching/Mentorship

2020	Certificate in College and University Teaching (CCUT).
2018	Instructor of Record, Phys. 110A, Introduction to Electromagnetism, University of California, Santa Barbara.
2016	Mentor for Gorman Scholar Program, University of California, Santa Barbara.
2016	Mentor for Summer Institute in Mathematics and Sciences, University of California, Santa Barbara.
2014-2017	Teaching assistant, 9 sessions total, University of California, Santa Barbara.

First and co-first author publications

1. **DeCrescent, R. A.** *et al.* Even-Parity Self-Trapped Excitons Lead to Magnetic Dipole Radiation in Two-Dimensional Lead Halide Perovskites. *ACS Nano* (2020) doi: http://dx.doi.org/10.1021/acsnano.0c03783
2. Iyer, P. P., **DeCrescent, R. A.**, Butakov, N. A., Alhassan, A., Lheureux, G., Weisbuch, C., Nakamura, S., DenBaars, S. P., Schuller, J. A., Unidirectional luminescence from InGaN/GaN quantum-well metasurfaces. Nat. Photonics (2020) doi: 10.1038/s41566-020-0641-x.
3. **DeCrescent, R. A.** *et al.* Bright magnetic dipole radiation from two-dimensional lead-halide perovskites. *Sci. Adv.* 6, eaay4900 (2020).

4. **DeCrescent, R. A.** *et al.* Optical Constants and Effective-Medium Origins of Large Optical Anisotropies in Layered Hybrid Organic/Inorganic Perovskites. *ACS Nano* 13, 10745-10753 (2019).

5. Dahlman, C. J., **DeCrescent, R. A.,**, Venkatesan, N. R., Kennard, R. M., Wu, G., Everest, M. A., Schuller, J. A., Chabinyc M. L., Controlling Solvate Intermediate Growth for Phase-Pure Organic Lead Iodide Ruddlesden-Popper $(C_4H_9NH_3)_2(CH_3NH_3)_{n-1}$
Pb_nI_{3n+1} Perovskite Thin Films. *Chem. Mater.* 31, 5832-5844 (2019).

6. Iyer, P. P., **DeCrescent, R. A.**, Lewi, T., Antonellis, N. & Schuller, J. A. Uniform Thermo-Optic Tunability of Dielectric Metalenses. *Phys. Rev. Applied* 10, 044029 (2018).

7. Brown, S. J. **DeCrescent, R. A.**, Nakazono, D. M. Willenson, S. H., Ran, N. A., Liu, X., Bazan, G. C., Nguyen, T.-Q., Schuller, J. A., Enhancing Organic Semiconductor-Surface Plasmon Polariton Coupling with Molecular Orientation. *Nano Lett.* 17, 6151-6156 (2017).

8. **DeCrescent, R. A.**, Brown, S. J., Schlitz, R. A., Chabinyc, M. L. & Schuller, J. A. Model-blind characterization of thin-film optical constants with momentum-resolved reflectometry. *Opt. Express, OE* 24, 28842-28857 (2016).

Conference Presentations

1. **Bright Magnetic Dipole Radiation from Two-dimensional Lead-Halide Perovskites.** Gordon Research Conference (Plasmonics and Nanophotonics) (2020).

2. **"Unidirectional luminescence from InGaN/GaN quantum-well metasurfaces"** in CLEO: 2020 (Optical Society of America, Washington, DC, 2020), Presentation #FTu4Q.6.

3. **Optical constants and Effective-Medium Origins of Large Optical Anisotropies in Layered Hybrid Perovskites.** MRS Spring Meeting (2020).

4. **Bright Magnetic Dipole Radiation from Two-dimensional Lead-Halide Perovskites.** APS March Meeting (2020).

5. **Momentum-resolved Spectroscopies: Optical Anisotropies and Magnetic Dipoles in 2D Lead-halide Perovskites.** Exciton Engineering in Emerging Semiconductors (E3S), Madrid, Spain (2020).

6. **Bright Magnetic Dipole Radiation from Layered Lead-Halide Perovskites.** MRS Spring Meeting & Exhibit (2019).

7. **Using Momentum Resolved Spectroscopies to Quantify Organic Semiconductor-Surface Plasmon Polariton Coupling in a Drastically Reorientable Small Molecule System.** APS March Meeting (2018).

8. **Unidirectional Luminescence from Emitting Metasurfaces.** Gordon Research Conference (Plasmonics and Nanophotonics) (2018).
9. **Resolving Morphology-Dependent Optical Properties with Momentum-Resolved Reflectometry.** APS March Meeting (2017).

Abstract

Using momentum-resolved optical spectroscopies to quantify anisotropic and multipolar phenomena in organic and hybrid organic-inorganic semiconductors

by

Ryan Anthony DeCrescent

Herein, we describe a momentum-resolved optical reflectometry technique for precisely quantifying absorption anisotropies, with a particular interest in its ability to estimate distinct *out-of-plane* dipole strengths in solution-processable semiconductors. We demonstrate major advantages over conventional techniques, e.g., variable-angle spectroscopic ellipsometry, and subsequently show how to merge the strengths of the two techniques. We interrogate two distinct material systems: organic semiconductor thin films and two-dimensional (2D) hybrid organic-inorganic perovskites (HOIPs). In organic thin films, we resolve molecular reorientations due to processing conditions. In 2D HOIPs, we adopt a layered effective medium model to show that strong optical anisotropies arise predominantly from *classical* electromagnetics effects (i.e., dielectric inhomogeneity) rather than anisotropies in the quantum-mechanical matrix elements. Finally, we demonstrate unexpected multipolar light-matter interactions in 2D HOIPs, revealed by a highly polarized and oblique emission sideband. Electromagnetic and quantum-mechanical analyses indicate that this emission originates from an out-of-plane magnetic dipole transition arising from the 2D character of electronic states. The techniques described herein are materials agnostic and may provide insight into fundamental optoelectronic processes and processing-dependent structure-function relationships in a wide variety of interrogated materials.

Contents

Curriculum Vitae **vii**

Abstract **x**

1 Introduction **1**
1.1 Permissions and Attributions 4

2 Developing a momentum-resolved reflection technique **5**
2.1 The experimental apparatus 5
2.2 Measuring the momentum distribution of polarized reflectance 6
2.3 Scaling coordinates from 'pixels' (x, y) to $\mathbf{k}_{||}$ 10
2.4 Fitting reflectance data to obtain complex optical constants 12
2.5 Multiplexing the measurement procedure for rapid data acquisition . . . 14
2.6 Conclusions 15

3 Morphology-dependent absorption anisotropies in organic thin films **17**
3.1 Introduction 17
3.2 Measurement Overview and Geometry 21
3.3 Results and Discussion 21
3.4 Summary and Outlook 28
3.5 Appendices for Chap. 3 29

4 Quantum-mechanical vs. classical origins of anisotropies in layered lead-halide perovskites **36**
4.1 Introduction 36
4.2 Results and Discussion 38
4.3 Conclusions 50
4.4 Supplementary Information 52

5 Discovering bright magnetic dipole radiation from a two-dimensional crystal **56**
5.1 Introduction 56

5.2 Results 59
5.3 Discussion 73
5.4 Supporting Information 74

6 Conclusions and Outlook **81**

A Detailed instructions for the mR technique **84**
A.1 Measurement procedure 84
A.2 Analyzing the data to extract optical constants 95
A.3 Incorporating mR fits into VASE 104

B Reflectance functions for uniaxial thin-film systems **116**

C Effective-medium model expressions **118**
C.1 Derivation of relevant expressions 118
C.2 Model parameters used for EMM calculations 124

D Radiation patterns for oriented electric and magnetic dipoles and electric quadrupoles **127**
D.1 Calculating normalized intrinsic multipolar emission rates 127

Bibliography **137**

Chapter 1

Introduction

Solution-processable semiconductors have been emphasized as promising material candidates for cost- and energy-efficient future optoelectronic technologies [1, 2]. For example, organic semiconductors can be deposited and easily incorporated into planar, and even corrugated, optoelectronic device geometries via well-established and scalable room-temperature methods, such as spin-casting, spray deposition, or blade-coating [3]. Indeed, organic light-emitting devices are already commercially available, and are currently used by several companies in cellular telephone and television displays [4]. This ease of processing, morphological control via processing conditions (e.g., choice of solvent or thermal annealing temperature) [5], and the "soft" nature of the materials are at the origin of their versatile implementation, the quintessence being, perhaps, the possibility of flexible electronics [6].

Optically, perhaps the most remarkable and unique feature of these materials, in comparison with conventional inorganic semiconductors (e.g., Si or GaAs), is their strong degree of optical anisotropy, originating from their marked structural anisotropy [7]. When implemented into optoelectronic devices, these anisotropies compound with universal polarization- and angle-dependent boundary conditions inherent to electromagnetic phe-

nomena, i.e., via Maxwell's equations. Device performance thus becomes sensitively dependent on the polarization state and wave-vector of the incident or emitted light. At a fundamental level, it is thus important to understand the inherent connection between thin film morphology and optical anisotropies.

Optical anisotropies are not unique to organic semiconductors. Indeed, in inorganic crystals, anisotropic bonding structure also leads to optical anisotropies. While these effects are typically negligible in three-dimensionally (3D) coordinated crystals, they become particularly pronounced in the limit of two-dimensional (2D) materials. In 2D materials, covalently (or ionically) bonded 2D semiconducting sheets are extended into the third dimension through weak Van der Waals forces [8]. Therefore, charge transport and optical interactions are typically mediated by electronic orbitals that are extended in the plane of connectivity, and are thus weak in the out-of-plane direction. Detailed studies of optical anisotropies thus provide valuable information about the electronic structure in these materials.

Chapter 2 provides a practical overview of the experimental apparatus and the newly developed 'momentum-resolved reflectometry' (mR) technique that is, in a sense, a major focus of this thesis. A complete description of the specific system used here is provided in the Ph. D. thesis of Dr. Steven J. Brown [9]. Therefore, Chapter 2 gives only a brief summary of the essential features of the technique, primarily for the purpose of providing context for the development of the mR technique. Detailed instructions are provided in Appendix A.

The purpose of Chapter 3 is to demonstrate the initial capabilities of our newly developed mR technique. The material systems of interest here are thin films of the organic polymer P(NDI2OD-T2). This system is of particular interest since the average molecular orientation in the solid state film can be controlled by processing conditions, taking on 'face-on' or 'edge-on' morphologies when thermally annealed below or above

the glass transition temperature ($\approx 300^\circ$ C), respectively [10, 11]. We resolve variations in the in-plane vs. out-of-plane dipole strengths between film morphologies, and argue that they originate from an out-of-plane tilt of the quantum-mechanical transition dipole moment as the average molecular orientation changes from face-on to edge-on.

Chapter 4 represents our first studies on a distinct class of material systems — the Ruddlesden-Popper phase ('layered') hybrid organic-inorganic perovskites (HOIPs). These are solution-processable bulk semiconductors with 2D optoelectronic properties. In contrast to organic semiconductors, the semiconducting regions are *inorganic*. The organic constituents in HOIPs are insulating, and therefore only indirectly influence the electronic structure through steric effects (e.g., by scaffolding the inorganic layers) [12] and by providing a non-uniform dielectric environment [13]. It comes as a surprise, then, that significant variations in the optical anisotropies are observed in these systems as the organic constituent is varied. The purpose of the study presented in Chap. 4 is to resolve the origins of these variations using the unique capabilities of mR.

In chapter 5, we demonstrate the discovery of unconventional multipolar light-matter interactions in the layered HOIP systems. Specifically, we study the momentum and polarization distribution of photoluminescence and demonstrate that a low-energy emission sideband exhibits radiation patterns that are uniquely identified as magnetic dipole in origin. Experimentally determined magnetic dipole transition rates observed in this system are approximately three orders of magnitude larger than any previously observed multipolar transition rate. We discuss potential origins and implications of this observation. Thorough understanding of the linear (electric) optical properties presented in Chap. 4 are instrumental in the quantitative analyses of this emission feature.

1.1 Permissions and Attributions

1. The content of chapter 3 has been reproduced with permission from The Optical Society: Reprinted with permission from Ryan A. DeCrescent, Steven J. Brown, Ruth A. Schlitz, Michael L. Chabinyc, and Jon A. Schuller, "Model-blind characterization of thin-film optical constants with momentum-resolved reflectometry," Opt. Express 24, 28842-28857 (2016). Copyright The Optical Society.

2. The content of chapter 4 has been reproduced with permission from The American Chemical Society: Reproduced with permission from DeCrescent, R. A. *et al.* Optical Constants and Effective-Medium Origins of Large Optical Anisotropies in Layered Hybrid Organic/Inorganic Perovskites. ACS Nano 13, 10745-10753 (2019). Copyright 2019 The American Chemical Society.

3. The content of chapter 5 has been reproduced with permission from the American Association for the Advancement of Science: Reprinted from DeCrescent, R. A. et al. Bright magnetic dipole radiation from two-dimensional lead-halide perovskites. Sci. Adv. 6, eaay4900 (2020). The Authors, some rights reserved; exclusive licensee American Association for the Advancement of Science. Distributed under a Creative Commons Attribution NonCommercial License 4.0 (CC BY-NC) `http://creativecommons.org/licenses/by-nc/4.0/`

Chapter 2

Developing a momentum-resolved reflection technique

This chapter provides a succinct conceptual overview of the momentum-resolved reflectometry (mR) technique that is, in a sense, a major focus of this thesis. A more definitive guide, primarily intended as a hands-on instructional resource for future students, is provided in Appendix A. Appendix A also includes a practical overview of the analysis used to extract complex uniaxial optical constants from the polarized momentum-resolved reflectance data.

2.1 The experimental apparatus

A majority of the results presented in this thesis were derived using a home-built momentum-resolved spectrometer. Fundamentally, momentum resolution is achievable through Fourier imaging techniques as described thoroughly in several popular text books [14] and in the succinct technical review by Kurvits *et al.* [15]. The specific experimental apparatus used in the work presented here is described in detail in the Ph. D. thesis

of Dr. Steven J. Brown [9]. Here, we will describe the system only very briefly, such that the reader can understand the development of the mR technique described in the following sections.

Essentially, the spectrometer is derived from an inverted microscope (Fig. 2.1a). Plano-convex lenses (blue) are positioned near the entrance (left in the schematic) and exit ports (bottom in the schematic) of the microscope (one such lens at each port). Each such lens images the primary objective's back focal plane (BFP) to a plane one focal-length, f, from the lens. These planes may be referred to as 'conjugate' BFPs (or Fourier planes, designated by black dashed lines in Fig.2.1a). All optical excitation and imaging is performed in these conjugate BFPs. The objective used for the studies described herein was a 100× oil-immersion objective with a numerical aperture (NA) of 1.3. While the Fourier imaging technique is not unique to this objective, an objective with NA>1 offers critical benefits that will become clear in Chap. 3.

2.2 Measuring the momentum distribution of polarized reflectance

The goal of mR is to obtain reflectance profiles as a function of the in-plane optical momentum, $\mathbf{k}_{||}$, of the incident beam. The tip of a single-mode optical fiber positioned in the conjugate BFP at the rear port of the microscope (Fig. 2.1a) approximates point-source excitation in $\mathbf{k}_{||}$-space (Fig. 2.1c), and thus to plane-wave excitation with in-plane momentum $\mathbf{k}_{||}$ at the level of the sample (Fig. 2.1b). In reality, the excitation is represented by an approximately Gaussian intensity profile in the BFP (Fig. 2.1c, inset). By mounting the fiber tip to a piezo stage, the $\mathbf{k}_{||}$ of the incident beam can be sensitively controlled, taking any value in a disk defined by $|\mathbf{k}_{||}|/k_0<$NA (Fig. 2.1c). In the previous

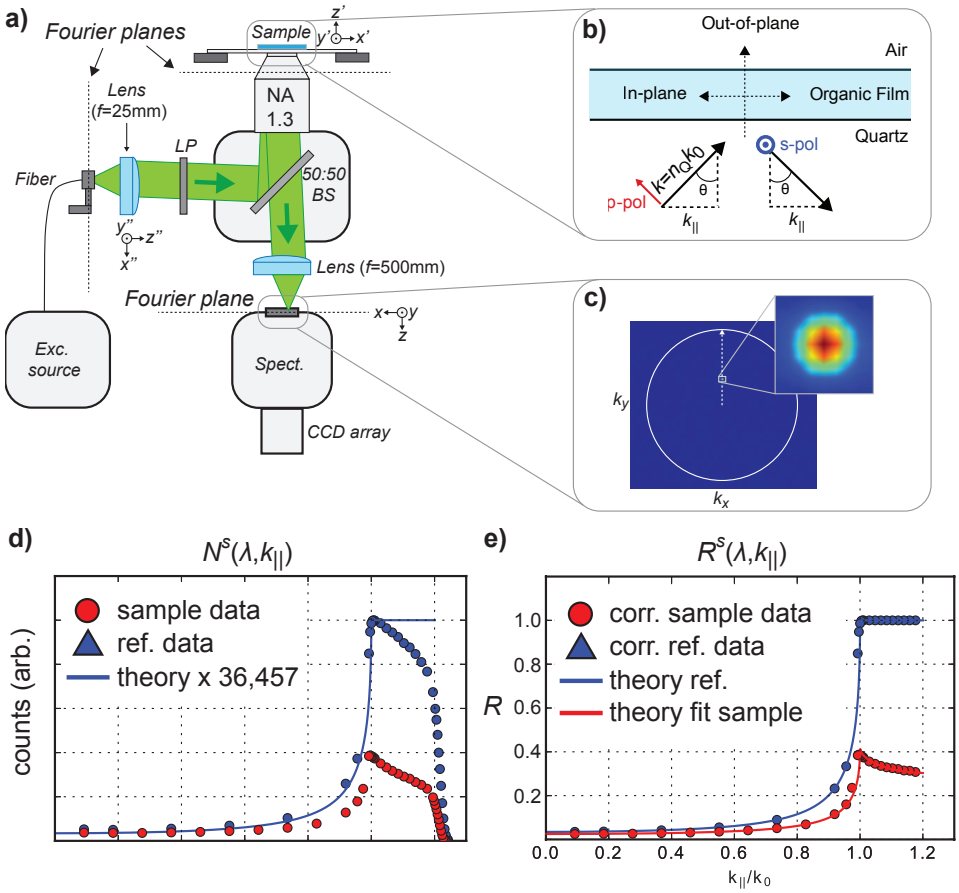

Figure 2.1: Overview of the momentum-resolved spectrometer and technique for measuring momentum-resolved reflectance. **(a)** Schematic of the system. A description is provided in the main text. Coordinate systems are provided at the input, the sample, and the spectrometer entrance to illustrate the connection between real-space and $\mathbf{k}_{||}$-space coordinates. The relevant Fourier planes are designated with black dotted lines. LP, linear polarizer. BA, beam splitter. f, focal length. CCD, charge-coupled device. **(b)** Geometry of the sample. Polarized plane waves are incident upon the sample at an angle θ (in-plane momentum $k_{||} = |\mathbf{k}_{||}|$). n_Q, substrate (quartz) refractive index. pol, polarization. **(c)** The momentum distribution of the specular reflectance as imaged at the CCD. Inset shows the magnified image of the reflected spot, with a full width at half max of approximately 3 pixels. White vertical arrow represents the k_y axis along which the excitation spot can be scanned for a complete dataset. **(d)** Example s-polarized reflectance data from (blue) a quartz coverslip reference and (red) a 46 nm thin film of organic polymer P(NDI2OD-T2) (spin-cast on an identical quartz coverslip). Blue solid line is the theoretical reflectance curve for s-polarized reflectance from a quartz-air interface, multiplied by the maximum number of s-polarized reference counts. **(e)** Proper reflectance is obtained using the correction procedure described by eqn. 2.2 on both the reference and sample. Solid lines show theory curves for (blue) the quartz-air reference and (red) the best-fit thin–film reflectance. Illustration in subpanel b and data in subpanels d-e from ref. [16].

expression, $k_0 = 2\pi/\lambda$ is the free-space momentum of an optical wave of wavelength λ.[1] The piezo stage also facilitates the focusing of the beam, i.e., proper z-positioning from the plano-convex lens such that the fiber tip lies in the BFP (e.g., Fig. 2.1c, inset). By use of the oil-immersion objective, this plane wave is incident upon the sample (from within the substrate with refractive index n_{sub}) at an angle θ such that $k_{||} = |\mathbf{k}_{||}| = n_{\text{sub}} k_0 \sin\theta$ (Fig. 2.1b). A linear polarizer ('LP' in Fig. 2.1a) is oriented with a polarization direction $\hat{\mathbf{e}}$ parallel (perpendicular) to $\mathbf{k}_{||}$ to generate a p- (s-)polarized incident beam (Fig. 2.1b). By using a super-continuum laser source, we can then control the incident wavelength, λ, in-plane momentum, $\mathbf{k}_{||}$, and polarization state of the incident beam.

The intensity of specular reflectance is measured by imaging the specular reflectance (again in Fourier space) to a charge-coupled device (CCD) array (Fig. 2.1c). At any single wavelength, by sweeping the excitation spot up the k_y axis (white arrow in Fig. 2.1c), we record the intensity of s- or p-polarized specular reflectance, $N^{s,p}_{\text{sample}}(\lambda, k_{||})$, from a thin-film sample (Fig. 2.1d, red circles).[2] An identical set of measurements is performed on a reference interface, yielding $N^{s,p}_{\text{ref}}(\lambda, k_{||})$. For example, reference data from a bare fused silica substrate is shown in Fig. 2.1d (blue circles). The reflectance function from the reference should be theoretically well known (discussed further below; Appendix B), and will be designated $R^{s,p}_{\text{ref}}(\lambda, k_{||})$. $R^{s,p}_{\text{ref}}(\lambda, k_{||})$ for a quartz-air interface is shown in Fig. 2.1d (blue solid line, multiplied by the maximum of the s-polarized reference reflectance data).

Data as acquired will be in the units (x, y, z), where (x, y) is a pixel coordinate at the level of the CCD (each being an integer between 0 and 1023) and z represents a number of counts (an integer between 0 and ≈64,000). Scaling between (x, y) and (k_x, k_y) will be described in the following section. Here we'll describe how to scale from z to proper

[1] The expression $|\mathbf{k}_{||}|/k_0$<NA, in fact, is a definition for the NA of an objective.

[2] Here, we're assuming $\mathbf{k}_{||} = k_{||}\hat{\mathbf{y}}$, and thus s- (p-)polarization has $\hat{\mathbf{e}} \perp \hat{\mathbf{y}}$ ($\hat{\mathbf{e}}||\hat{\mathbf{y}}$).

reflectance, R.

A 'correction function' $C^{s,p}(\lambda, k_{||})$ is defined by

$$C^{s,p}(\lambda, k_{||}) = R^{s,p}_{\text{ref}}(\lambda, k_{||})/N^{s,p}_{\text{ref}}(\lambda, k_{||}). \tag{2.1}$$

The correction function $C^{s,p}(\lambda, k_{||})$ is then used to scale the sample reflectance data (in units of 'counts', which depends on many experimental parameters, including excitation intensity and integration times) to proper 'reflectance' (a number between 0 and 1) by

$$R^{s,p}_{\text{sample}}(\lambda, k_{||}) = C^{s,p}(\lambda, k_{||})N^{s,p}_{\text{sample}}(\lambda, k_{||}). \tag{2.2}$$

The reference reflectance is trivially provided by a similar expression, yielding $R^{s,p}_{\text{ref}}(\lambda, k_{||})$. The correction function serves two purposes, and can be thought of as a product of two terms: one is a *constant* factor that scales counts (a number on the order of 10^4) to a number on the order of 1 (appropriate for reflectance); the other is a $k_{||}$-dependent function (of order 1) that accounts for system-dependent non-uniformity in both excitation and collection efficiencies.

Example reflectance curves are shown in Fig. 2.1e. This procedure is performed at each wavelength of interest. Care must be taken in applying the correction function to data around Brewster's angle in p-polarized reflectance (not shown here, but presented in Chap. 3), because theoretically the reflectance goes to zero there.[3] In practice, we choose to apply only the constant scale factor correction where the theoretical reflectance is greater than 0.002. Other variations of the constraints can be used with discretion. For example, in several iterations, we chose to correct data only above the critical angle of total internal reflection, defined by $k_{||} > k_0$. Care must also be taken in applying

[3]Note that this idiosyncrasy can be avoided by using a reference that has no zero in the theoretical reflectance.

the correction factor around $k_{||} = k_0$ for *both* polarizations, since the slope approaches infinity.[4] In practice, we can (and should) ignore the data, and thus the correction function, in a very small range around $k_{||} = k_0$; because the slope approaches infinity here (at least, when the system exhibits negligible losses), this region would dominate the error from which the fit is derived. (See Appendix A for more details.)

2.3 Scaling coordinates from 'pixels' (x, y) to $\mathbf{k}_{||}$

In reality, the CCD knows nothing about momentum-space coordinates; it provides a two-dimensional matrix of numbers with 'coordinates' specified by the x and y values of the pixels. The span of the BFP is represented by a disk in $\mathbf{k}_{||}$-space, $k_{||}/k_0$<NA (illustrated as a white circle in Fig. 2.1c). The physical size of this disk is governed by system parameters; the magnification of the primary objective as well as the focal length, f, of the external plano-convex lens positioned by the user [15]. E.g., for our particular setup (Nikon CFI Plan Fluor 100XS, a 100× NA=1.3 oil-immersion objective) and an external f=500 mm plano-convex, the image of the BFP at the level of the sample is approximately 0.75 cm in diameter. This spans approximately 3/4 of the full CCD array.

The center of this disk represents the origin, (k_x, k_y)=(0,0). We'll assume the user is not starting system alignment from scratch, but rather working with the system from a condition as described in ref. [9]. This center position is most conveniently located by looking for compounded internal reflections of the pin-point of light that represents the specular reflection (Fig. 2.2a). Specifically, when the specular reflection is observed close to (e.g., within ∼50-100 pixels from) the origin, a secondary reflection spot *opposite* the origin will become visible.[5] The primary and secondary reflection spots will move in synchrony as the user moves the fiber tip in the BFP. The origin (0,0) can be identified

[4] At least, in the case of weak absorption, Im($\tilde{n}$)<<1.

[5] In fact, several might become visible, but there is one 'primary' one that is most obvious.

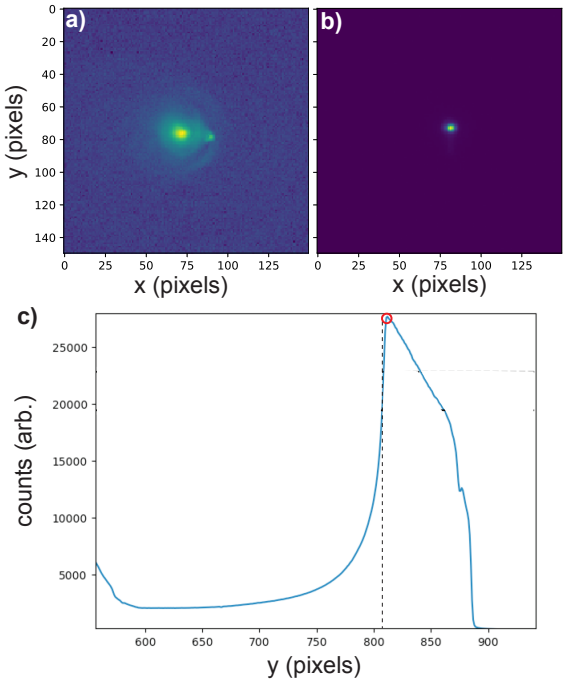

Figure 2.2: Centering and scaling the raw image **(a)** Primary specular reflection spot and secondary reflection spot, visible in a relatively narrow range around the origin of $\mathbf{k}_{||}$-space. Counts are presented in a log scale to make the secondary reflection more apparent. **(b)** Properly centered specular reflection spot. Only a single Gaussian-like peak is apparent. **(c)** s-Polarized reflection data traced along the k_y-axis (equivalently, the y-axis). The vertical dashed black line represents the y-coordinate of maximum slope, which thus represents the critical angle of TIR, $|\mathbf{k}_{||}| = k_0$. The red open circle marks the location of the maximum change of slope (i.e., maximum curvature). Theoretically this should be an infinitely sharp feature; in practice, it is smoothed by finite imaging resolution.

by moving the primary spot ever-closer to this center point so that all reflections overlap completely, giving a single Gaussian-like reflection spot at (k_x, k_y)=(0,0) (Fig. 2.2b).

At this stage, one of two coordinates necessary for a linear scaling function have been located. We need one more 'landmark'. There are two useful ones: (1) the critical angle of total internal reflection (TIR), defined by $k_{||} = k_0$, and the NA, defined by $k_{||}/k_0 = NA$. In principle, the NA would be observed as an infinitely sharp drop-off in collected intensity. In practice, however, we find that the NA is not a good reference for two reasons: the drop-off is not infinitely sharp; (2) it usually doesn't lie exactly

at the nominal NA and thus cannot be assumed to represent, e.g., $k_{||}/k_0 = 1.3$ in our case here. Therefore, I prefer to use the critical angle of TIR, since reflection curves in both polarizations exhibit a very sharp increase in reflectance there; equivalently, a discontinuity in the slope of the reflectance is observed there. Systematically, one can look for the maximum of the slope along, say, the y-axis: $\max(|R(y_i) - R(y_{i-1})|)$, where y_i is the y-coordinate of the ith pixel along the trace (Fig. 2.2c). This method is also more likely to systematically account for finite imaging resolution of the system, which serves to 'smear' ideally sharp features such as the well-defined slope discontinuity at $k_{||}/k_0 = 1$.[6]

Once these coordinates are located, one performs a linear scaling between (x, y) and (k_x, k_y). Let (x_0, y_0) be the (x, y)-coordinate of the origin, and r_c be the distance (in units of pixels) between the origin and the critical angle of TIR. The scaling functions are given simply by:

$$k_y(y) = (y - y_0)/r_c \qquad \text{and} \qquad k_x(x) = (x - x_0)/r_c \tag{2.3}$$

2.4 Fitting reflectance data to obtain complex optical constants

The s- and p-polarized reflectance data are then fit at any single wavelength to simultaneously obtain the real (Re) and imaginary (Im) components of the complex refractive index (e.g., see Fig. 2.1e). The functional form for the reflectance to which this data should be compared depends on the system in question. However, in the entirety of this thesis we will restrict our attention to the simplest possible geometry — a single

[6]The experimentally observed curve can be thought of as the theoretical profile convoluted with a Gaussian point-spread function; see Appendix A and ref. [17].

uniaxial slab between two semi-infinite media with planar (and parallel) interfaces. This is a good universal model for almost all spin-cast thin films of homogeneous media. The reflectance functions for this three-layer system are provided in Appendix A. (In Chapter 4, we will show how the results can be interpreted when the medium is not homogenous.) Therefore, $R^{s,p}_{\text{sample}}(\lambda, k_{||}; n, k)$ correspond to the polarized three-layer Fresnel reflection functions (Appendix A).

For the sake of introducing the minimum number of free parameters (two), we first fit the s-polarized data to the function $R^{s}_{\text{sample}}(\lambda, k_{||}; n_o, k_o)$ to obtain the Re and Im parts of the 'ordinary' (in-plane) complex refractive index, $\tilde{n}_o = n_o + ik_o$. Fundamentally, in mR, a unique fit for both parameters is possible since we have measured $R^{s}_{\text{sample}}(\lambda, k_{||})$ over a broad range of $k_{||}$. An exemplary s-polarized thin-film reflectance fit at a highly absorbing wavelength (further described in Chap. 3) is shown in Fig. 2.1e (solid red line). Fits for $\tilde{n}_o(\lambda)$ are obtained over all wavelengths of interest.

The p-polarized reflectance data is then fit to the function $R^{p}_{\text{sample}}(\lambda, k_{||}; n_e, k_e)$ to obtain the Re and Im parts of the 'extraordinary' (out-of-plane) complex refractive index, $\tilde{n}_e = n_e + ik_e$. By inputting best estimates for $\tilde{n}_o$ (derived from s-polarized fits), we again introduce only two free parameters (n_e and k_e) which can then, in principle, be uniquely determined. In practice, we find that the determinations for $\tilde{n}_e$ exhibit some of the challenges associated with measuring out-of-plane optical constants. In particular, the Re and Im parts of $\tilde{n}_e$ exhibit a correlated impact on the reflection function [16]. This results in large error estimates in Re(n_e), and complicates interpretation of the confidence intervals for ($\tilde{n}_e$) (see Chap. 3). However, we find that k_e (e.g., Fig. 3.6) is determined with relatively narrow confidence intervals ($\sim$5-10% in best cases), thus allowing resolution of differences in the out-of-plane absorption that were previously obscured in ellipsometry analyses on the same system [18].

Exemplary results on a specific material system — spin-cast thin films of the organic

polymer P(NDI2OD-T2) — and further details about fitting procedures, parameter correlations, and confidence intervals will be presented in Chap. 3.

2.5 Multiplexing the measurement procedure for rapid data acquisition

The mR technique as discussed so far describes point-source illumination at a single wavelength. From an 'historical' viewpoint, this process was necessary to grow intuition for the procedure and the results stemming from it. However, the process as described is very slow; one exposure must be acquired for each polarization, at each momentum coordinate, and at each wavelength of interest. Further, this must be performed on both sample and reference materials. For example, the dispersion curves to be presented in Chap. 3 (seven wavelengths, approximately 25 momentum coordinates and two polarizations each, on two distinct material samples and a reference) required approximately 1000 exposures (that is, ignoring errors and repeated measurements). This is not ideal and, in fact, not necessary. This technique may be generalized for rapid data acquisition by multiplexing over wavelength and momenta, i.e., by illuminating over all wavelengths and momenta simultaneously.

This generalization (described thoroughly in Appendix A) is quite straight-forward and requires only three modifications over the previously described technique: (1) Instead of a single-wavelength excitation from, e.g., a laser, one uses a broadband source that covers an arbitrary wavelength range of interest. This source need not be coherent; later results on perovskite films (e.g., Chap. 4) were acquired with a combination of a white-light incandescent source and a violet-blue LED. (2) Instead of fiber-tip illumination in the BFP, one 'floods' the BFP with light using a diffuser film to approximate

uniform illumination over all in-plane momenta, simultaneously. (3) The spectral dependence is accounted for by using the CCD/spectrometer in monochromator mode (i.e., by analyzing the first-order diffraction of the spectrometer), rather than looking at the 0th-order diffraction (reflection) from the spectrometer. In this case, the entrance slit of the imaging spectrometer is used to isolate reflection curves along the k_y axis, and spectral resolution is acquired in the x-dimension of the CCD. Note that this is observationally identical to the procedures described in ref. [9], except that the observed light here corresponds to specular reflection rather than photoluminescence. Data is analyzed in precisely the same way as in the point-by-point method (see Appendix A), with the benefit that combining data from multiple files is not necessary.

2.6 Conclusions

As will be described in detail in Chap. 3, the minimal number of free parameters in mR is one major benefit of the technique over conventional techniques, e.g., variable angle spectroscopic ellipsometry (VASE); in VASE, coherent combinations of s- and p-polarized reflectance are necessarily measured simultaneously. Consequently, both ordinary and extraordinary optical constants govern the polarization state of the reflected light, and must be fit simultaneously. Inherent insensitivity to the out-of-plane optical response and many correlated parameters [19] can thus lead to large errors in estimates of both the in-plane and out-of-plane optical constants.

Chapters 3-4 demonstrate the utility of mR on two distinct systems, with a specific eye on its ability to resolve variations in the out-of-plane absorption dipole strength of thin film systems. Chap. 3 focuses upon organic thin films of the n-type polymer P(NDI2OD-T2), in which variations in absorption anisotropies arise from distinct morphological changes between films thermally annealed at different temperatures. Chap. 4 focuses

upon two-dimensional (layered) HOIPs incorporating alkylammonium cations with a variety of lengths. The degree of anisotropy is observed to increase significantly as the length of the organic cation is increased. By analytically treating the significant dielectric inhomogeneity which is unique to these systems, we demonstrate that the variations arise from *classical* electromagnetics effects rather than quantum-mechanical effects. Previous reports have shown similar variations [20, 21], but the origins have yet to be succinctly explained. Our demonstration in chapt. 4 is enabled by the high-quality estimates of the anisotropic refractive index afforded by mR.

Chapter 3

Morphology-dependent absorption anisotropies in organic thin films

3.1 Introduction

Thin films are a fundamental component of modern optoelectronic devices, and have found prolific applications in industrial, military, R&D, civil, and consumer settings [22, 23, 24, 25, 26]. Knowing their optical constants is important for performance simulation and design [27, 28, 29]. To date, variable angle-of-incidence spectroscopic ellipsometry (VASE), is the predominant method for determining the optical constants of thin films [30, 31, 32, 33, 34]. (For a broad overview of the topic, see [35]). However, determination of thin film optical constants with VASE can be a complicated and difficult task for numerous reasons: (i) The analysis procedure requires the construction of complicated spectral models that may involve dozens, or even hundreds, of model parameters [36, 19]; (ii) Basic VASE analyses present high correlation of fit parameters, and thus poor or unknown reliability of fit parameters and possibly unphysical results [36, 19, 37, 38, 39]; (iii) In the thin-film limit, analyses suffer from intrinsic theoretical and experimental

sensitivity limitations [36, 40]; (iv) Incidence from air produces predominantly in-plane (IP) fields (parallel to the film interface) in the bulk of the film. This provides weak coupling to out-of-plane (OP) excitations and extraction of OP parameters suffers [19].

Although variations of the basic VASE technique (e.g., interference-enhanced, transmission-mode, total-internal- reflection, multiple-sample, etc...) can help alleviate correlation concerns and limitations associated with thin films [36, 40, 41, 42], all spectroscopic ellipsometry approaches suffer from complications associated with multi-parameter fits based on spectral models that are not known a priori. The measurements are analyzed against an unknown number of electronic models that can take a number of distinct forms (e.g. Lorentz and Gaussian oscillators, Drude, Cauchy, etc...), each of which is characterized by several free parameters. Least-squares minimization is used not only to determine the free parameters, but also to refine the model itself. As a result, determining optical constants with spectroscopic ellipsometry is time consuming, requires finesse, and produces results with unknown errors and uncertainties.

An alternative to spectral fitting is the measurement and fitting of optical properties (e.g. transmittance, reflectance) as a function of angle, rather than wavelength. In contrast to ellipsometry, a universal "Fresnel model" is employed and the system consists of a minimal number of free parameters. For instance, an isotropic film is characterized at each wavelength by just three unknowns — the film thickness, refractive index, and absorption coefficient. Such approaches may be considered "model-blind", or "deterministic", since the data is fit to a priori Fresnel reflection equations. However, the analyses used in previous angle-resolved techniques are limited to films with thicknesses on the order of a wavelength or larger; that is, researchers have inferred complex refractive indices by analyzing successive Fabry-Perot interference fringes [43, 44, 45, 46] or prism-coupled waveguide modes [47, 48, 49]. Here, we determine the complex refractive index of polymer thin films, of known thickness ($\sim$50 nm), with a high degree of certainty

using model-blind analysis of angle-resolved reflection measurements extending beyond the critical angle of total internal reflection (TIR).

Using Fourier-imaging techniques, we measure the wavelength-dependent angle-resolved reflectance from thin polymer films deposited on quartz substrates. The film thickness is determined in advance from atomic force microscopy measurements of samples co-deposited under identical processing conditions. Experiments are performed in a high-numerical-aperture (NA=1.3) imaging system, enabling measurements well beyond the critical angle, i.e. the onset of TIR. Fits of *s*-polarized reflectance measurements converge to a unique solution of the complex ordinary refractive index (n_o, E-field in the plane of the film) with quantified small uncertainty estimates. By comparing results to independent UV-Vis-NIR absorption measurements, we show that these results are substantially more accurate than optical constants determined via ellipsometry; that is, with our technique, determination of the ordinary complex refractive index is not complicated by unique out-of-plane properties. We subsequently determine the complex extraordinary refractive index (n_e, E-field perpendicular to the substrate) by performing the same procedure for *p*-polarized reflectance. These results reveal morphology-dependent optical anisotropies that are obscured in ellipsometry measurements. Analysis of parameter sensitivity and correlation (see Appendix 3.5.1 for further discussion) demonstrate the robustness of this technique and the importance of measuring reflectance beyond the critical angle. These results demonstrate a "turn-key" approach for measuring optical constants that obviates the uncertainties and modeling challenges inherent to ellipsometry.

Although the techniques described here are materials agnostic, we demonstrate our technique on films of P(NDI2OD-T2) [50, 51, 52, 53]. This material provides a good test case due to its interesting processing-dependent structural and optical properties [54]. When spin-coated from solution, the polymer molecules self-assemble into highly-

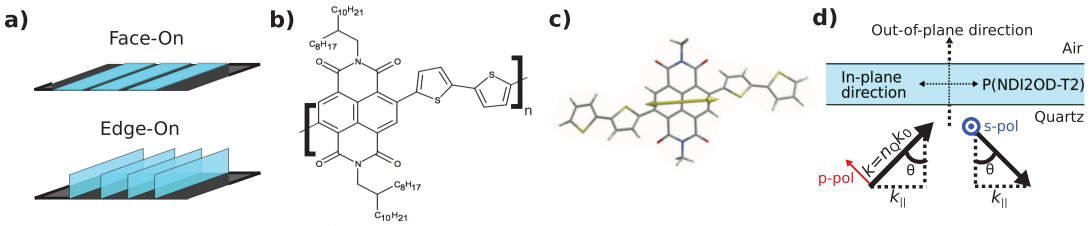

Figure 3.1: (a) 'Face-on' and 'edge-on' morphologies assumed by P(NDI2OD-T2) for low- and high-temperature thermal annealing, respectively; (b) P(NDI2OD-T2) molecule; (c) polymer segment with associated transition dipole moment; (d) the macroscopic EM system representing the sample on substrate.

ordered morphologies with molecular back-bones generally aligned parallel to the substrate surface. The molecular orientation is further influenced through thermal annealing; annealing at 150°C yields a 'face-on' morphology with the π-stacking direction perpendicular to the substrate, while annealing at 305°C yields an 'edge-on' morphology, as in Fig. 3.1(a). In both cases the optical transition dipole of this polymer is oriented mostly along the molecular back-bone, within the plane of the film (see Figs. 3.1b,c). Both morphologies thus possess uniaxial optical properties (extraordinary axis perpendicular to the substrate) with stronger polarizability and absorption along the in-plane ordinary axes. Such optical anisotropies are common to many small molecule and polymer thin films [36, 19, 55, 56, 57, 58, 59] and can significantly impact device performance and design [60, 61, 62, 63]. The ability to change molecular orientation with annealing provides a means to subtly vary optical properties of thin films without changing the molecular constituents or other system parameters. As we will demonstrate, the measurements and analysis described here can resolve these subtle differences that were not witnessed in ellipsometric studies.

3.2 Measurement Overview and Geometry

The film is interrogated via angle-resolved reflection measurements using a Nikon Eclipse Ti-U inverted microscope with a 100x/1.3 NA oil-immersion objective. Using back focal plane (BFP) imaging ('Fourier imaging') techniques [54, 64, 65, 66, 67, 68, 69], we control the incidence angle of our illumination source. Specifically, the single-mode optical fiber output of a wavelength tunable laser is placed in the BFP where it acts as a point source in Fourier space (i.e., momentum space). By translating the fiber within the BFP we control the incident momentum vector, $\vec{k}$, while a linear polarizer allows control of incident polarization. A schematic of the basic experimental geometry is shown in Fig. 3.1(d). The light is incident from the substrate and reflected back through the substrate and microscope objective. The reflected intensity is measured as a function of in-plane momentum, $k_{||}$, which relates to the incident angle, θ, within the quartz substrate according to $k_{||}=n_Q k_0 \sin\theta$, where n_Q is the refractive index of quartz (1.4553 at 700 nm) and k_0 is the free-space wave momentum. The reflection profiles are then normalized to those of a quartz-air interface at the same incident intensity in order to correct for angle- and polarization-dependent collection efficiencies in the microscope, yielding the s- and p-polarized reflectances, R_s and R_p, respectively (Fig. 2.1).

3.3 Results and Discussion

3.3.1 Determining In-Plane Optical Constants

s-Polarized reflection measurements (λ=700 nm) of bare quartz substrates (blue triangles) and substrates coated with 46nm thick PNDI2OD-T2 films (red circles) are shown in Fig. 3.2. Figure 3.2(a) corresponds to face-on (150° anneal) films and Fig. 3.2(b) to edge-on (305° anneal) films. Theoretical curves (solid lines) for the single quartz-air

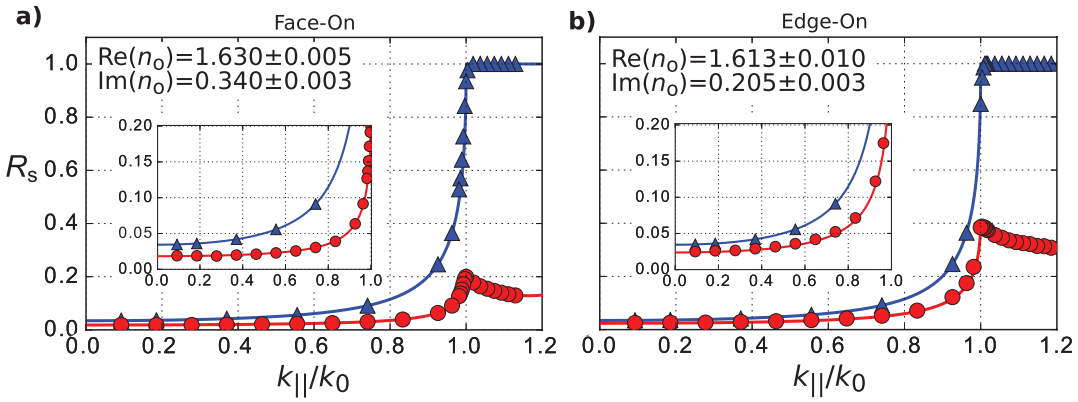

Figure 3.2: s-Polarized reflection measurements for bare quartz substrates (blue triangles) and film-on-substrate (red circles) at 700 nm for 46 nm (a) face-on and (b) edge-on films. Theoretical curves (solid lines) for single quartz-air interface (blue) and the two-interface quartz-film-air system with best-fit film index (red) are superimposed on the data. The edge-on film has a smaller absorption coefficient (Im[n_o]), manifested most evidently as higher reflectance at large momentum values ($k_{||} \geq k_0$). Best fit values for the real and imaginary parts of the ordinary index and associated 99% confidence values are displayed in the upper left hand corner of each plot.

interface (blue) and the two-interface quartz-film-air system with the best-fit film index (red) are superimposed on the data. For small momentum values (near normal incidence), the reflection coefficients with and without films exhibit small but measurable differences (inset in Figs. 3.2a,b). These differences increase substantially as the in-plane momentum approaches and then surpasses the critical angle. The reflection intensity at the critical angle ($k_{||}=k_0$) is nearly half as large for face-on films ($\sim$20%) in comparison to edge-on films ($\sim$40%), suggesting an approximately 50% larger value of the imaginary part of the refractive index. As we will discuss later, measuring and fitting the reflection intensity over this large range of momenta is critical for generating accurate, high-confidence deductions of the optical constants.

Following the procedures described in Sect. 3.2, we perform the same analysis at seven evenly spaced wavelength intervals between 500-900 nm. The wavelength range is chosen to span the low-energy absorption peak of P(NDI2OD-T2). Resulting values of the real (red, left axis) and imaginary (blue, right axis) components of the refractive index

for face-on and edge-on films are shown in Fig. 3.3(a) and 3.3b, respectively. Both films display a strong absorption band peaking near 700nm, with a corresponding "derivative" line-shape of the real part of the refractive index, as expected for a Lorentz oscillator. The face-on film exhibits a larger absorption peak and greater variation in the real part of the index as compared to edge-on films. It is important to note that fits at each wave- length are independent of each other; we make no assumptions about the nature of the electromagnetic oscillators in the material system, and the optical parameters are determined without fitting the data to a forward simulation. The experiment/fitting procedure is, in this sense, "model-blind" and produces optical constants without the use of spectral models.

Included in the plots (Figs. 3.3a,b) are 99% confidence intervals derived via the "bootstrap" method [70], assuming reasonable variations in the measured data. Those for the imaginary component lie within the scale of the data markers and thus are not visible. Confidence intervals for the imaginary part of the refractive index are generally 0.1-1% the height of the data markers; the optical constants derived here are clearly precise, but an independent measure is needed to demonstrate their accuracy. For a given set of optical constants, at each wavelength, we can produce an expected transmission spectrum based on a five-layer (air-oil-quartz-film-air) Fresnel model. These predicted transmission spectra are shown in Fig. 3.3 (red circles) for face-on (c) and edge-on (d) films. UV-Vis-NIR transmission measurements performed upon the same sample set are also displayed in Figs. 3.3c,d (blue dashed lines). To compare techniques, a unique set of optical constants for identically-prepared films (on oxidized Si substrates) was determined independently via VASE (Appendix 3.5.2) using a spectroscopic model consisting of ten Gaussian oscillators (and 35 total fit parameters). The expected transmission from ellipsometry-derived optical constants is also shown in Figs. 3.3c,d (green triangles).

Transmission values derived from our model-blind procedure show excellent agree-

ment with the measured UV-Vis-NIR data for both samples across the entire wavelength band; the derived optical constants are both precise and accurate. In contrast, our best ellipsometry results are in poor agreement with UV-Vis-NIR transmission, especially for edge-on films. Even the qualitative differences in absorptance between the face-on and edge-on films are obscured, demonstrating the complications introduced by optical anisotropies in VASE. Interestingly, the fits of ellipsometry parameters psi and delta appear quite good (Appendix 3.5.2), and reasons for the inaccuracy of the derived results are not obvious due to the complexities of the constructed model.

3.3.2 Demonstrating Uniqueness and Sensitivity to Large Momenta

The robustness of these fit results can be better appreciated by a quantitative examination of the fitting procedure. The fitting algorithm (the "trust-region reflective", TRR, algorithm [71, 72]) minimizes, within specified bounds, the sum of squared residuals:

$$S(\mathbb{R}\mathrm{e}\ n, \mathbb{I}\mathrm{m}\ n) = \Sigma_i \big[y_i - R(k_{||,i}\ ;\ \mathbb{R}\mathrm{e}\ n, \mathbb{I}\mathrm{m}\ n) \big]^2 \tag{3.1}$$

where y_i is the measured reflectance at in-plane momentum $k_{||,i}$, and $R(k_{||,i}\ ;\ \mathbb{R}\mathrm{e}\ n, \mathbb{I}\mathrm{m}\ n)$ is the predicted reflectance at $k_{||,i}$ with index values $\mathbb{R}\mathrm{e}(n)$ and $\mathbb{I}\mathrm{m}(n)$. The bounds chosen here [$1 \leq \mathbb{R}\mathrm{e}(n_o) \leq 2$ and $0 \leq \mathbb{I}\mathrm{m}(n_o) \leq 1$] include reasonable values for virtually all organic films. A 2D color map of the error function for face-on films at 700 nm is shown in Fig. 3.4(a) (edge-on films show similar behavior and an error map is presented in Appendix 3.5.1). The maps exhibit a clearly defined global minimum, and the ordinary index is consequently determined with high confidence. Local minima in the error function are prevalent in ellipsometry, and their absence here highlights another attractive feature of this model-blind approach. The precision demonstrated here results in large part from

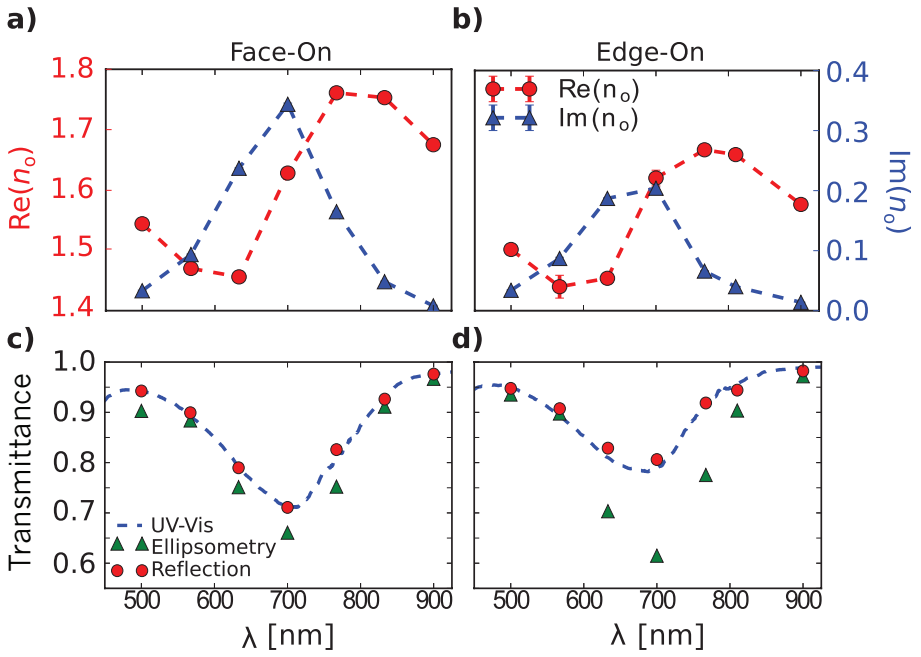

Figure 3.3: [(a) and (b)] Variation of the real (red, left axis) and imaginary (blue, right axis) parts of the ordinary index for (a) face-on and (b) edge-on films. The curves in each plot show the expected lineshapes associated with an optical absorption resonance around λ=700 nm. 99% confidence intervals are included, but those for the imaginary parts lie within the data markers and are not visible. [(c) and (d)] Normal-incidence transmission spectra through the 46 nm film on fused-silica substrate for (c) face-on and (d) edge-on films. Red circles show the prediction using values determined from R_s measurements; Green triangles show the prediction using values determined from ellipsometry; Blue dashed lines show UV-Vis-NIR transmission measurement. In agreement with the molecular model, smaller IP absorption is visible in the edge-on film, attributed to the higher OP dipole strength. This subtlety is well-resolved by our reflectometry procedure, whereas ellipsometry incorrectly suggests a larger IP absorption for edge-on films.

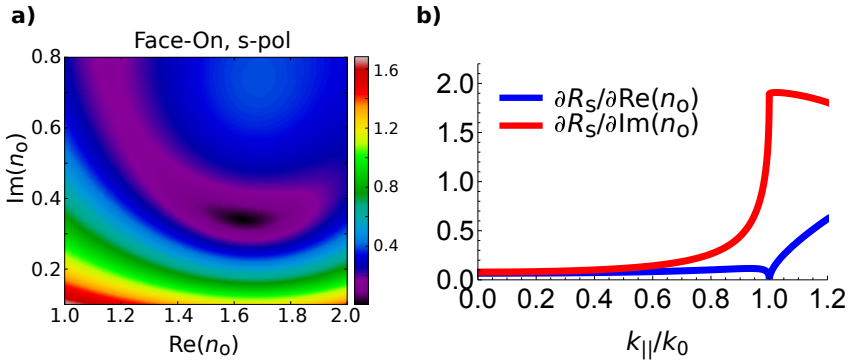

Figure 3.4: (a) 2D map of the error FOM, $\sqrt{S}$ (Eqn. (3.1)), for real and imaginary components of the ordinary index of the face-on film as fit against R_s data at 700 nm. In order to reveal details in the neighborhood of the minimum, the vertical range is limited to $0.1 \leq \mathbb{I}\mathrm{m}(n_o) \leq 0.8$ in this visualization. The specified fit bounds $[1 \leq \mathbb{R}\mathrm{e}(n_o) \leq 2$ and $0 \leq \mathbb{I}\mathrm{m}(n_o) \leq 1]$ cover index values for nearly all organic films. (b) Sensitivity of the reflection function, R_s, with respect to real (blue) and imaginary (red) components of the ordinary index, as a function of in-plane momentum, $k_{||}$. The curves are calculated at typical index values: $\mathbb{R}\mathrm{e}(n_o)$=1.5; $\mathbb{I}\mathrm{m}(n_o)$=0.2. R_s shows significantly increased sensitivity to the fit parameters for in-plane momenta beyond the critical angle of TIR. This is especially so for $\mathbb{I}\mathrm{m}(n_o)$, and thus accurate estimates of film absorption benefit significantly from measurements in the region of TIR.

the access to large momentum values afforded by the high NA imaging system. This statement is supported by numerical calculations of the partial derivatives $\partial R_s/\partial \mathbb{R}\mathrm{e}(n_o)$ (blue) and $\partial R_s/\partial \mathbb{I}\mathrm{m}(n_o)$ (red), shown in Fig. 3.4(b). The reflectance exhibits significantly increased sensitivity to both the real and imaginary parts of the refractive index for in-plane momenta near and beyond the critical angle of TIR ($k_{||}/k_0 > 1.0$). This suggests that the reliability of the angle-resolved procedure demonstrated here is greatly enhanced by accessing the region of TIR.

3.3.3 Determining Out-of-Plane Optical Constants

Measuring reflectance beyond the critical angle provides an additional advantage of great importance for analyzing organic thin-films: enhanced sensitivity to out-of plane optical properties. Resolving out-of-plane optical constants is a notorious challenge for

ellipsometry [36, 19, 55, 56, 73]. In the case of P(NDI2OD-T2), momentum-resolved photoluminescence excitation measurements demonstrate a clear difference in the optical anisotropies for face-on and edge-on films. Edge-on films exhibit a substantial increase in light emission and absorption from out-of-plane oriented dipoles [54]. One would expect an associated difference in $\mathbb{I}\mathrm{m}(n_e)$, but no such behavior is evident in our ellipsometry results (Appendix 3.5.2). To investigate the extraordinary index, we measured and fit p-polarized reflection profiles (Fig. 3.5) for (a) face-on and (b) edge-on films. The pseudo-Brewster's angle and subsequent onset of TIR are highlighted in the figure insets. The most striking difference between the two films occurs right at the critical angle, where the E-field within the thin-film is purely oriented in the out-of-plane direction [65]. Here, the face-on film exhibits nearly unity reflectance whereas the edge-on reflectance is only $\sim$84%. The associated fits reveal a significantly larger value of $\mathbb{I}\mathrm{m}(n_e)$ for edge-on films (0.09) as compared to face-on films (0.01), as expected from complementary photoluminescence studies [54]. Wavelength-dependent values of $\mathbb{I}\mathrm{m}(n_e)$ and $\mathbb{R}\mathrm{e}(n_e)$ are presented in Figs. 3.6a and 3.6b, respectively. Though the determined out-of-plane indices exhibit unexpected fluctuations and greater uncertainty, the edge-on film (blue) displays a clear increase in absorption coefficient. Indeed, the reflectance is again highly sensitive to the imaginary part the extraordinary index for in-plane momenta beyond the critical angle (see Appendix 3.5.1) and, consequently, differences in out-of-plane absorption between face-on and edge-on films are well resolved.

The determinations for n_e demonstrate some of the challenges associated with measuring out-of-plane optical constants. In particular, the real and imaginary parts of the index exhibit a correlated impact on the reflection coefficient. This results in large error estimates in $\mathbb{R}\mathrm{e}(n_e)$, and complicates interpretation of the confidence intervals for (n_e). Regardless, our model-blind approach resolves differences in n_e that were previously obscured in ellipsometry analysis, and these preliminary results suggest approaches

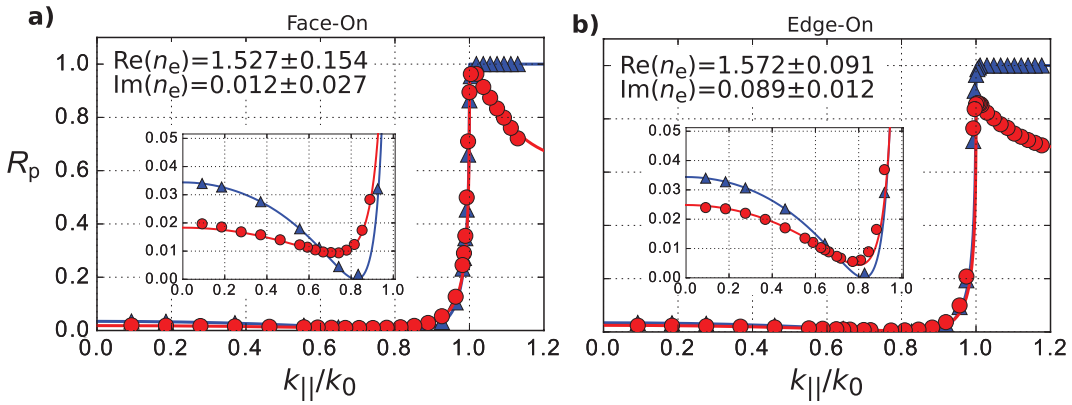

Figure 3.5: p-Polarized reflection measurements for bare quartz substrates (blue triangles) and film-on-substrate (red circles) at 700nm for 46 nm (a) face-on and (b) edge-on films. Theoretical curves (solid lines) for single quartz-air interface (blue) and the two-interface quartz-film-air system with best-fit film index (red) are superposed on the data. The enhanced OP absorption is apparent in the edge-on film, manifest as substantially lower reflectance at TIR. The inset highlights both data around the pseudo-Brewster angle. Best fit values and 99% confidence values are printed in each plot.

for future refinements and improvements of the technique.

3.4 Summary and Outlook

We have demonstrated a "turn-key" approach for the determination of the in-plane refractive index and absorption coefficient of organic thin films through model-blind fitting of momentum-resolved reflectance. Comparison with independent UV-Vis-NIR absorption experiments demonstrate high accuracy and precision, far surpassing ellipsometry results. Analysis of error maps and parameter sensitivity curves validate the fitting procedure and demonstrate the importance of measuring reflectivity beyond the critical angle. We further extend the technique and analysis to characterize the out-of-plane optical constants by analyzing p-polarized reflectance curves. We resolve subtle differences in the imaginary part of n_e for two films comprising the same molecular constituents but different morphologies, in agreement with angle-resolved photoluminescence excita-

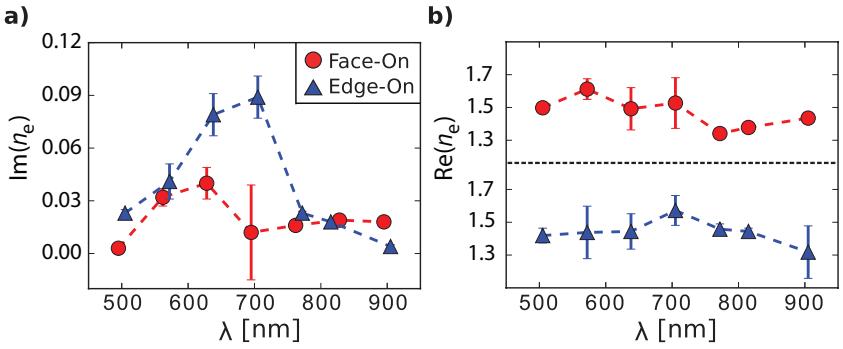

Figure 3.6: (a) The imaginary component of the extraordinary refractive index for face-on (red circles) and edge-on (blue triangles) films, determined via p-polarized reflection measurements. Though uncertainties are relatively large, the edge-on film exhibits a clear increase in OP absorption, relative to the face-on film. The wavelengths between face-on and edge-on films have been slightly offset to avoid overlapping error bars. (b) The real component of the extraordinary refractive index for face-on (red circles) and edge-on (blue triangles) films. 99% confidence bars are included in each plot.

tion measurements. In contrast to conventional analyses, our turn-key technique and analysis does not require constructing or refining complex physical models, and provides immediate model-blind results with quantifiable error estimates.

3.5 Appendices for Chap. 3

3.5.1 Appendix A: Error maps, fit sensitivities, and parameter correlation

In the main manuscript, we show a 2D map of the error figure-of-merit for s-polarized reflection at 700 nm for face-on films. The map shows a deep, unique minimum of the error within the presented bounds, justifying the use of the simple gradient-descent least-squares minimization procedure. Figure 3.7 shows an analogous map for edge-on films.

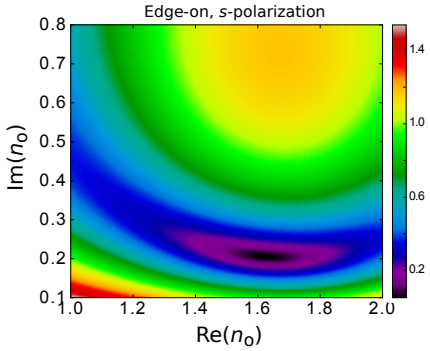

Figure 3.7: 2D map of the error FOM, $\sqrt{S}$ (Eqn. (1) of main manuscript), for real and imaginary components of the ordinary index of edge-on films as fit against R_s data at 700 nm. In order to reveal details in the neighborhood of the minimum, the vertical range is limited to $0.1 \leq \mathbb{I}\mathrm{m}(n_o) \leq 0.8$ in this visualization. A clear unique minimum exists, validating the use of the gradient-descent method.

The curvature has lessened in the $\mathbb{R}$e-direction relative to the face-on film, but a unique minimum clearly remains. It is a general trend that higher absorption leads to stronger minima, and thus $\mathbb{R}\mathrm{e}(n_o)$ is determined with higher confidence where $\mathbb{I}\mathrm{m}(n_o)$ is greater. This turns out to be true also for the extraordinary index determinations (see Fig. 3.8).

The determined real and imaginary components of the extraordinary axis exhibit relatively high uncertainty and obvious fluctuations, compared with those of the ordinary index. We gain insight into the problem by looking at the 2D error maps for real and imaginary components of the extraordinary index as fit against R_p data. These maps are presented in Fig. 3.8 for (a,c) face-on and (b,d) edge-on films at 700 nm. The maps are presented at (a,b) 'low' and (c,d) 'high' contrasts in order to show details in the neighborhood of the minima.

A unique minimum exists, but it exhibits very small curvature in the $\mathbb{R}\mathrm{e}(n_e)$-dimension. In contrast, the maps exhibit relatively high curvature in the $\mathbb{I}\mathrm{m}(n_e)$-dimension in the neighborhood of the minimum. Consequently, differences in out-of-plane absorption are well-resolved between face-on and edge-on films. However, the fits now witness a broad "valley", over which the error is minimal. This is partic-

ularly evident for face-on films (Figs. 3.8a,c) and, in general, when the out-of-plane absorption is low. Consequently, for any given estimate of $\mathbb{I}\mathrm{m}(n_e)$, the error is quite insensitive to changes in $\mathbb{R}\mathrm{e}(n_e)$ and the final determinations become extremely sensitive to measurement and calibration errors. This valley minimum is, in general, sloped in the $\mathbb{R}$e-$\mathbb{I}$m plane, and it is in this sense we say the extraordinary parameters exhibit a correlated effect upon the fit.

These statements are supported by numerical calculations of the partial derivatives $\partial R_p/\partial\mathbb{R}\mathrm{e}(n_e)$ (blue) and $\partial R_p/\partial\mathbb{I}\mathrm{m}(n_e)$(red), as presented in Fig. 3.9(a). As out-of-plane absorption increases the reflection function R_p grows more sensitive to changes in $\mathbb{R}\mathrm{e}(n_e)$. This effect is demonstrated in the inset of Fig. 3.9(a), and is also apparent upon comparison of Figs. 3.8a and 3.8b. Certainly, this is why the dispersion behavior of $\mathbb{R}\mathrm{e}(n_e)$ is much more clearly resolved in the edge-on film, and the confidence intervals in $\mathbb{R}\mathrm{e}(n_e)$ are generally smaller at the absorption peak. The sensitivity curves further suggest that determination of out-of-plane optical parameters again benefits substantially by accessing the region of total internal reflection (TIR), $k_{||}\geq k_0$. In fact, whereas R_s shows significant sensitivity to the in-plane optical parameters for all $k_{||}/k_0$ (see Fig. 4(b) of main manuscript), R_p shows negligible sensitivity for $k_{||}/k_0\lessapprox 0.98$ and sharply increased sensitivity beyond this point.

Lastly, we look at a criterion for parameter correlation between parameters $\mathbb{R}\mathrm{e}(n_e)$ and $\mathbb{I}\mathrm{m}(n_e)$ [38]:

$$C = \left| \frac{\partial R_p}{\partial\mathbb{R}\mathrm{e}(n_e)} \Big/ \frac{\partial R_p}{\partial\mathbb{I}\mathrm{m}(n_e)} \right|. \tag{3.2}$$

Parameters $\mathbb{R}\mathrm{e}(n_e)$ and $\mathbb{I}\mathrm{m}(n_e)$ are said to be correlated if C is constant over a given range of $k_{||}$; that is, changes in R_p due to variation in one parameter can be compensated by a corresponding variation in the other. Of course, C varies with $k_{||}$ and one must consider

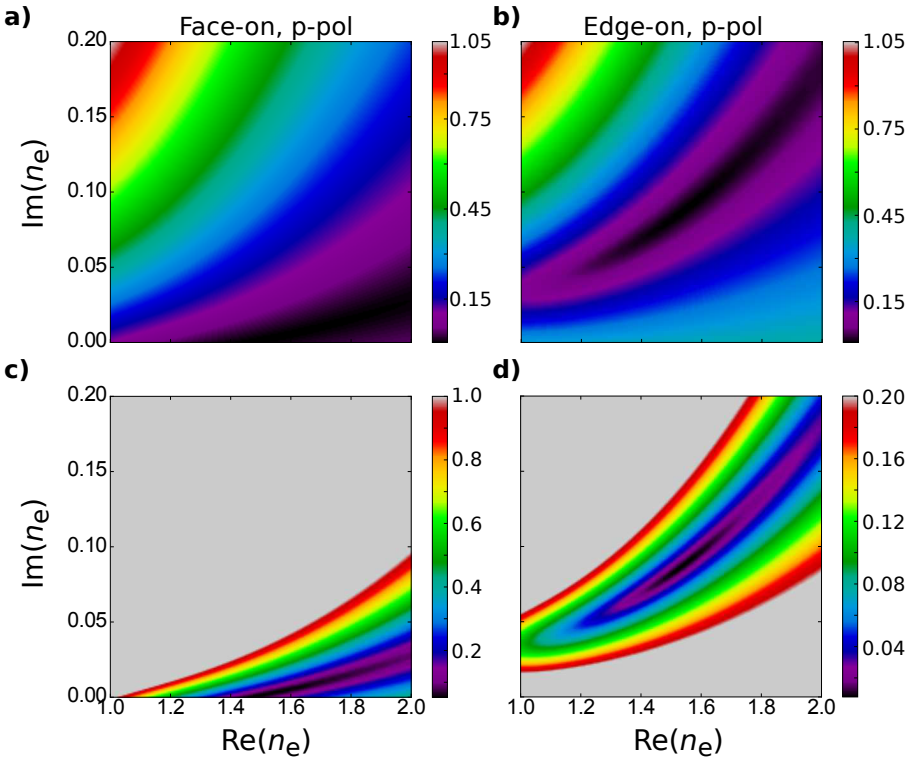

Figure 3.8: [(a) and (b)] 2D maps of the error FOM, $\sqrt{S}$ (Eqn. (1) of main manuscript), for real and imaginary components of the extraordinary index of (a) face-on and (b) edge-on films as fit against R_p data at 700 nm. [(c) and (d)] The same maps as in (a) and (b), in which values greater than a maximum value (specified by color bars) have been oversaturated (gray). This serves to show fine details in the neighborhood of the minima.

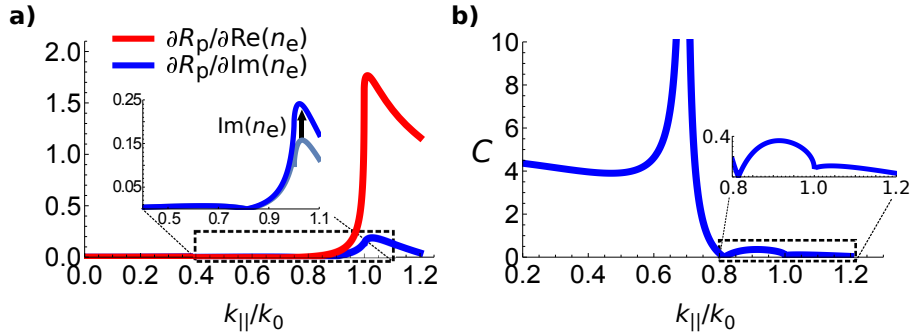

Figure 3.9: (a) Sensitivity of the reflection function, R_p, with respect to real (blue) and imaginary (red) components of the extraordinary index, as a function of in-plane momentum. The curves are calculated at typical index values: $\mathbb{R}\mathrm{e}(n_o)$=1.5; $\mathbb{I}\mathrm{m}(n_o)$=0.2; $\mathbb{R}\mathrm{e}(n_e)$=1.5; $\mathbb{I}\mathrm{m}(n_e)$=0.05. The reflectance shows drastically increased sensitivity to the fit parameters for in-plane momenta beyond the critical angle of TIR. The inset demonstrates increased sensitivity of R_p with respect to the real part of the extraordinary index in films with greater out-of-plane absorption. (b) The correlation function, C (Eqn. 3.2) as a function of in-plane momentum, again assuming typical index values specified for (a). The behavior for $k_{||}/k_0 > 1$ suggests substantial correlation between the real and imaginary components of the extraordinary index in the region of TIR.

C over the entire range of measurements. This 'correlation function', C is plotted in Fig. 3.9(b) over the angular range $0 < k_{||}/k_0 < 1.2$ and suggests that $\mathbb{R}\mathrm{e}(n_e)$ and $\mathbb{I}\mathrm{m}(n_e)$ are substantially correlated in the TIR region. Unfortunately, this region is where R_p is most sensitive to *both* OP parameters, as seen in Fig. 3.9(a). We believe this to be the reason for the "valley" in the error maps.

3.5.2 Appendix B: Comparison with ellipsometry

Figure 3.10 shows the measured ellipsometric quantities psi (blue, left axis) and delta (red, right axis) for (a) face-on and (b) edge-on films of P(NDI2OD-T2) at three unique angles of incidence. Superimposed on this data are the best-fit curves (dashed black line) resulting from the spectroscopic model. The model consists of ten in-plane Gaussian oscillators, each of which introduces three free parameters: central energy, width, and amplitude. The out-of-plane oscillators are restricted to the same energies, widths, and

relative amplitudes as the in-plane oscillators, and thus introduce a single amplitude ratio that was allowed to vary. A "UV pole" introduces two free parameters to get the real part of the refractive index in the right place. Additionally, the thickness of the film (P(NDI2OD-T2)) and substrate (SiO_2) are allowed to vary slightly around 46 nm and 200 nm, respectively. This gives a grand total of $(3 \times 10) + 1 + 2 + 2 = 35$ total fit parameters.

The resulting real (red, left axis) and imaginary (blue, right axis) parts of the ordinary (a,b) and extraordinary (c,d) refractive index are shown in Fig. 3.11 for (a,c) face-on and (b,d) edge-on films. Though the fits of delta and psi appear to be of high quality, the resulting index suggest variations between different film morphologies that are qualitatively and quantitively contrary to UV-Vis absorption, angle-resolved photoluminescence excitation, and model-blind reflectometry measurements. Specifically ellipsometry measurements suggest a smaller in-plane absorptance ($\mathrm{Im}[n_o]$) for face-on films in comparison to edge-on films. In actuality UV-Vis-NIR transmission and model-blind reflectometry display larger absorptances for face-on films. Similarly, ellipsometry measurements also suggest larger out-of-plane absorptance ($\mathrm{Im}[n_e]$) for face-on films in comparison, whereas model-blind reflectometry and momentum-resolved photoluminescence excitation [54] measurements both show the opposite trend.

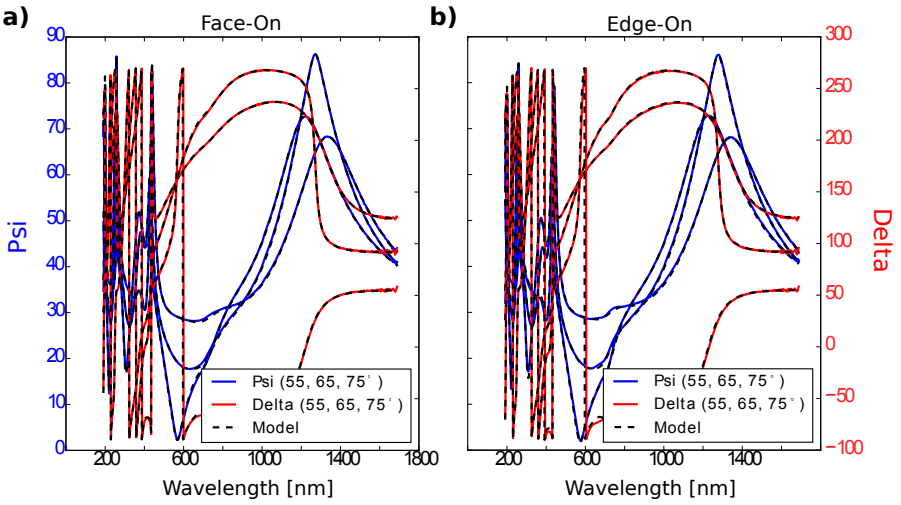

Figure 3.10: Variable-angle spectroscopic ellipsometry measurements of Psi (blue, left axis) and Delta (red, right axis) for (a) face-on and (b) edge-on films of P(NDI2OD-T2). The constructed model necessary for a quality fit introduces 35 free parameters. Though the fits of Delta and Psi appear to be very good, the quality of the model remains unknown, and we find the resulting refractive index estimations to be flawed.

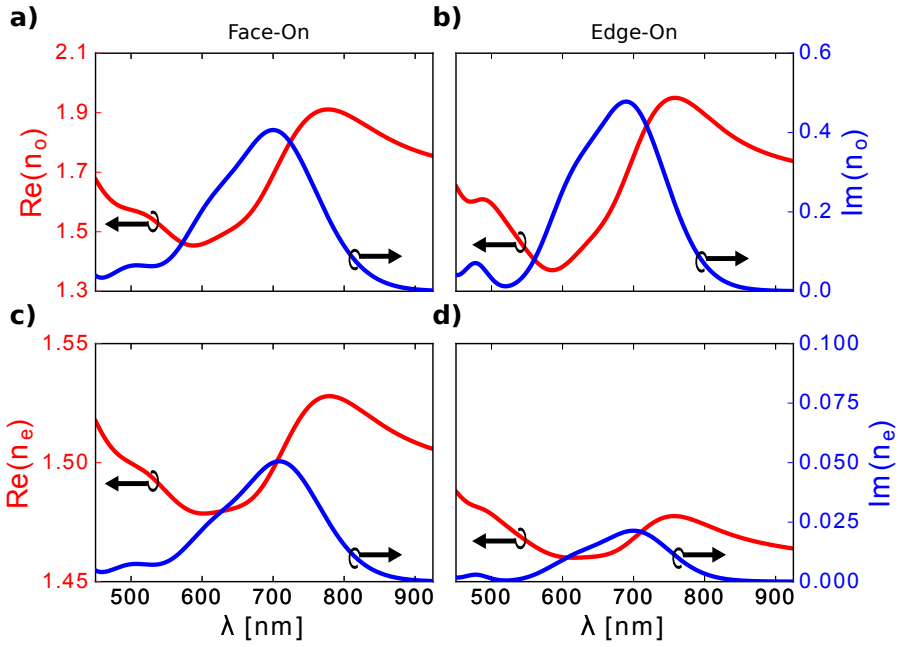

Figure 3.11: Spectroscopic ellipsometry results for the real (red, left axis) and imaginary (blue, right axis) parts of the (a,b) ordinary and (c,d) extraordinary refractive index for (a,c) face-on and (b,d) edge-on films. Contrary to UV-Vis transmission, angle-resolved photoluminescence, and our reflectometry measurements, the edge-on film shows *higher* IP absorption.

Chapter 4

Quantum-mechanical vs. classical origins of anisotropies in layered lead-halide perovskites

4.1 Introduction

When semiconductors are reduced to atomic length scales, unique optical properties emerge that reflect changes in both electronic structure and electromagnetic interactions [74, 75]. This confinement often leads to enhanced light-matter interactions, making two-dimensional (2D) semiconductors promising and versatile materials for optoelectronics [76, 77, 78]. The burgeoning class of layered hybrid organic-inorganic perovskites (HOIPs), though not atomically thin per se, are also recognized as 2D materials since carriers are confined at the atomic-scale within non-interacting semiconducting layers (*e.g.*, Fig. 4.1a) [20, 79, 80, 81]. Facile synthesis by solution-processing methods [82, 83, 84, 85], outstanding optical properties [20, 86, 87, 88, 89], and structural versatility [20, 83, 84], make 2D HOIPs attractive materials for optoelectronic and photonic

applications [90, 84, 91, 92, 93, 94]. The optical constants of 2D HOIPs have not yet been well characterized, despite being indispensable for fundamental understanding and development of optoelectronic devices.

Indeed, obtaining accurate optical constants is particularly challenging given the significant optical anisotropies common to 2D materials. Variable angle spectroscopic ellipsometry (VASE; schematically illustrated in Fig. 4.1b) — the canonical technique for characterizing thin-film optical constants [95, 96] — provides Kramers-Kronig-consistent results over a broad wavelength range between the ultraviolet and mid-infrared. However, the need for *a priori* dispersion models, a large number of correlated free parameters, and low sensitivity to the out-of-plane optical response make the determination of reliable optical constants *via* VASE an unsuspectingly difficult task [97, 7, 98]. In contrast, momentum-resolved spectroscopies offer unique advantages and have proven to be powerful techniques for quantifying optical constants and anisotropies in 2D semiconductors [99] and organic thin films [18, 16, 100]. For example, momentum-resolved reflectometry (mR; Fig. 4.1b) provides well-conditioned optical constants *via* "turn-key" approaches that obviate modeling uncertainties inherent to VASE [16, 101].

Here, we use a self-consistent combination of mR and VASE to generate continuous Kramers-Kronig-consistent optical constants with reliable estimates of the optical anisotropies. We subsequently quantify absorption and photoluminescence (PL) anisotropies in various 2D HOIP thin films, which tend to adopt highly oriented structures with semiconducting lead-iodide layers parallel to the substrate interface (*e.g.*, Fig. 4.1a) [102]. Though the electronic structure and dielectric properties of the inorganic layer are known to be weakly sensitive to the choice of the organic cation, R (Fig. 1a) [103, 104, 81], the thin-film optical response varies significantly between compounds [20, 21]. We show how these variations arise primarily from classical electromagnetic effects — rather than quantum mechanical effects — owing to dielectric inhomogeneities

inherent to this class of materials. We develop and present an effective medium model that accounts for such effects, and show how it can explain recent observations in other inhomogeneous nanomaterials, including CdSe nanoplatelets. These results provide critical optical characterizations useful for basic and applied studies of 2D HOIP optoelectronics, and more generally establish the connection between experimentally measured optical anisotropies and quantum-mechanical calculations. A complete set of optical constants for all samples studied here are provided in ref. [17].

4.2 Results and Discussion

4.2.1 Quantifying linear absorption properties

Figure 1c shows the in-plane (IP; blue) and out-of-plane (OP; red) complex permittivities, $\bar{\epsilon}_{||}$ and $\bar{\epsilon}_{\perp}$ respectively, of a butylammonium lead iodide ($(CH_3)(CH_2)_3NH_3)_2PbI_4$, henceforth $(C_4)_2PbI_4$) thin film (Fig. 4.1a; Methods). The real and imaginary components are presented in the top and bottom panels, respectively. For the spin-cast thin films studied here, experiments observe averages over crystalline grains with different IP orientations. Therefore, these measurements cannot effectively distinguish between IP anisotropies that may exist in, *e.g.*, the material's orthorhombic phase. Nonetheless, these IP anisotropies are known to be very weak relative to the IP/OP anisotropy [20] and will henceforth be ignored. A sharp IP absorption peak, seen in $\mathrm{Im}(\bar{\epsilon}_{||})$, around 510 nm originates from the 1s exciton, which is confined to the PbI layers [105, 79, 88]. The maximum of the OP absorption, $\mathrm{Im}(\bar{\epsilon}_{\perp})$, is much smaller, approximately 1/10 that of $\mathrm{Im}(\bar{\epsilon}_{||})$. These results agree well with several early experimental investigations of single-crystal 2D HOIPs which revealed a strong IP excitonic resonance with a very weak (approximately 5%) OP component [105, 20]. This strong uniaxial response has generally been

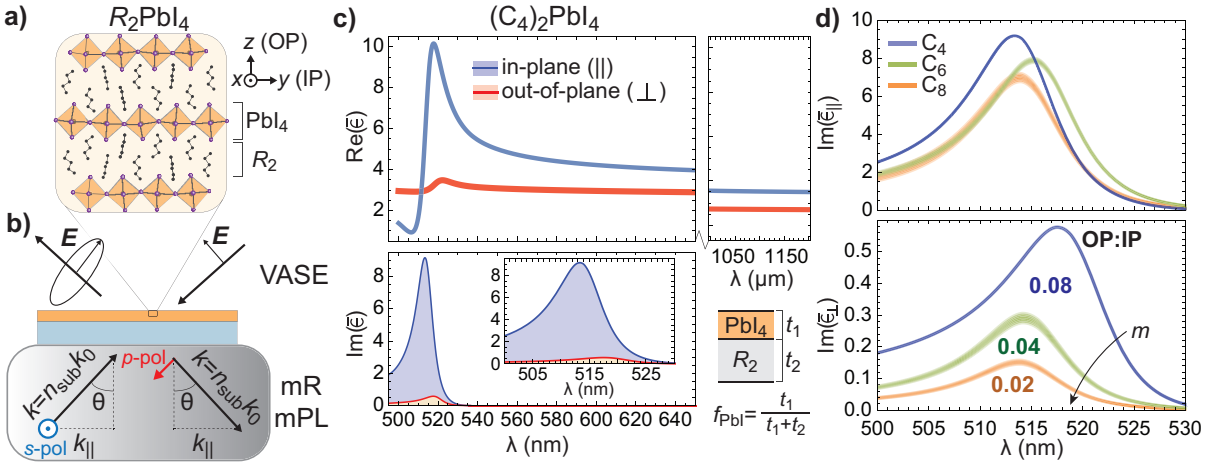

Figure 4.1: ***Quantifying variations in effective absorption anisotropies in $(C_m)_2PbI_4$ with m=4, 6, and 8.*** **(a)** Schematic crystal structure of R_2PbI_4. **(b)** Complex uniaxial optical constants of spin-cast thin films are determined by a combination of momentum-resolved reflectometry (mR; from the substrate) and VASE (from the superstrate, ambient). Momentum-resolved PL (mPL) is used to measure PL anisotropies, also from within the substrate. **(c)** Complex uniaxial permittivity of $(C_4)_2PbI_4$ (butylammonium lead iodide). In-plane (||) components are shown in blue; out-of-plane (⊥) components are shown in red. Real components are shown in the upper panel; imaginary components are shown in the lower panel. The inset shows a magnified view of of the imaginary components around the exciton absorption resonance. Schematic illustrates how the volumetric fill fraction of PbI_4 layers (f_{PbI}) depends on the length of the R cation. (Orange: PbI layers. Gray: R bilayers). **(d)** Magnified view of (upper panel) IP components, Im($\bar{\epsilon}_{||}$), and (lower panel) OP components, Im($\bar{\epsilon}_{\perp}$), for films prepared with R=C_4 (blue), C_6 (green), and C_8 (orange). Approximate ratios of integrated OP:IP absorption strengths (Table I) for each material are specified in the upper panel.

attributed to a 2D character of the exciton [106], ultimately arising from a 2D electronic structure of the metal-halide layers [107]. Associated with these absorption resonances are complementary variations in Re($\bar{\epsilon}_{||}$) and Re($\bar{\epsilon}_{\perp}$). This large absorption anisotropy produces a substantial birefringence, Δn=n_e−n_o=−0.731 where $n_{o,e}$=$\sqrt{\bar{\epsilon}_{||,\perp}}$, just below the absorption onset which settles to Δn=−0.168 in the infrared (right subpanel). Films prepared with phenethylammonium, $(C_6H_5(CH_2)_2NH_3$, henceforth PEA), exhibit an even larger birefringence, Δn=−0.836 [17].

Similar optical constants are measured for spin-cast films prepared with longer alky-

lammonium cations, R=$(CH_3)(CH_2)_{m-1}NH_3$) (henceforth C_m) with m=6 and 8 (Fig. 4.1d). For increasing R-cation length (*i.e.*, increasing m), we find a subtle but systematic decrease in the IP absorption, $\mathrm{Im}(\bar{\epsilon}_{||})$ (Fig. 4.1d, top panel). Interestingly, $\mathrm{Im}(\bar{\epsilon}_{\perp})$ decreases much more rapidly as m is increased (Fig. 4.1d; bottom panel). The ratio of the OP:IP absorption strengths, $|M_{\mathrm{IP}}|^2/|M_{\mathrm{OP}}|^2$ where $|M_{\mathrm{IP,OP}}|^2$=$\int \mathrm{Im}[\epsilon_{||,\perp}(\lambda)]d\lambda$, consequently decreases from approximately 0.08 to 0.02 as m increases from 4 to 8. Similar trends in absorption anisotropies [20, 21] and corresponding photoluminescence anisotropies [21] have been observed in previous studies, but the origins remain unresolved. Below, we show how these effects arise from classical local electric field inhomogeneties.

4.2.2 Quantifying photoluminescence properties

Momentum-resolved spectroscopies can also be used to resolve distinct IP and OP components of *emission* dipole moments. For example, momentum-resolved photoluminescence (mPL) has been used to quantify the orientation of individual molecules [108] and the average tilt angles of polymers in organic semiconducting thin films [18]. Recently, mPL has been used to quantify emission anisotropies in a variety of novel hybrid nanomaterials, including 2D HOIPs [21] and quantum-confined CdSe nanoplatelets embedded in an oleic-acid matrix [109]. In both cases, large anisotropies inferred from the mPL analyses were directly attributed to anisotropies of the band-edge wave functions of the emissive layers (*e.g.*, CdSe in ref. [109], semiconducting PbI monolayers in ref. [21]).

Experimental p-polarized momentum-resolved radiation patterns are shown in Fig. 4.2a for (blue dots) m=4, (orange dots) m=6, and (green dots) m = 8 thin-films of equivalent thickness (Methods). PL anisotropies are most evident near the critical angle of total internal reflection ($k_{||}$=k_0; Fig. 4.2b), the region into which OP (IP) dipoles

radiate maximally (minimally); the larger the suppression of PL at $k_{||} \approx k_0$, the larger the degree of anisotropy [99]. Consistent with the measured absorption anisotropies, this minimum becomes more pronounced as m increases from (blue) 4 to (green) 8, implying a decreasing OP dipole strength with increasing m. (See Supporting Information section 4.4.1 for further discussion.)

We quantify emission anisotropies by fitting the p-polarized radiation patterns to a combination of IP and OP dipoles, independently at each wavelength. Note, however, that this procedure requires accurate estimates of the anisotropic refractive index at the emission wavelengths, further motivating the need for the detailed measurements and analysis described above. Though the trend amongst materials (*vide infra*) is similar to that found in absorption, the ratios are uniformly smaller; OP:IP emission ratios in films prepared with C_4, C_6, and C_8 are found to range between $\approx$0.01 (C_8) and 0.06 (C_4). In films prepared with PEA, the ratio is found to be 0.04. While some portion of this discrepancy may arise from compounded experimental errors between input optical constants (particularly the OP components) and measured radiation patterns, analyses on different samples return similar ratios. In general, however, emission and absorption anisotropies need not be equivalent, as they arise from fundamentally distinct optical processes. Later, as for absorption, we will explore these variations in the context of classical electric field inhomogeneities.

Table I summarizes optical parameters of the materials discussed here, including films with PEA R-cations that have interlayer spacings comparable to C_6 films [110, 82] but a larger molecular polarizability.[103] Experimentally, we find a significantly larger OP optical response in films prepared with PEA (Table I). At first sight, these large variations are surprising and appear to be inconsistent with quantum-mechanical calculations that suggest nearly invariant dielectric constants of the constituent layers [103, 104]. We next show how these variations between different materials largely arise from classical

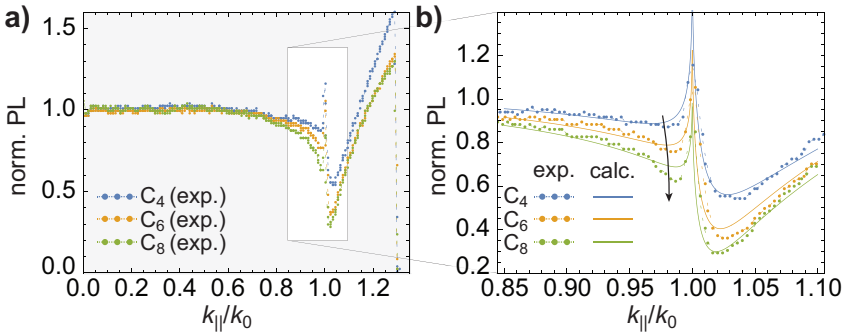

Figure 4.2: ***Quantifying variations in effective emission anisotropies in $(C_m)_2PbI_4$ with m=4, 6, and 8.*** **(a)** Experimental (normalized) p-polarized momentum-resolved PL (mPL) from 43 nm thick films of $(C_m)_2PbI_4$ with (blue) m=4, (orange) m=6, and (green) m=8. Data at each $k_{||}$-point has been integrated in energy over the emission band. **(b)** Magnified view of the data shown in subpanel (a) around the critical angle of total internal reflection ($k_{||}/k_0$). mPL counts in this region sensitively depend on both the OP emission dipole moment and the out-of-plane refractive index. Theoretical mPL counts (solid lines), calculated using optical constants for each material, demonstrate the excellent fit quality.

electromagnetic effects that can be accounted for using an effective medium model.

R cation	f_{PbI} (c-axis spacing, Å)	Norm. IP osc. strength ($\|M_{IP}\|^2$)	Norm. OP osc. strength ($\|M_{OP}\|^2$)	OP:IP strength ratio	$\epsilon_{\perp,\infty}$	n_e-n_o (λ=530 nm) [n_e-n_o (λ=1000 nm)]
C_4	0.462 (13.84)	117.1±1.6	9.03±1.00	0.077±0.010	2.85±0.01	-0.731 [-0.168]
C_6	0.391 (16.53)	108.1±2.5	3.90±0.21	0.036±0.003	2.82±0.16	-0.789 [-0.157]
C_8	0.341 (18.78)	92.0±4.5	2.01±0.10	0.022±0.002	2.76±0.25	-0.728 [-0.127]
PEA	0.390 (16.41)	101.0±2.2	10.5±0.4	0.104±0.007	2.96±0.13	-0.836 [-0.186]

Table 1: Structural and optical parameters for spin-cast thin films prepared with various R cations. Definitions are given in the main text or in Methods.

4.2.3 Deconvolving classical and quantum-mechanical anisotropies

The significant dielectric inhomogeneity inherent to 2D HOIPs sets them apart from conventional quantum-well systems comprised of III-V semiconductors [111]. Consequently, anisotropies are expected to arise at a purely classical level. Indeed, Guo *et al.*

[112] and Fieramosca *et al.* [21] acknowledged the analogy between 2D HOIPs and layered optical metamaterials [113, 114]. However, no attempt has yet been made to deconvolve these *effective* anisotropies from anisotropies *intrinsic* to the constituent layers.

The significance of this inhomogeneity is easily understood within the context of first-order perturbation theory. The transition rate, Γ_{fi}, of an electric dipole, $\vec{M}_{fi}$, at position (x, y, z) subject to a harmonic electric field of frequency ω, $\vec{E}(x, y, z; \omega)$, is expressed as [111]:

$$\Gamma_{fi} \propto | \underbrace{\vec{M}_{fi}}_{\substack{\text{quantum} \\ \text{mechanical}}} \cdot \underbrace{\vec{E}(x, y, z; \omega)}_{\text{classical}} |^2 \tag{4.1}$$

In the quantum-mechanical picture, $\vec{M}_{fi}$ is the transition dipole moment between states $|i\rangle$ and $|f\rangle$. That is, the rate of energy exchange to/from the electromagnetic field depends on the value of the *local* electric field (*i.e.*, $\vec{E}(x, y, z; \omega)$) which is, in turn, governed by the dielectric environment [115, 111, 116, 99]. This distinction is critical for comparison with quantum-mechanical calculations.

We quantify this effect in 2D HOIPs by considering two distinct (hypothetical) linear and isotropic media (Fig. 4.3a): 'medium 1' (orange; top panel) and 'medium 2' (gray; bottom pannel), with frequency-dependent relative permittivities, $\epsilon_1(\omega)$ and $\epsilon_2(\omega)$. 'Medium 1' — an "active" material — shows a strong Lorentzian resonance at a frequency ω_0 (which may represent, *e.g.*, an exciton) with $\epsilon_1 < 0$ behavior over a small domain on the high-frequency side of the resonance. In stark contrast, 'medium 2' — a "passive" material' — has a relatively small permittivity and is completely transparent over this range, thus exhibiting negligible dispersion. Medium 1 and 2 are reasonable models for, *e.g.*, the metal-halide and organic spacer layers in 2D HOIPs, respectively [103, 112, 104]. At the interfaces (Fig. 4.3b), the parallel-to-interface ($||$) and perpendicular-to-interface

($\perp$) electric field matching conditions are distinct; $E_{||}$ (blue) is continuous across the interface while $E_{\perp}$ (red) exhibits a sharp discontinuity according to (Supporting Information S4)

$$E_{||}(z' = 0^-) = E_{||}(z' = 0^+)$$
$$\epsilon_1 E_{\perp}(z' = 0^-) = \epsilon_2 E_{\perp}(z' = 0^+). \tag{4.2}$$

A material composed of many such alternating layers (Fig. 4.3c; top panel) can be structurally described by the volumetric fill fraction of medium 1: $f_1{=}t_1/(t_1 + t_2)$ where t_i (i=1,2) is the layer thickness of medium i. If the alternating layers are each much thinner than the optical wavelength, the composite material can be optically described with *effective* parallel ($\bar{\epsilon}_{||}$) and perpendicular ($\bar{\epsilon}_{\perp}$) permittivities according to basic constitutive relations [117]. Given the differences expressed in Eqn. 4.2, the *effective* parallel and perpendicular optical constants represent different averages. Generalizing Eqn. 2 to account for *intrinsically* uniaxial constituents, each with permittivity tensors $\epsilon_i{=}\text{diag}(\epsilon_{i,||}, \epsilon_{i,||}, \epsilon_{i,\perp})$ (i=1,2), we arrive at (Supporting Information S4):

$$\bar{\epsilon}_{||} = f_1\epsilon_{1,||} + (1 - f_1)\epsilon_{2,||}, \qquad \bar{\epsilon}_{\perp} = \frac{1}{f_1/\epsilon_{1,\perp} + (1 - f_1)/\epsilon_{2,\perp}}. \tag{4.3}$$

At this level of description, the layered material is now effectively homogeneous, but uniaxial with an *effective* permittivity tensor $\bar{\epsilon}{=}\text{diag}(\bar{\epsilon}_{||}, \bar{\epsilon}_{||}, \bar{\epsilon}_{\perp})$ [117]. Figure 4.3c (bottom panel) shows the *effective* IP (blue) and OP (red) permittivities calculated for our hypothetical layered medum with f_1=0.5. This crystal exhibits a uniaxial optical response markedly different from that of either bulk constituent. The IP optical response is reduced slightly due to volumetric averaging between active and passive layers. More noticeably, the OP optical response is reduced significantly due to suppression of the

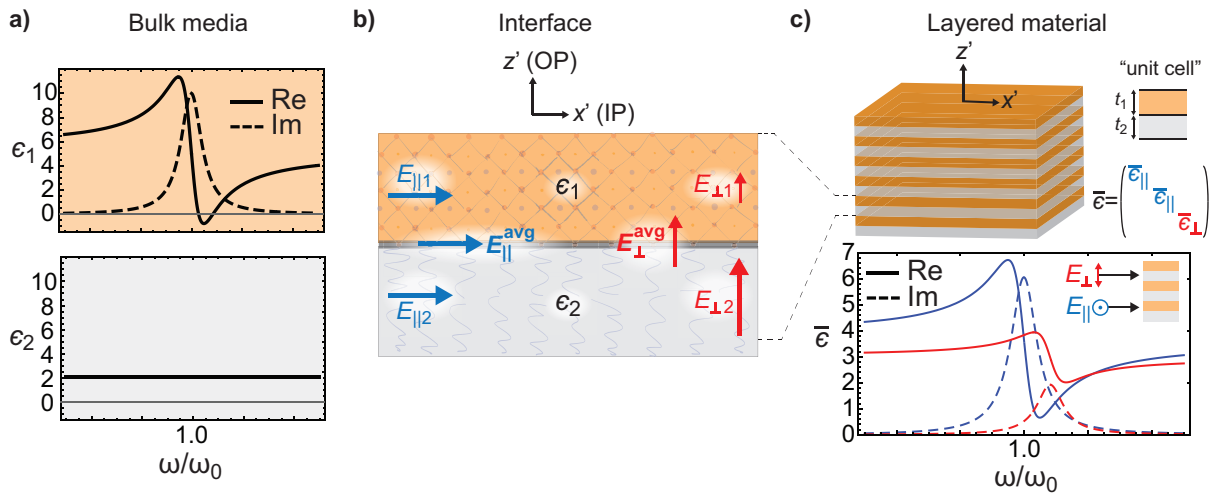

Figure 4.3: ***Origin of large effective optical uniaxiality in layered nanomaterials.*** **(a)** Permittivities of two hypothetical isotropic dielectric media. 'Medium 1' (top; orange) shows a strong Lorentzian resonance at a frequency ω_0. 'Medium 2' (bottom; gray) is completely transparent (Im(ϵ_2)=0) and thus exhibits negligible dispersion. **(b)** Electric field matching conditions at the level of a single dielectric interface. The in-plane electric field (blue) is continuous across the interface. The out-of-plane electric field (red) exhibits a discontinuity because of the dielectric contrast and is suppressed in the high-permittivity medium. **(c)** A layered system is thus optically uniaxial even when the material constituents are isotropic. The calculated permittivities in (c) assume a fill factor, f_1, of 0.5 (*i.e.*, $t_1/(t_1+t_2)$=0.5).

local perpendicular electric field, $E_\perp$ (Eqn. 4.2), within the absorbing regions due to their relatively high local permittivity. Although the absorbing medium is isotropic at an *intrinsic* level, the layered medium acquires a significantly anisotropic *effective* optical response.

Optical experiments invariably measure the *effective* optical properties of layered HOIPs. Using the effective medium model (EMM) described above, however, we can gain a better understanding of the *intrinsic* optical properties. For instance, the decrease in $\mathrm{Im}(\bar{\epsilon}_{||})$ can be predicted from a decrease in the volumetric fill fraction of PbI layers (f_{PbI}). Similarly, large measured anisotropies arise from field inhomogeneities described in Eqn. 4.2. To facilitate comparison between experiment and quantum-mechanical calculations, we exploit Eqn. 4.3 to extract the *intrinsic* optical constants, $\epsilon_{||}^{\mathrm{int}}$ and $\epsilon_{\perp}^{\mathrm{int}}$, from measured optical constants, $\bar{\epsilon}_{||}$ and $\bar{\epsilon}_{\perp}$. Namely, we equate the right-hand side of the EMM expressions (Eqn. 4.3) to the measured optical constants, input known structural parameters, and solve for the intrinsic optical constants of the PbI monolayers (Methods). Because of the vertically layered thin-film structure of $R_2\mathrm{PbI}_4$, equations relating IP ($||$) and OP ($\perp$) expressions can be solved independently. Exemplary *intrinsic* PbI optical constants resulting from this calculation are presented in Fig. 4.7. The results indicate an *intrinsic* OP:IP absorption strength ratio of approximately 0.3, as compared to 0.08 inferred from thin films directly. That is, anisotropies in the quantum-mechanical matrix elements reduce the OP dipole strength by only a factor of $\approx$1/3; in contrast, classical electric field inhomogeneities play a larger role, leading to a further reduction by a factor of $\approx$1/4, and even larger factors in films prepared with longer organic cations. This suggests the simple route to tuning significantly the macroscopic optical anisotropies, *i.e.*, by varying the length and polarizability of the organic cation. The corrected $(\mathrm{C}_4)_2\mathrm{PbI}_4$ high-frequency OP permittivity ($\epsilon_{\perp,\infty}^{\mathrm{int}}\approx$4.1 for λ>1000 nm; Fig. 4.7) can now be compared directly to calculations in refs. [103, 104] and both are found to

be in very good agreement. The high-frequency IP permittivity ($\epsilon^{\text{int}}_{||,\infty}$≈4.7) is most easily compared to the 3D system $(C_1)PbI_3$. Although the IP bonding structure of R_2PbI_4 is similar to that of $(C_1)PbI_3$, atomic-scale continuity with neighboring low-permittivity organic layers should suppress the dielectric constant relative to bulk values. We thus conclude that the EMM as developed here accurately described the relationship between experimentally observed (*i.e.* effective) and theoretically predicted (*i.e.* intrinsic) optical anisotropies.

Though Eqns. 4.2-4.3 hold independently at each wavelength, we simplify subsequent analyses by deriving (for each material) a single wavelength-averaged correction factor that account for the EMM effects (Supporting Information S5). The relations are particularly simple for the vertically layered thin-film structure of R_2PbI_4; the OP dipole strength ($|M_{\text{OP}}|^2$) correction depends on the dielectric contrast and (implicitly) the volumetric fill fraction of PbI layers:

$$|M^{\text{int}}_{\text{OP}}|^2 = \langle|\epsilon^{\text{int}}_{\perp}/\bar{\epsilon}_{\perp}|^2\rangle \times |M_{\text{OP}}|^2 \tag{4.4}$$

in which $\langle\rangle$ denotes spectral averaging over the absorption (or emission) band (Methods). As before $\bar{\epsilon}_{\perp}$ is the *effective* OP permittivity of the crystal. Note that $\epsilon^{\text{int}}_{||,\perp}$ corresponds to the material in which the absorption or emission process is localized (*e.g.*, the PbI layers in 2D HOIPs). To evaluate these correction factors, the dielectric and structural properties of the material constituents must be known. To this end, we use $\epsilon^{\text{int}}_{||,\perp}$ derived from the procedures described in the previous section (Fig. 4.7).

Figure 4.4 summarizes absorption (left panel) and emission (right panel) anisotropies inferred directly from thin-film measurements ("effective"; orange markers) and after applying EMM corrections ("intrinsic"; purple markers) for all of the materials studied here. The inferred anisotropies in the PbI layers are uniformly smaller than in the

homogenous layered medium. Notably, after accounting for variations in length and permittivities of the organic layers, we find a similar degree of absorption anisotropy (OP:IP ≈0.3) between films prepared with C_4, C_6, and PEA. Films prepared with C_8 still show a relatively small OP:IP ratio (≈0.12) after this correction, which likely results from experimental errors, particularly in the OP optical constants. Since emission and absorption correction factors are (nearly) equivalent, relatively small *effective* OP:IP ratios lead to correspondingly small *corrected* ratios. Interestingly, residual variations are found in emission ratios but are absent in absorption ratios. Some portion of this discrepancy may arise from compounded experimental uncertainties; the inferred OP dipole strengths are particularly sensitive to the input optical constants. The results also depend upon the assumed distribution of emitter positions within the film (Methods). However, to what degree this discrepancy arises from experimental artifacts or inherent differences in optical processes remains unresolved at the current time. For comparison, we also include values from ref. [21] (down triangles) before and after applying corrections derived here. (Note that ref. [21] quotes OP percentages; here we have converted to OP:IP ratios.) Though absolute values differ between that work and ours, the trend between materials agrees well. We suspect ratios derived in ref. [21] are overestimated since effective values are significantly larger than those inferred here and in ref. [20], and since corrected values are very large (exceeding 1 in the case of m=4).

Leveraging this analysis, we can now quantify and understand optical anisotropies in films of butylammonium methylammonium lead iodide, $(C_4)_2(C_1)_{N-1}Pb_NI_{3N+1}$, with N>1, which tend to consist of statistical mixtures of oriented crystallites (Supporting Information S5) [102, 118]. The corrections described in Eqn. 4 can be extended to account for this crystallite reorientation (Supporting Information S4 and S5). Similar EMM treatments have successfully been applied to quantify the role of anisotropic intrinsic carrier mobilities in ensembles of conducting oxide nanocrystals [119]. Interestingly, for both

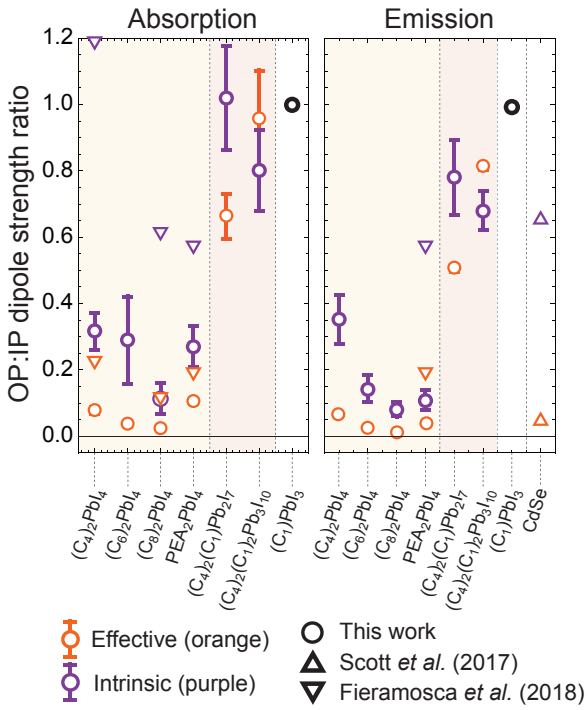

Figure 4.4: ***Summary of effective vs. intrinsic anisotropies in layered nanomaterials.*** Orange markers: *Effective* OP:IP ratios for various materials determined in (circles) this work, (up triangles) Ref. [109], and (down triangles) ref. [21]. Purple markers: *Intrinsic* OP:IP ratios calculated by techniques described in the main text. Error bars represent estimates of 99% confidence intervals, primarily originating from uncertainties in optical constants. Absence of error bars indicates no confidence estimate or confidence intervals approximately equivalent to marker sizes.

N=2 and N=3 HOIPs, we find nearly isotropic absorption and emission after accounting for EMM effects, which likely reflects "new" Pb and I p_z orbital contributions in the bonding structure that are highly suppressed in the limit of the monolayer system [107, 120]. We note, however, that phase intergrowth in the thin-film structure for N>1 may reduce the applicability of the model derived here [118].

4.3 Conclusions

The EMM derived here can be immediately applied to other material systems with layered geometries. For example, we consider previous mPL analyses of CdSe nanoplatelets as studied by Scott *et al.* [109] In that work, monolayers of highly oriented CdSe nanoplatelets were immersed in an oleic-acid matrix and deposited on transparent substrates. As per typical mPL analyses, radiation patterns were modeled using a three-layer Fresnel model with *effective* (*i.e.*, homogeneous and uniaxial) optical constants (see Supplementary Tables I-II of ref. [109]). Within that model, observed radiation patterns correspond to an *effective* OP contribution of 5% (OP:IP ratio of 0.052) (Fig. 4, orange up triangle). However, at a more rigorous level, these radiation patterns arise from a five-layer system (Fig. 4.8). This is indeed an analytically tractable problem, using the same formalism as presented in previous reports [116, 99, 109], but extended using electric fields calculated for a five-layer model [121]. These calculations reveal that radiation patterns observed in ref. [109] correspond to an *intrinsic* OP contribution of 41% (OP:IP ratio of ≈0.66) (Fig. 4, purple up triangle), an order of magnitude larger than that inferred by Scott *et al.* [109] This discrepancy is captured very well using the simple correction factors described above ($|\epsilon_{\perp}^{\mathrm{int}}/\bar{\epsilon}_{\perp}|^2$=$|(7.9+i2.6)/(2.332+i0.026)|^2$≈12.7), further validating the simplified procedure described in this work. Indeed, this corrected ratio is more compatible with emission anisotropies observed in III-V quantum-well sys-

tems [122, 123], in which the effects of dielectric inhomogeneity are minimized, and in other CdSe nanoplatelet [124] and nanowire studies [125].

Knowledge of the *effective* optical properties is suitable for understanding, *e.g.*, angle-dependent reflection, transmission and absorption rates. The optical constants reported here will thus be useful for modeling and optimizing 2D HOIP-based optoelectronic devices. These macroscopic optical properties, however, do *not* directly reflect the properties of the material constituents; classical corrections must be applied before attributing the optical properties to the underlying electronic structure and anisotropies in the quantum-mechanical transition dipole moment. We show how these differences can be simply accounted for using correction factors derived from an effective-medium model. In particular, in OP-layered nanomaterials, quantum-mechanical OP dipole moments are substantially underestimated — by a factor of approximately 5 or greater in 2D HOIPs — when ignoring dielectric inhomogeneties. In the most significant case considered here (CdSe nanoplatelets), we have shown that inferred quantum-mechanical anisotropies were overestimated by approximately a factor of 10. After accounting for such effects, absorption anisotropies in 2D HOIPs are found nearly independent of the choice of the R cation. This study illustrates how experimentally inferred optical anisotropies relate to quantum-mechanical calculations in any material, and offers an intuitive explanation for previously unexplained variations in optical properties of 2D HOIPs. Our model may also provide guidelines for predicting and designing birefringence properties in layered compounds.

4.4 Supplementary Information

4.4.1 Further details about mPL analysis

To understand the significance of dielectric inhomogeneity on the emission processes in HOIPs, we prepared thin films of $(C_m)_2PbI_4$ (m=4, 6, and 8) with equivalent thicknesses (up to experimental accuracy, limited by imaging resolution of atomic force microscopy and thin-film surface texture; Methods). Experimental p-polarized radiation patterns are shown in Fig. 4.5a for (blue dots) m=4, (orange dots) m=6, and (green dots) $m = 8$ (identical to data presented in manuscript). For films with equivalent thickness, variations in the radiation patterns solely reflect changes in the dipole orientation and dielectric environment surrounding the Pb-I layers [17]. Namely, *for a constant OP dipole strength*, a decrease in the PL counts around $k_{||} \approx k_0$ is expected to follow the decrease in n_e as m increases from (blue) 4 to (green) 8 (Fig. 4.6). This prediction (assuming a *constant* OP dipole strength over all values of m) is shown as solid lines in Fig. 4.5b (color corresponding to experimental markers). (Note that these calculations are different than those presented in the manuscript. Calculations in the manuscript represent fits to each material.) The experimental PL, however, shows a substantially *steeper* fall-off (compared to calculations) as m increases. We thus immediately infer a decreasing OP dipole strength with increasing m, as observed in absorption measurements. This decrease is quantified by fitting of the OP and IP emission dipole strengths independently at each wavelength. Fig. 4.5c shows the IP (blue) and OP (red) dipole *moments* extracted from fits at each wavelength. Integrated OP:IP emission dipole *strength* ratios are printed as bold text in each subpanel.

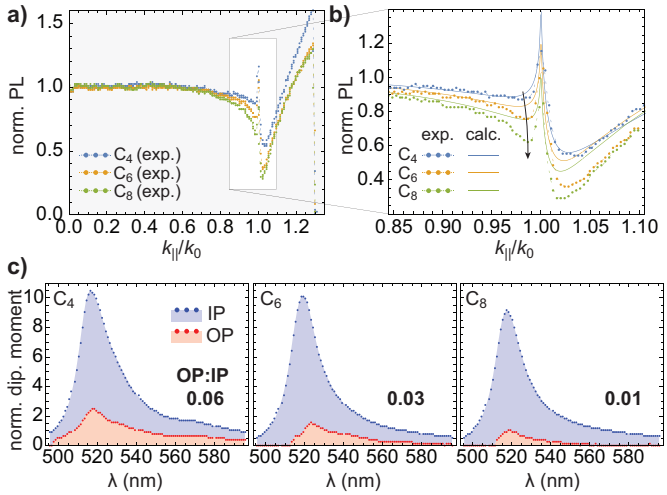

Figure 4.5: ***Further details about mPL analysis.*** **(a)** Experimental p-polarized mPL from 43 nm thick films of $(C_m)_2PbI_4$ with (blue) m=4, (orange) m=6, and (green) m=8. **(b)** Magnified view of the data shown in subpanel (a) around the critical angle of total internal reflection ($k_{||}/k_0$). Solid lines are calculations assuming a constant OP:IP emission dipole strength ratio. **(c)** IP (blue) and OP (red) dipole *moments* extracted from fits at each wavelength. Integrated OP:IP emission dipole *strength* ratios are printed as bold text in each subpanel.

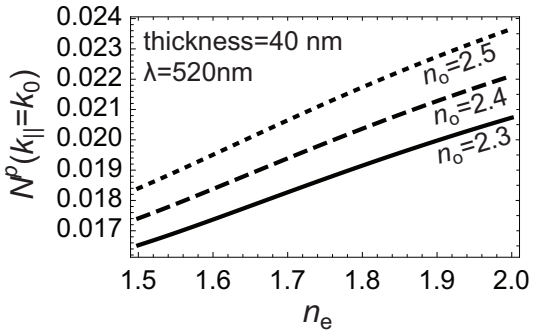

Figure 4.6: ***Variation of predicted counts at $k_{||}=k_0$ with variations in n_e and n_o.*** Calculated (normalized) p-polarized PL counts at $k_{||}=k_0$ for a 40 nm thin film and a constant OP:IP emission strength ratio (0.05). PL is expected to decrease at $k_{||}=k_0$ with both n_o (specified in text) and n_e (horizontal axis).

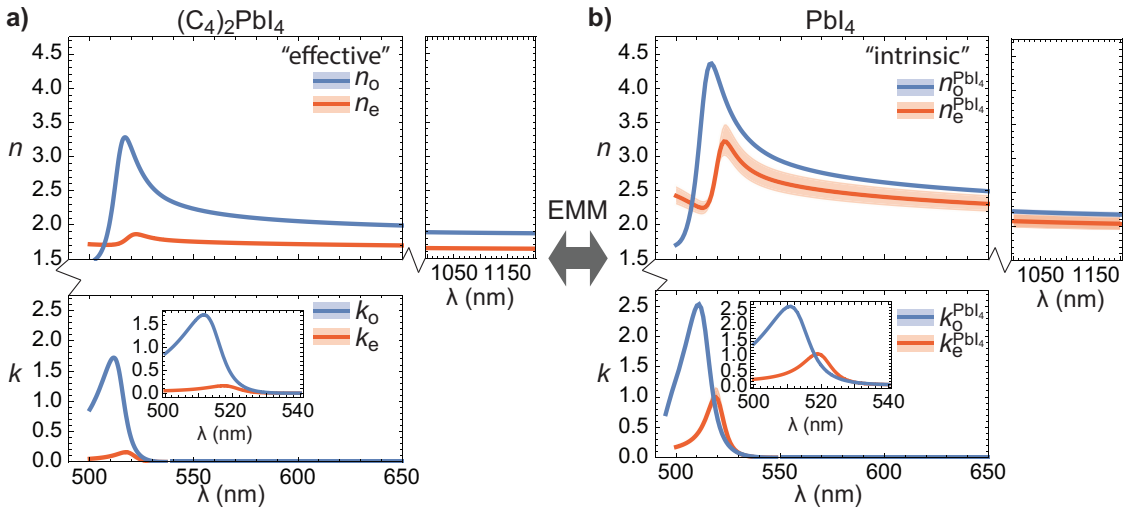

Figure 4.7: ***Effective vs. intrinsic optical constants of $(C_4)_2PbI_4$.*** The complex uniaxial refractive indices of **(a)** $(C_4)_2PbI_4$ thin films (*i.e.*, "*effective*" optical constants) and **(b)** of the constituent PbI_4 monolayers (*i.e.*, "*intrinsic*" optical constants). The ordinary (IP) components are shown in blue; the extraordinary (OP) components are shown in red. Here we have used the relationship $n_o^{PbI_4}=\sqrt{\epsilon_{||}}$ and $n_e^{PbI_4}=\sqrt{\epsilon_{\perp}}$ The real components (n_o, n_e) are shown in the upper panels; the imaginary components (k_o, k_e) are shown in the lower panels. The *intrinsic* optical constants were determined by equating Eqns. C.15-C.16 to the measured thin-film optical constants and solving for the optical constants of the PbI_4 layers independently at each wavelength. Filled colored regions represent the range of values obtained using the approximate $\pm 3\sigma$ ranges. We assume an isotropic refractive index of 1.5 for the organic spacer layers, as recently calculated by Traore *et al.* [104].

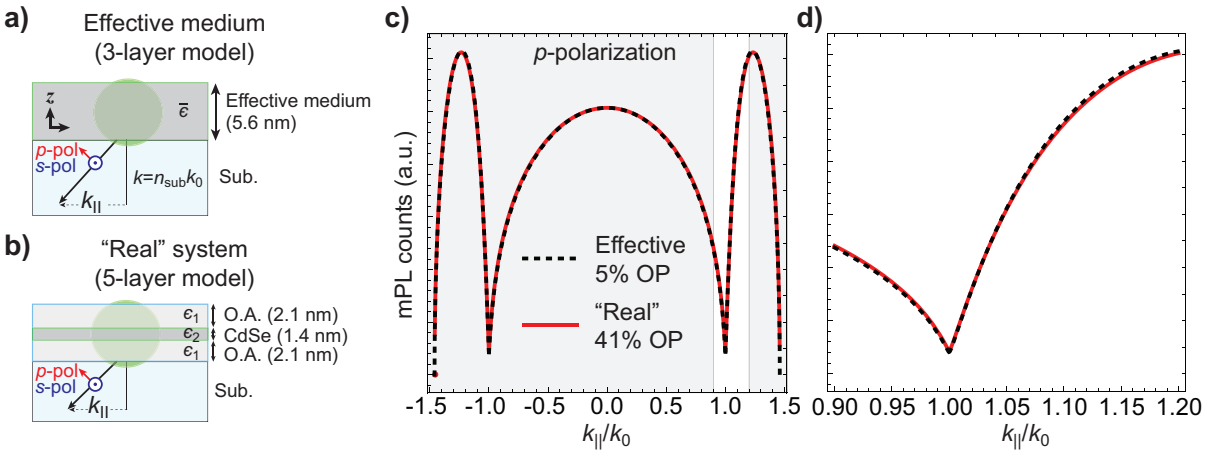

Figure 4.8: ***Three-layer vs. five-layer model for CdSe nanoplatelets*** **(a)** Schematic of the EMM (*i.e.*, three-layer model) and experimental geometry used in ref. [109]. The system comprised of oleic acid and CdSe nanoplatelets are together treated as a homogeneous material with effective uniaxial permittivity $\bar{\epsilon}$. **(b)** Schematic representing a more realistic model (*i.e.*, five-layer model) of the system studied in ref. [109]. **(c)** Momentum-resolved p-polarized radiation patterns from from the CdSe nanoplatelet system. Black dashed line: radiation patterns calculated using the three-layer model with effective-medium permittivities and an OP contribution of 5% (corresponding to observations, *i.e.*, the "data", in ref. [109]). Red solid line: radiation patterns calculated using the rigorous five-layer model and an OP contribution of 41%. **(d)** Magnified view of the p-polarized counts around $k_{||}=k_0$ which arise solely from OP EDs in the thin-film limit. "Real" (*e.g.*, red) and "effective" (*e.g.*, black dashed) models produce identical radiation patterns, but the inferred OP dipole strength differs by nearly an order of magnitude.

4.4.2 Discussion of results presented in Scott *et al.*

We consider the case in ref. [109] in which CdSe platelets (thickness 1.4 nm, ϵ_2=7.9+i 2.6) are surrounded by oleic acid ligands (length 2.1 nm, ϵ_1=2.129). We calculate the resulting radiation patterns using both the three-layer model, and a more rigorous five-layer model which takes completely into account the dielectric inhomogeneity. These two distinct systems are illustrated in Fig. 4.8. All optical constants are taken from Supplementary Information Tables I-II in ref. [109]. The effective medium is characterized by $\bar{\epsilon}_{||}=2.652+i0.192$ and $\bar{\epsilon}_{\perp}=2.332+i0.026$.

Chapter 5

Discovering bright magnetic dipole radiation from a two-dimensional crystal

5.1 Introduction

For atomic systems in free space, magnetic-dipole (MD) transition rates are approximated to be 10^{-5} times lower than those for electric dipoles (EDs) [126, 127]. This intuition has been carried over to crystalline systems and, consequently, light-matter interactions in semiconductors are uniformly treated within the ED approximation, that is, by considering only the first term of a multipolar expansion [111]. In conventional bulk semiconductors (e.g., Si and GaAs), band-edge MD transitions, and similarly electric quadrupole (EQ) transitions, are rigorously forbidden by parity selection rules; ED transitions occur between odd-parity ('p-like') states at the valence band maximum (VBM) and even-parity ('s-like') states at the conduction-band minimum (CBM) [111]. Optical metamaterials [128] and quantum dots [129] have challenged this paradigm, exploiting

multipolar resonances to enhance spontaneous emission rates [130]. However, the resulting light-matter interactions are enforced by the *mesoscale* structure of the material or strong electric field gradients in the vicinity of a plasmonic structure rather than the quantum mechanical properties of the the bulk material.

Whenever the symmetries of the states at play deviate from those described above, however, MD and EQ transitions become formally allowed. Furthermore, a brief examination of transition rates based on Fermi's Golden Rule suggests that MD transitions rates may be significantly enhanced in semiconductor systems. Consider excitations with a mass m in a medium with (isotropic) refractive-index n. Fermi's Golden Rule gives for the spontaneous emission from state i to state f through ED (A_{ED}) and MD (A_{MD}) channels [116]:

$$A_{\mathrm{ED},i\to f} = \frac{\omega^3 \epsilon_0^{1/2} \mu_0^{3/2}}{3\hbar\pi} n |q \langle f| \mathbf{r} |i\rangle|^2 \tag{5.1}$$

$$A_{\mathrm{MD},i\to f} = \frac{\omega^3 \epsilon_0^{1/2} \mu_0^{3/2}}{3\hbar\pi} n^3 \left| \frac{q}{2mc} \langle f| \mathbf{L} + 2\mathbf{S} |i\rangle \right|^2 \tag{5.2}$$

where $\omega{=}2\pi c/\lambda$, c is the speed of light, ϵ_0 (μ_0) is the vacuum permittivity (permeability), $\hbar$ is Planck's constant, q is the charge of the state in question, and $\mathbf{L}$ and $\mathbf{S}$ are the orbital and spin angular momentum operators. Detailed calculations for lanthanide atoms in free space [127] give MD emission rates on the order of 10 s^{-1}. In semiconductors, however, the elementary excitations are states with effective mass $m^*{\sim}0.1m_0$ (rather than the bare electron mass, m_0) in a medium with $n{\approx}2.5$ (for a typical semiconductor). That is, MD transitions from excited states in a crystalline system, assuming not forbidden by symmetry, are expected to be approximately three orders of magnitude faster than those of atoms in free space, significantly reducing the disparity between ED and MD rates.

To demonstrate this possibility, we use energy-momentum spectroscopies to study the polarization-dependent radiation patterns from two-dimensional (2D) hybrid organic-

inorganic perovskites (HOIPs). HOIPs are a rapidly burgeoning class of semiconductors, offering benefits of solution processability, outstanding optoelectronic properties, and the ability to form both three-dimensional (3D) and quantum confined (i.e., 2D) structures [131, 80]. Of particular interest for photonic applications, 2D HOIPs incorporating large alkylammonium molecules (e.g., butylammonium lead iodide, BA_2PbI_4; Fig. 5.1a) offer additional structural and quantum degrees of freedom, providing continuously tunable band-gap energies and desirable narrow excitonic luminescence [83, 132, 133]. Indeed, researchers have demonstrated stable light-emitting diodes (LEDs) with high quantum efficiencies [133, 91, 134], as well as low-threshold optical gain [93]. However, numerous studies reveal anomalous absorption and emission sideband features in both 2D [135, 136, 137, 138, 91] and 3D HOIPs [139] that may be detrimental to color purity.

Insofar as 2D HOIPs are comprised of alternating semiconducting (metal halide) and insulating (organic) layers, they are recognized as "natural" quantum-well semiconductor structures [20]. Accordingly, light-matter interactions in HOIPs are treated by analogy to widely studied conventional semiconductors, such as GaAs [20, 140, 141, 142]. Namely, optical transitions are assumed to be completely described by the ED approximation [111]. Operating within this conventional framework, researchers have attempted to identify the origin of anomalous low-energy sideband features in 2D and 3D HOIPs, arriving at interpretations ranging from bound- or bi-exciton emission [20, 143] to strong phonon-carrier interactions [136, 144]. Recent evidence of more "exotic" and fundamentally interesting physics, such as deep exciton self-trapping [137] and complex exciton-polaron structures [145], strong Rashba and Dresselhaus couplings [146], and an unconventional exciton fine structure [142] reflect the interplay of an unconventional electronic structure, strong spin-orbit coupling [141], structural complexity [147], and the possibility of significant dynamic symmetry-breaking mechanisms [148, 149, 139].

Energy-momentum spectroscopies have surfaced as powerful techniques for identifying

anisotropic and multipolar optical phenomena in thin-film systems [116, 99, 16, 100, **?**, 21, 17]. For example, by analyzing momentum- and polarization-dependent luminescence profiles, researchers have quantified distinct MD and ED optical transitions in lanthanide [116] and transition-metal ions [150], and have identified distinct interlayer excitons in organic semiconductor thin films [99]. Here, energy-momentum spectroscopy reveals that the low-energy sideband in 2D HOIPs exhibits a peculiar polarization and angle dependence characteristic of MD radiation. While the features described herein seem to be generic to the material system, including 3D HOIPs, we exploit the highly oriented and 2D nature of BA_2PbI_4 (Fig. 5.1a) to relate the unusual radiation patterns to the underlying quantum mechanical origins.

5.2 Results

Figure 5.1b shows measured grazing incidence wide-angle X-ray scattering (GIWAXS) patterns from a spin-cast thin film of BA_2PbI_4. This data is consistent with a vertically layered structure in which PbI_4 monolayers are separated by BA_2 spacer layers in the out-of-plane (z) direction [118]. The wavelength-dependent uniaxial complex refractive index of these samples was determined by a combination of momentum-resolved reflectometry [16, 17] and variable-angle spectroscopic ellipsometry. Films exhibit a predominant in-plane (IP) optical response with weak out-of-plane (OP) dispersion, similar to high-quality single crystals [20] and consistent with the vertically layered orientation as determined from GIWAXS. By the nature of the spin-casting method, the resulting films are polycrystalline and thus rotationally isotropic over microscopic length scales relevant for the measurements performed here ($\sim$100 μm) [102]. The highly oriented and rotationally invariant thin-film structure facilitates detailed analysis of momentum- and polarization-dependent optical phenomena using the experimental geometry illus-

trated in Fig. 5.1c. However, as we will describe later, the same features are observed from high-quality single crystals and our conclusions are thus not restricted to spin-cast films. In energy-momentum spectroscopy, both the in-plane electromagnetic momentum ($\mathbf{k}_{||}$=$\langle k_x,k_y \rangle$) and wavelength (λ) distribution of polarized reflection or luminescence are simultaneously measured by imaging the Fourier plane (i.e., back focal plane; BFP) of a collection objective onto the entrance slit of an imaging spectrometer. Polarized spectra are acquired by placing a linear polarizer in the collection path oriented either perpendicular (s) or parallel (p) to the entrance slit (y-axis). Figures 5.1d-f show s- (left) and p-polarized (right) energy- and momentum-resolved PL measured from a 61 nm spin-cast film of BA_2PbI_4 at room temperature.

As seen in Figure 5.1d, s-polarized PL spectra collected above the total-internal-reflection condition $|k_{||}|$=$|k_y|$>k_0 (red dashed) are dramatically different than conventional spectra as collected by a 0.5 NA objective ($|k_{||}| \leq 0.5k_0$; blue). Both s- (left) and p-polarized (right) spectra exhibit the well-established excitonic emission feature at 520 nm. However, a distinct emission feature at 540 nm ($\sim$90 meV energy difference), apparent as a subtle shoulder at low momenta (blue), becomes the dominant emission feature at high momenta (red dashed). In contrast, this emission feature is virtually absent at *all* momenta in p-polarized spectra. This difference in momentum distributions is even more striking when we examine the full energy-momentum spectra (Figure 5.1e; polarization orientation indicated by white arrows). The low-energy emission feature is readily observed as two bright lobes in the s-polarized spectra at $|k_{||}|$>k_0. Importantly, the s-polarized emission features at 520 nm and 540 nm have markedly distinct curvature in k-space (Fig. 5.1f; left). The emission feature at 520 nm (blue) is maximal near normal ($k_{||}$=0) and exhibits a slow roll-off into higher momenta; the opposite is true for emission at 540 nm (orange). This illustrates the critical role of the experimental geometry on the inferred significance of this emission; because this light is emitted at highly

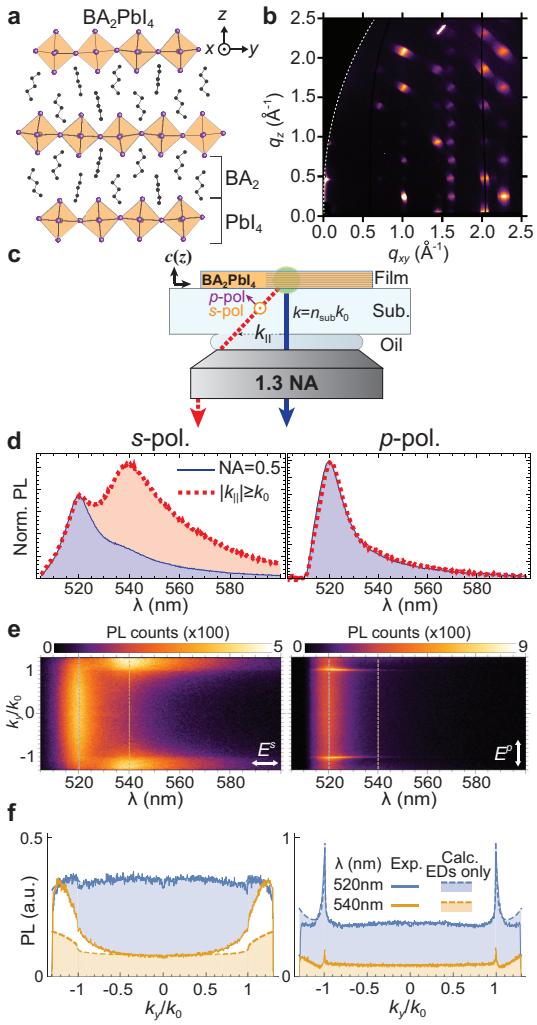

Figure 5.1: **Structure and energy-momentum photoluminescence spectra of BA_2PbI_4.** (**a**) Schematic crystal structure of BA_2PbI_4. Thin films exhibit a vertically layered morphology with repeated PbI_4 monolayers separated in the z-direction by BA_2 spacer layers. (**b**) Experimental GIWAXS patterns of a spin-cast BA_2PbI_4 thin film. (**c**) Experimental geometry: Momentum- ($k_{||}$) and polarization-dependent PL spectra are collected from within the substrate by an oil-immersion 1.3 NA objective. (**d**) s-Polarized (left) and p-polarized (right) photoluminescence spectra of a BA_2PbI_4 thin film (61nm) as collected at two very different regions in momentum space: $|k_{||}|<0.5k_0$ (solid blue) and $|k_{||}|>k_0$ (dashed red). PL traces are normalized to be equivalent at 520 nm. (**e**) s-Polarized (left) and p-polarized (right) energy-momentum spectra from which the PL spectra of Fig. 5.1d were taken. The multipolar emission is readily observable in s-polarized spectra as two bright lobes at λ=540 nm in regions with $|k_{||}|>k_0$. (**f**) Momentum-space line cuts at 520 nm (blue) and 540 nm (orange) for s-polarization (left) and p-polarization (right). Theoretical traces (dashed lines) assuming only oriented electric dipoles agree poorly with 540 nm s-polarized line cuts, showing that the bright high-$k_{||}$ emission cannot originate from an electric dipole transition.

oblique angles with respect to the crystal axis, it would be ordinarily be trapped (i.e., wave-guided) within the high-index substrate, or within the material itself, and thus only weakly collected with conventional PL geometries (e.g., blue lines in Fig. 5.1d). This is a general concern for 2D materials, since the polarization and directionality of the interactions is governed by highly anisotropic electronic wave functions [151]. This may also have significant implications for HOIP-based LEDs; the spectrum and dynamics may be strategically enhanced or refined using photonic architectures [152].

Calculated *s*-polarized PL counts (D), assuming only the existence of ED emission, are shown in Fig. 5.1f (dashed lines) at both 520 nm (blue) and 540 nm (orange). Experimental PL at the 520 nm (primary exciton) emission is accurately described by the ED theory, consistent with an ED-allowed excitonic transition involving Γ_6^- CBM and Γ_6^+ VBM states [140, 141]. The 540 nm emission feature, however, is poorly modeled by the same theory. In contrast, *p*-polarized PL at both 520 nm and 540 nm are well-described by ED-only theory. While low-energy emission shoulders have been observed in conventional PL spectra of both inorganic and hybrid organic-inorganic perovskites [20, 135, 137, 153, 91, 138, 139], none of these prior works examined the polarization and momentum dependence reported here. Note that this theory completely accounts for reabsorption effects by including the complex (uniaxial) refractive index of the material, thus excluding reabsorption as a possible explanation of the secondary peak. The strong high-$k_{||}$ emission excess observed predominantly in *s*-polarization cannot be explained by any combination of oriented ED transitions in a rotationally invariant system; a distinct ED transition centered around 540 nm would contribute with equivalent weight to both *s*- and *p*-polarized spectra, inconsistent with our data. The results presented here thus unambiguously demonstrate that this emission is multipolar in nature.

We observe similar multipolar features at high momenta in a number of related HOIPs, including exfoliated single crystals of the "bilayer" system $BA_2(CH_3NH_3)Pb_2I_7$

(Fig. 5.6), thin films of BA_2PbBr_4, and films prepared with longer alkylammonium cations (octylammonium and dodecylammonium). We find that this feature is robust to sample preparation methods, and is particularly apparent in high-quality single crystals prepared with various alkylammonium cations (including phenethylammonium), and flakes mechanically exfoliated from such crystals. We thus conclude that this feature is general to the material system, and is robust against sample preparation methods and substitutions of both the halide and spacer molecules.

While this feature is regularly observed around 540 nm in exfoliated single crystals, we note that, for similarly prepared BA_2PbI_4 thin films, this emission feature is observed with significantly varying strength at a range of energies between ∼30-90 meV below the primary emission peak. Analyses of thin-film PL spectra under varying illumination and environmental conditions suggest that this variation is due, in part, to the incorporation of oxygen or water under various processing conditions. Note, however, that prolonged illumination in ambient conditions significantly *reduces* the resolution of two distinct peaks, which possibly explains why this feature is so apparent in single crystals. Importantly, this indicates that this sideband does not originate from atmospheric effects (e.g., water or oxygen), but rather seems to be *hindered* by them.

The highly s-polarized nature of the excess (i.e., non-ED) PL provides strong clues for the origins of the multipolar radiation. The candidate oriented multipoles that emit highly oblique s-polarized light are OP MDs and IP EQs. Calculated 2D y-polarized radiation patterns from these multipoles are presented in Fig. 5.2 with s- and p-polarized $k_{||}$-space linecuts shown below and to the right of each 2D image, respectively. OP MDs ("MD_z"; Fig. 5.2a) are associated with a circulating IP electric field and thus produce only s-polarized radiation. However, this s-polarized MD_z contribution is functionally identical to s-polarized emission from IP EQs (Fig. 5.2b; D). Although either MD or EQ terms can be used to fit the s-polarized emission anomaly, identifying the correct multi-

pole term is important for determining the underlying quantum-mechanical origins. To this end, the OP MD and IP EQ can be distinguished by the fact that the OP MD emits no p-polarized PL; in contrast, IP EQs contribute significantly to both s- and p-polarized spectra. Critically, our data shows virtually zero PL excess in p-polarized spectra (Fig. 5.1d), indicating that the multipolar PL is associated with a highly oriented OP MD transition. Note that, while the ED radiation patterns possess features similar to those of the EQ, the preceding discussion is focused solely upon the patterns associated with the *excess* counts (i.e., those not already accounted for by the ED theory). We suspect the very subtle shoulder observed in high-$k_{||}$ p-polarized spectra is due to depolarization scattering from surface texture or slightly tilted crystallite domains in spin-cast thin films. Equivalent measurements on mechanically exfoliated single crystals (Fig. 5.6), in which these imperfections are minimized, show no such p-polarized shoulder and confirm the MD assignment.

The energy-momentum spectra, in combination with the known material optical constants, afford the opportunity to quantify the relative intrinsic multipolar transition rates. At each wavelength, we decompose the momentum distribution of polarized PL counts, $N^{s,p}(\lambda, \mathbf{k}_{||})$, into a linear combination of oriented EDs and OP MDs according to Eqn. 5.3:

$$N^{s,p}(\lambda, \mathbf{k}_{||}) = C_{\text{exp}} \times \big[A_{\text{ED}_{\text{IP}}}(\lambda)\tilde{\rho}^{s,p}_{\text{ED}_{\text{IP}}}(\lambda, \mathbf{k}_{||}) + A_{\text{ED}_{\text{OP}}}(\lambda)\tilde{\rho}^{s,p}_{\text{ED}_{\text{OP}}}(\lambda, \mathbf{k}_{||}) + A_{\text{MD}_{\text{OP}}}(\lambda)\tilde{\rho}^{s,p}_{\text{MD}_{\text{OP}}}(\lambda, \mathbf{k}_{||})\big] \tag{5.3}$$

Here, the $\tilde{\rho}^{s,p}$ are the normalized local density of optical states (LDOS) into which the oriented dipoles may emit, $A(\lambda)$ are the wavelength-dependent intrinsic emission rates, and C_{exp} is a constant factor accounting for setup-specific experimental parameters. Analytical forms for the LDOS are presented in Appendix D. Including the MD contribution,

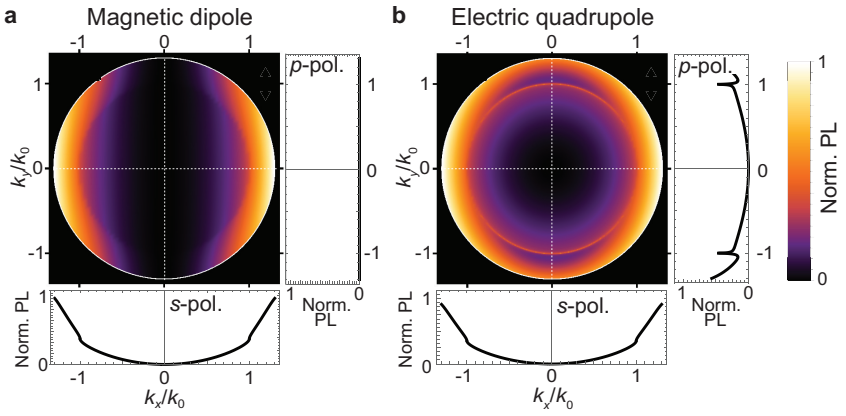

Figure 5.2: **Calculated momentum-resolved multipolar luminescence patterns at λ=540 nm.** (**a**-**b**) Calculated y-polarized momentum-resolved luminescence patterns from (**a**) an OP MD and (**b**) IP EQs. s-Polarized and p-polarized traces are shown below and to the right of each 2D image, respectively. Note that the radiation patterns from OP MDs and IP EQs differ along the p-polarized traces; the s-polarized traces are identical. All calculations were performed for a 61 nm film using known optical constants.

we now see that the experimental radiation patterns for both polarizations are very well represented by the theory across all wavelengths (Fig. 5.3a). The resulting decomposed spectra are presented in Fig. 5.3b. The ED and MD peaks resolved in Fig. 5.3b are observed as genuinely distinct transitions. Though the MD (dashed red) contribution is notably more broad than the ED (black) contribution, both exhibit similar asymmetric lineshapes characteristic of luminescence from quantum wells, suggesting that the MD transition also originates from an exciton-like excited state.

Although multipolar emission is usually orders of magnitude weaker than ED emission, the multipolar contribution in BA_2PbI_4 exhibits an integrated magnitude $[\int A_{\mathrm{MD}}(\lambda)d\lambda]$ comparable to that of the ED, i.e.,

$$\frac{\int A_{\mathrm{MD}}(\lambda)d\lambda}{\int A_{\mathrm{ED}}(\lambda)d\lambda + \int A_{\mathrm{MD}}(\lambda)d\lambda} \approx 0.16. \tag{5.4}$$

As described below, such a strong multipolar PL contribution is highly unusual and

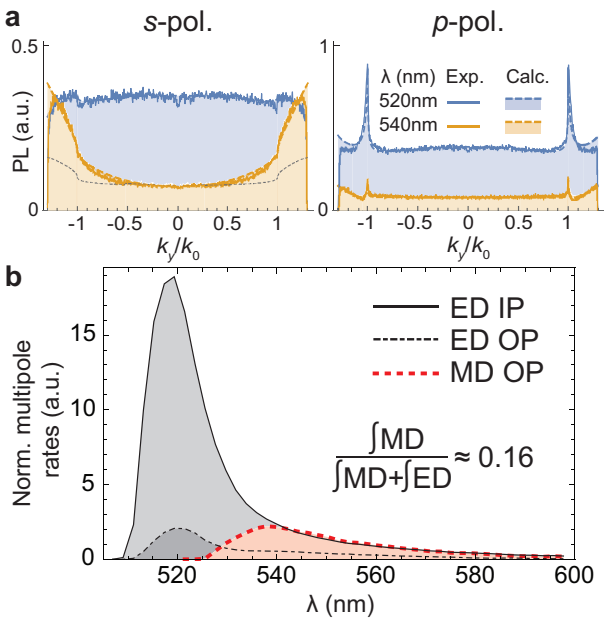

Figure 5.3: **Multipolar decomposition of energy-momentum spectra.** (**a**) Comparison of (dashed filled) theoretical and (solid) experimental momentum-space radiation profiles at λ=520 nm (blue) and λ=540 nm (orange) including both oriented ED and MD transitions. *s*-(*p*-)Polarized spectra are shown on the left (right). All traces show excellent agreement with theory once multipolar components are included in the theory. Calculation excluding MDs is shown as a thin black dotted line. (**b**) Normalized intrinsic multipole radiation rates, $C_{\mathrm{exp}}A(\lambda)$, determined from multipolar decompositions of energy-momentum spectra: IP EDs (black solid); OP EDs (black dot-dashed); OP MDs (red dashed).

particularly unexpected when we consider the overall fast dynamics of the system. In lanthanide ions, for instance, multipolar PL is observed due to long-lived ($\sim$100 μs) excited states associated with ED-forbidden recombination channels [154, 127]. Here, however, we observe sub-ns PL lifetimes for the main excitonic feature at 520 nm (Fig. 5.4a, blue circles).These PL decay traces were measured at reduced temperature (250 K) to try to better isolate any differences in the excited state dynamics [139]. Still, PL traces of the isolated 540 nm feature (Fig. 4a, red squares) show no discernible differences; both traces are well represented by a bi-exponential decay with a primary component lifetime of $\tau\approx$296 ps, consistent with values obtained for the primary exciton in previous reports [144, 155]. Just below 250K, BA_2PbI_4 shows a structural phase transition [82] accompanied by an abrupt change in the PL spectrum. Nonetheless, distinct ED and MD PL features can be identified at low temperatures by comparing spectra from highly oriented and randomly oriented film morphologies (e.g., Fig. 5.7), further supporting the generality of MD emission over a large temperature range. These two emission features also show nearly identical behavior under intensity-dependent PL. Throughout a very broad range of excitation intensities (I_{exc}=1-750 mW/cm^2) the spectral shape is observed to be nearly invariant (Fig. 4b; darker colored lines). Only at extremely high excitation intensities ($I_{\mathrm{exc}}>10^3$ mW/cm^2; lighter colored lines) does the spectrum begin to vary, with the *low-energy* feature growing in relative strength. Power-law fits of the decomposed spectra ($I_{\mathrm{PL}}\propto I_{\mathrm{exc}}^{\alpha}$) (Fig. 5.4c) reveal that both the ED contribution (black; α_{ED}=1.17$\pm$0.05) and the multipolar contribution (red; α_{MD}=1.15$\pm$0.04) grow in parallel. Note that the data presented in Fig. 5.4 was measured from poly-crystalline samples with random crystallite orientations in order to enhance the visibility of the 540 nm emission feature with conventional spectroscopy techniques, but similar conclusions are made from analogous measurements on spin-cast thin films. This intensity dependence excludes bi-excitons (α=2) or excitons bound to *extrinsic* defects (α<1) as a likely origin. In light

of recent reports highlighting the prevalence of low-energy "white-light emitting" states in 2D HOIPs [137], we note that this pump dependence is consistent with an (intrinsic) self-trapping mechanism. The red-shift between MD and ED features is expected from such a mechanism, but the 90 meV energy difference observed here is significantly smaller than that of previously observed white-light emitting states.

The *absolute* radiative lifetimes can be estimated from the measured PL lifetime, quantum yield (PLQY), and normalized multipolar emission rates. Assuming that the measured PLQY of 0.4% is representative of both emission features, our data implies radiative rates of 1.4×10^7 s^{-1} and 1.9×10^6 s^{-1} for the ED and MD respectively, assuming the emission arises from identical exciton densities. (Note that this PLQY is comparable to previously reported values for this material [135].) However, considering the 90 meV energy splitting, the observed low-energy (MD) transition rate could be enhanced relative to the high-energy (ED) transition due to the thermal occupation of excited states. If we assume two distinct emissive channels in thermal equilibrium, the intrinsic MD radiative rate is reduced by a factor of exp(90 meV/26 meV)≈30, yielding an intrinsic radiative rate of 6.0×10^4 s^{-1}. Even with this more conservative estimate, the inferred multipolar radiative rate is three orders of magnitude larger than any MD emission rate reported from atomic systems [127], and is curiously close to that predicted from the discussion surrounding Eqns. 5.1-5.2. There is, to our knowledge, no crystalline system to which this may yet be compared. The multipolar emission observed in BA_2PbI_4 is extraordinarily bright and challenges conventional understanding of multipolar light-matter interactions.

We now consider the electronic band structure as it relates to the origins of the multipolar PL signature. Density functional theory (DFT) calculations of the BA_2PbI_4 electronic structure are summarized in Fig. 5.5. At each wave vector, $\mathbf{k}$, along the Γ-X and Γ-U directions of the reciprocal lattice, we project the ground-state eigenfunctions onto a basis consisting of I (Fig. 5.5b) and Pb (Fig. 5.5c) orbitals with symmetries cor-

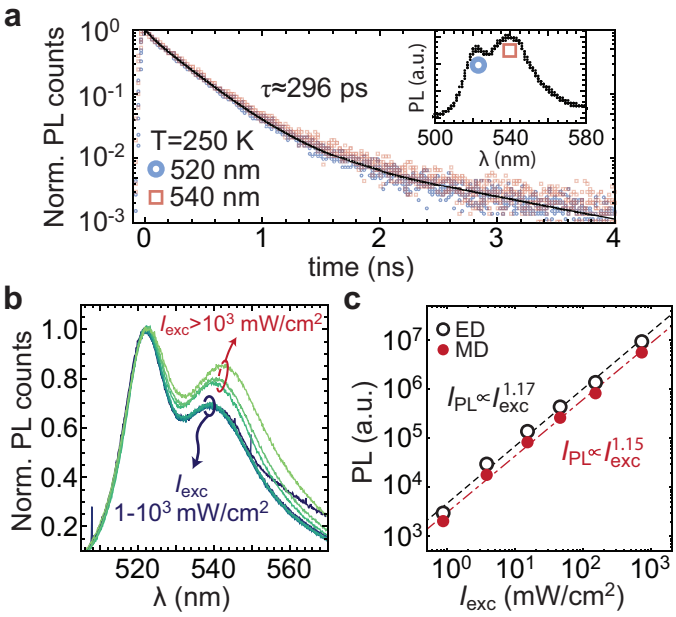

Figure 5.4: ***Dynamics and pump-dependence of emission features:*** (**a**) Time-resolved photoluminescence traces of the 520 nm (blue) and 540 nm (red) emission features from drop-cast films at 250 K. Data at both wavelengths is well represented by a bi-exponential decay (black) with a τ=296 ps primary component. Reduced temperature increases the relative strength of the 540 nm emission feature. 250 K was chosen to reduce thermally assisted energy transfer between states. (**b**) Pump intensity-dependence of PL spectra from a drop-cast film at T≈300 K. Data has been normalized to the PL at 520 nm. (**c**) Log-log plot of integrated PL strength (I_{PL}=$\int A(\lambda)d\lambda$) from ED (black) and MD (brown) contributions as a function of excitation intensity, I_{exc}. Lines are power law fits: $I_{\mathrm{PL}} \propto I_{\mathrm{exc}}^{\alpha}$ with nearly identical exponents for the ED (α=1.17±0.05; black) and MD (α=1.15±0.04; red) emission.

responding to s, p_x, p_y, and p_z orbitals. The weight of the projection is represented by the size of the circle at each $\mathbf{k}$. The VBM (set to 0 eV in the band diagrams) comprises roughly equal contributions from I $(5)p$ orbitals and Pb $(6)s$ orbitals, in agreement with previous reports [141]. (I and Pb p_y contributions are not shown since they are nearly identical to p_x, due to the system's approximate C_4 symmetry.) Note, however, that the I p_z contribution is significantly suppressed relative to the IP contributions. The CBM comprises nearly equal contributions of Pb $(6)p_x$ and $(6)p_y$ orbitals with an absent p_z contribution. The symmetries of the CBM and VBM states participating in optical transitions, however, are governed by the bonding character of the constituent atoms. Previous studies have assigned Γ_6^- ('p-like') and Γ_6^+ ('s-like') symmetries to the CBM and VBM wavefunctions, $|\psi_{\mathrm{CBM}}\rangle$ and $|\psi_{\mathrm{VBM}}\rangle$, respectively [140, 141]. In analogy with conventional semiconductors, these states may be qualitatively represented by $|X\rangle$ and $|Y\rangle$ (CBM), and $|S\rangle$ (VBM); a predominantly IP ED transition is described by a symmetry analysis of the ED matrix elements between CBM and VBM states: $\langle S|\, x\, |X\rangle \approx \langle S|\, y\, |Y\rangle$ and $\langle S|\, z\, |\psi_{\mathrm{CBM}}\rangle \approx 0$ [141]. The non-zero ED_z contribution observed here and in previous experiments [20, 21, 17] likely arises from a non-negligible I p_z contribution at the VBM and an I $(5)s$ contribution at the CBM. Electron-hole correlations yield three distinct (1s) exciton levels with *odd* parity, corresponding to the direct product of $\Gamma_6^- \otimes \Gamma_6^+$, and an *even* parity crystal ground state [140]. However, selection rules still reflect the underlying VBM and CBM states and these conclusions are thus unaltered. Such treatments have been used with apparent success to describe the low-temperature exciton spectrum observed in previous reports [20, 140, 142].

In contrast to the ED term, the MD term connects states with *equivalent* parity [154, 156]. Symmetry based analyses of multipolar matrix elements are outlined in Supplementary Information section 5.4.1. Qualitatively, in the electron-electron picture, MD_z connects CBM and VBM states with IP extended orbitals; the necessary Bloch

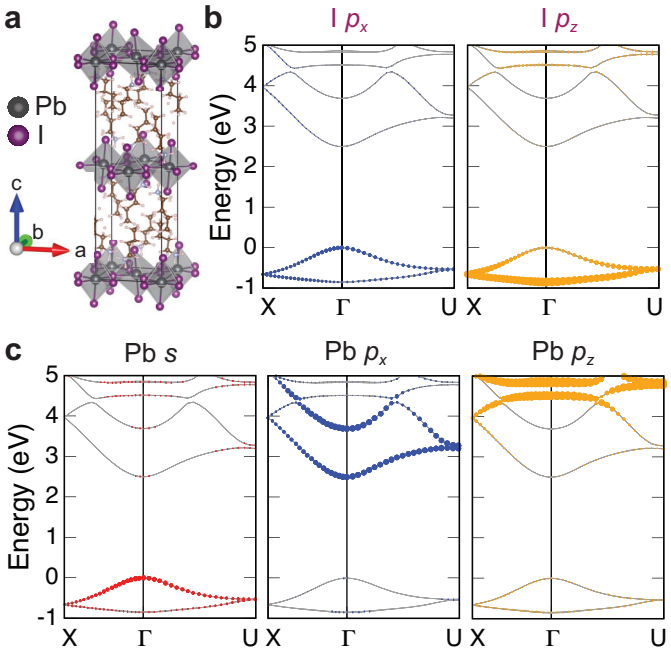

Figure 5.5: ***Calculated band structure and band character of BA_2PbI_4.*** (**a**) The BA_2PbI_4 unit cell used in DFT calculations comprises two distinct layers. Pb atoms are shown in black and I atoms are shown in purple. (**b-c**) Computed band structures along the Γ-X and Γ-U directions of the reciprocal lattice, projected onto Pb and I orbitals with symmetries of s, p_x, p_y, and p_z. The relative weights are represented by the size of the circles at each momentum. (**b**) I p_x (left) and p_z (right) contributions to the band structure. I (5)p orbitals contribute primarily to the valence bands. The valence band maximum (VBM; energy set to 0 eV) predominantly derives from in-plane I (5)p orbitals (p_x and p_y). (**c**) Pb s (left), p_x (center) and p_z (right) contributions to the band structure. The conduction band minimum (CBM) predominantly derives from in-plane Pb (6)p orbitals (p_x and p_y). The VBM also shows significant contributions from Pb (6)s orbitals. In all cases, p_y contributions are identical to p_x contributions and are thus are not shown.

states are absent in the VBM and thus these multipolar transitions are strictly forbidden within the aforementioned treatment for 1s excitons (Eqn. S43). While this selection rule is *reversed* for a *p*-like exciton envelope function (Eqn. S47), the hydrogenic 2p exciton state lies at energies ≈300 meV *higher* than than the 1s exciton state [140] and is thus excluded as a likely candidate. Our experimental results thus suggest the presence of structural distortions that generate a low-energy excited state (e.g., exciton or exciton-polaron) with distinct (i.e., even) parity. Indeed, a surge of recent reports highlight the importance of *dynamic* symmetry-breaking mechanisms, e.g., thermally-induced lattice distortions [146, 148, 149, 139] and a strong polaronic character of excited states [157, 145, 158, 159], both reflecting the relatively "soft" ionic lattice. Though numerous DFT studies have explored the role of typical static asymmetries [147] and thermal fluctuations in HOIPs [149], none have established a significant change in electronic state symmetries or optical selection rules. The MD feature observed here appears as a spectrally distinct excited state, favoring polaronic effects — namely, exciton self-trapping — as a potential origin, especially in light of potential parity-breaking polaron phenomena [160, 158, 159]. For example, a *p*-like electron-hole configuration with *lower* energy — the "off-site" self-trapped exciton in some references — may be induced and stabilized by interactions with antisymmetric lattice distortions [160, 159]. Indeed, the pump dependence (Fig. 5.4c) is consistent with a self-trapping mechanism. This hypothesis is bolstered by a dramatic thermal red-shift of the MD feature (Fig. 5.7), mirroring similar thermal shifts observed for self-trapped exciton-polaron states in lithium niobate due to significant "lattice softening" with increasing temperatures [161].

5.3 Discussion

Exploiting the highly-oriented structure of 2D HOIPs, and taking into account polarization-, wavelength-, and angle-dependent collection effects, we identify an oriented, exceptionally fast magnetic dipole optical transition that appears as a PL sideband at room temperature. The unconventional radiation properties of the sideband luminescence have not yet been acknowledged. Consequently, the magnitude of these transitions has been largely underestimated. Similar directional effects are expected to afflict optical studies of other 2D materials [151]. The presence of a multipolar transition in 2D HOIPs is evidently inherent to the material system. Accounting for extrinsic collection effects, we show that the MD radiative rate is at least three orders of magnitude larger than multipolar emission rates previously identified in atomic systems; there is yet no other crystalline system to which these rates may be compared.

This observation of bright MD luminescence, coupled with first-principles considerations of radiation rates (Eqns. 1-2), suggests that multipolar phenomena may be more prevalent than previously thought and challenges a long-standing assumption that may limit further understanding and development of novel materials, especially for optoelectronic devices such as LEDs and lasers. Though the precise role of spin-orbit coupling and quantum-confinement remains unresolved, the physics demonstrated here may impact the development of quantum information applications based on "dark" (ED-forbidden) excitons in 2D materials [162]. Metamaterials communities regularly exploit classical electric dipolar and multipolar resonances [128, 163] to engineer directional radiation patterns, but assume that multipolar effects are negligible at the quantum level. The distinct electric field symmetries associated with the spectrally separated ED and MD radiation in 2D HOIPs thus point toward the possibility of engineering unique light-matter interactions in nanoscale resonators constructed from 2D HOIPs, as has recently been explored

in WSe_2 [164].

5.4 Supporting Information

5.4.1 Analysis of transition matrix elements

Here we discuss the multipolar optical transition selection rules by describing the initial (CBM) and final (VBM) states in terms of Bloch functions at $\mathbf{k}$=0, with with p- and s-like symmetries, respectively. We refer to this as the "conventional treatment", in analogy with the formalism developed for III-V semiconductors [111], as used in several recent reports [141, 142]. We show that within this treatment MD and EQ transitions are strictly forbidden.

In the presence of spin-orbit coupling (SOC), neither orbital (L) nor spin (S) angular momentum are good quantum numbers, and one instead takes eigenstates of *total* angular momentum (squared), $\hat{J}^2 = \hat{\mathbf{J}}^2 = (\hat{\mathbf{L}} + \hat{\mathbf{S}})^2$, and its projection, $\hat{J}_z$, along a particular quantization axis: $|J, J_z\rangle$ [111, 141, 142]. The quantization axis, $\hat{z}$, is conveniently taken to be the dimension in which carriers are most strongly confined (e.g., the c-axis in 2D HOIPs or the out-of-plane direction for nanoplatelets of 3D HOIPs). In HOIPs, the CBM is associated with the spin-split band with J=1/2 (and L=1). In previous studies, the VBM is treated with an overall s symmetry, and is thus represented by the Bloch function $|S\rangle$ (L=0, and thus J=1/2) [140, 141, 142]. The orthonormal CBM and VBM

states within this description are:

$$|\psi_{c,+}\rangle = \left|\frac{1}{2},+\frac{1}{2}\right\rangle_c = \frac{1}{\sqrt{2}}(|X\rangle_c + i\,|Y\rangle_c)\,|\downarrow\rangle \tag{5.5}$$

$$|\psi_{c,-}\rangle = \left|\frac{1}{2},-\frac{1}{2}\right\rangle_c = -\frac{1}{\sqrt{2}}(|X\rangle_c - i\,|Y\rangle_c)\,|\uparrow\rangle \tag{5.6}$$

$$|\psi_{v,+}\rangle = \left|\frac{1}{2},+\frac{1}{2}\right\rangle_v = |S\rangle_v\,|\uparrow\rangle \tag{5.7}$$

$$|\psi_{v,-}\rangle = \left|\frac{1}{2},+\frac{1}{2}\right\rangle_v = |S\rangle_v\,|\downarrow\rangle \tag{5.8}$$

in which v (c) denotes valence (conduction) band states, and $|\uparrow\rangle$ ($|\downarrow\rangle$) is the eigenstate of $\hat{\mathbf{S}}$ with eigenvalue +1/2 (-1/2). $|X\rangle$ and $|Y\rangle$ correspond to real p-like orbitals (analogous to atomic L=1 orbitals) with symmetry axes along the Cartesian x and y directions, respectively. We have here assumed that the $|Z\rangle$ contribution at the CBM is negligible, in accordance with the 2D nature of the orbitals [141]. By symmetry considerations, it is immediately apparent that the ED matrix elements, $M_{ED} \propto \langle 1/2, \pm 1/2|\,\hat{x}_i\,|1/2, \pm 1/2\rangle$ (i=1,2,3), are *in general* non-zero since the individual terms $\langle S|_v\,\hat{x}\,|X\rangle_c = \langle S|_v\,\hat{y}\,|Y\rangle_c \neq 0$, thus driving in-plane electric dipole band-to-band transitions in HOIPs. Accounting for electron-hole exchange (i.e., excitons), specific singlet/triplet combinations may become ED-allowed or ED-forbidden, as determined by considering the proper product combinations of states as presented in Eqns. 5.5-5.8; e.g., $|\psi_{c,i}\rangle\,|\psi_{c,j}\rangle$ with i and j independently taking the 'values' '+'(=sign(+1)) and '−'(=sign(−1)) [140, 142] (which we henceforth write as i, j=+, −). (Equivalently, there are four distinct matrix elements to consider for the states in Eqns. 5.5-5.8, some of which are zero.)

5.4.2 Magnetic dipole transitions: orbital and spin wavefunction considerations

The MD vector operator is given by $\hat{\mathbf{m}}=(e/2mc)(\hat{\mathbf{L}}+2\hat{\mathbf{S}})$ where e and m are the charge and mass of the particle in question, respectively [156]. Our experimental results motivate us, in particular, to inspect $\hat{m}_z \propto \hat{L}_z + 2\hat{S}_z$, and thus we analyze matrix elements of the form $\langle\psi_{v,i}|\,\hat{m}_z\,|\psi_{c,j}\rangle \propto \langle\psi_{v,i}|\,(\hat{L}_z+2\hat{S}_z)\,|\psi_{c,j}\rangle$ with $i,j=+,-$. Notice that the orbital components in $|\psi_{v,i}\rangle$ and $|\psi_{c,j}\rangle$, as written in Eqns. 5.5-5.8, are $\hat{L}_z$ eigenstates, all terms in which are associated with a single specific value of L (i.e., L=0 for VBM states and L=1, $L_z=\pm1$ for CBM states). (More generally, all orbital terms exist within a subspace associated with a single specific *parity* of L; e.g., L=0,2,4,... for VBM states. Terms with $L>1$, however, are small contributions and rigorously do not affect the conclusions of our following symmetry arguments.) Therefore, all terms $\langle\psi_{v,i}|\,\hat{m}_z\,|\psi_{c,j}\rangle$ are immediately seen to be zero. Specifically, restraining our attention to L=0 and L=1 leading terms for the VBM and CBM, respectively, Eqns. 5.5-5.6 can be rewritten in terms of spherical harmonics ($|l,m_l\rangle$):

$$|\psi_{c,+}\rangle \approx |L=1,m_l=+1\rangle_c\,|\downarrow\rangle \tag{5.9}$$

$$|\psi_{c,-}\rangle \approx -\,|L=1,m_l=-1\rangle_c\,|\uparrow\rangle \tag{5.10}$$

and $|S\rangle_v \approx |L=0,m_l=0\rangle_v$. (The symbol $\approx$ is used to indicate that we have chosen to ignore contributions with $L>1$.) With these we analyze the terms in the matrix elements of interest:

$$\begin{aligned}\langle\psi_{v,i}|\,(\hat{L}_z+2\hat{S}_z)\,|\psi_{c,j}\rangle &= \langle\psi_{v,i}|\,\hat{L}_z\,|\psi_{c,j}\rangle + 2\,\langle\psi_{v,i}|\,\hat{S}_z\,|\psi_{c,j}\rangle \\ &= j\,\langle\psi_{v,i}\rangle\,\psi_{c,j} + 2(-j\times\frac{1}{2})\,\langle\psi_{v,i}\rangle\,\psi_{c,j} = 0\end{aligned} \tag{5.11}$$

where j=+1,−1 and in the final equality we have utilized the orthogonality of the terms with differing L. However, an odd-parity term in the VBM is necessary to generate a non-zero $\hat{m}_z$ matrix element. In particular, since $\hat{L}_z\,|S\rangle$=0, we conclude that odd-parity terms must be included in the VBM in this picture. The preceding arguments remains true even when accounting for excitonic correlations of the electron and hole states, *specifically for the 1s exciton state*, as this can only introduce a spherically (or, in 2D, circularly) symmetric envelope function to the analysis. That is, the multipolar character of the transition is determined from the underlying electron and hole Bloch states comprising the exciton [140]. Note, however, that this selection rule on the Bloch states is *reversed* for a p-like exciton envelope state. While hydrogenic p-like (e.g., 2p) exciton states typically lie at energies ≈300 meV *higher* than than the 1s exciton state [140], a p-like exciton configuration with lower energy — in some references referred to as "off-site" self-trapped exciton — may be induced by interactions with antisymmetric lattice distortion, e.g., as in refs. [160, 159].

5.4.3 Magnetic dipole transitions: Group theoretical considerations

Approximating the crystal point group as D_{4h} [140] and restraining our attention to the Γ-point ($\vec{k}$=0), the MD_z operator ($\sim R_z$) transforms according to the irreducible representation A_{2g}. The in-plane electric dipole operator ($\sim x, y$) transforms as E_u. Electron (at the CBM) and hole states (at the VBM) transform as E_u and A_{1g}, respectively. The corresponding s-like envelope function transforms also as A_{1g} and an in-plane p-like envelope function transforms as E_u. The crystal ground state also transforms as A_{1g}.

Electric dipole transitions w/ s-like exciton envelope: We consider the direct product

$$\underbrace{A_{1g}}_{\text{final state}} \otimes \underbrace{E_u}_{\text{IP ED}} \otimes \underbrace{(A_{1g} \otimes E_u \otimes A_{1g})}_{\text{initial state}} = E_u \otimes E_u = A_{1g} \oplus A_{2g} \oplus B_{1g} \oplus B_{2g} \supset A_{1g} \quad (5.12)$$

Since the result contains the totally symmetric representation A_{1g} of D_{4h}, the transition is allowed, which agrees with the discussion above.

Electric dipole transitions w/ p-like exciton envelope:

$$A_{1g} \otimes E_u \otimes (E_u \otimes E_u \otimes A_{1g}) = E_u \otimes (E_u \otimes E_u) = E_u \otimes (A_{1g} \oplus A_{2g} \oplus B_{1g} \oplus B_{2g}) \not\supset A_{1g} \quad (5.13)$$

in which the final relation follows simply from the result that the product representation of two irreducible representations, e.g., Γ_m and Γ_n, contains the totally symmetric representation, $\Gamma_1(=A_{1g})$, once if $m{=}n$, otherwise the product does not contain Γ_1 [156]. Therefore, electric dipole transitions from the p-like exciton state are forbidden.

Magnetic dipole transitions w/ s-like exciton envelope:

$$A_{1g} \otimes A_{2g} \otimes (A_{1g} \otimes E_u \otimes A_{1g}) = A_{2g} \otimes E_u \not\supset A_{1g} \quad (5.14)$$

Magnetic dipole transitions w/ p-like exciton envelope:

$$\begin{aligned} A_{1g} \otimes A_{2g} \otimes (E_u \otimes E_u \otimes A_{1g}) &= A_{2g} \otimes (E_u \otimes E_u) \\ &= A_{2g} \otimes (A_{1g} \oplus A_{2g} \oplus B_{1g} \oplus B_{2g}) \supset A_{1g} \end{aligned} \quad (5.15)$$

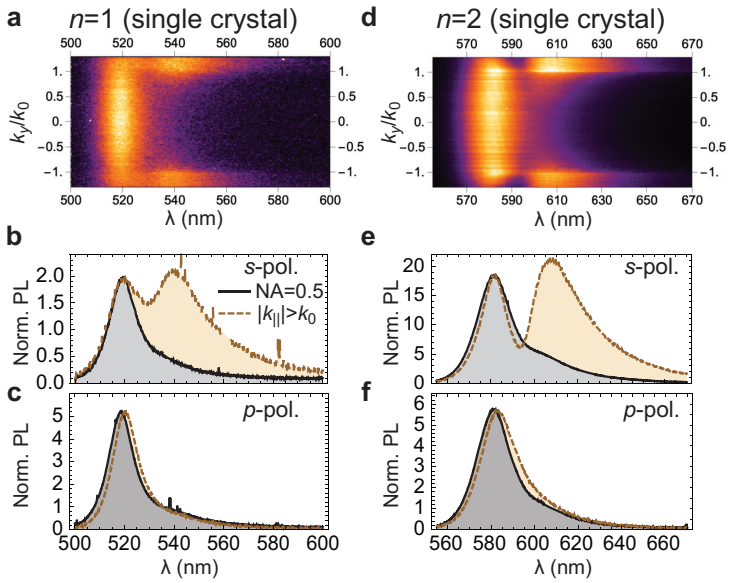

Figure 5.6: ***Multipolar emission in exfoliated single crystals of*** $(C_4)_2(C_1)_{N-1}Pb_NI_{3N+1}$ ***with n=1-2.*** Polarization- and momentum-dependent PL spectra of exfoliated single crystals of $(C_4)_2(C_1)_{N-1}Pb_NI_{3N+1}$ with (**a-c**) n=1 and (**d-f**) n=2. (**a**) s-Polarized energy-momentum PL spectra. (**b**) s-Polarized and (**c**) p-polarized spectra collected at $|k_{||}|<0.5k_0$ (NA=0.5; solid) and $|k_{||}|>k_0$ (dashed). (**d**) Same as (a), but for single crystals with n=2. (**e**) Same as (b), but for single crystals with n=2. (**f**) Same as (c), but for single crystals with n=2. In both cases, a secondary strong emission peak at high momenta ($|k_{||}|>k_0$) arises in the s-polarized spectrum at an energy ≈90 meV below the primary ED-mediated exciton emission peak.

in which we have again used the result stated after Eqn. 5.13. In agreement with the discussion in the previous section, we find that that the magnetic dipole transition from the exciton state with p-like envelope is allowed. We also find that the electric dipole transition from this state is forbidden, which may account for the distinct pure-MD character of the 540 nm emission.

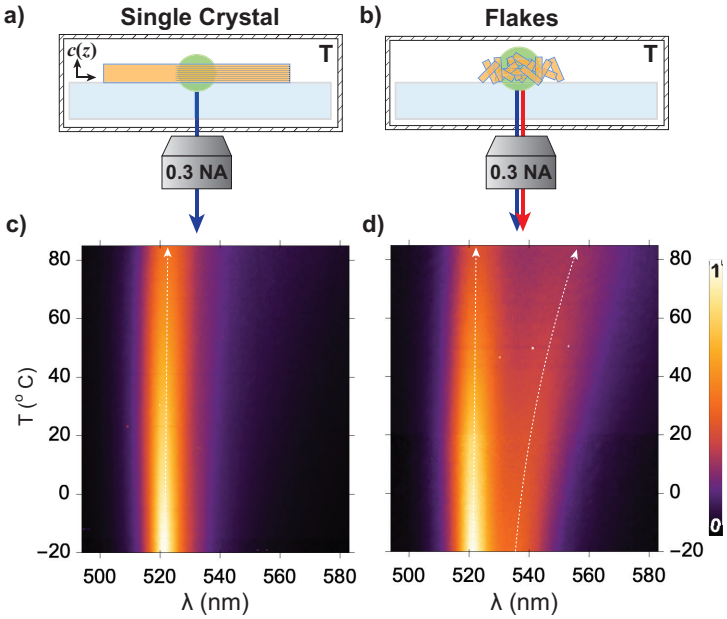

Figure 5.7: ***Temperature-dependent PL of ED and MD emission features in 2D HOIPs.*** (**a-b**) Schematic of experimental geometry for measuring ED and MD PL with varying temperature using a low-NA (NA=0.3) objective. (**a**) The ED emission feature is observed by collecting light near normal exitance (i.e., along the z-axis) from single crystals. (**b**) Both ED and MD emission features can be observed with a low-NA objective by positioning crystals with random orientations on the substrate. (**c-d**) 2D images of PL as a function of temperature. The white dashed arrows highlight the two distinct PL peaks as a function of temperature. Notably, the peak wavelength and width of the MD emission feature, attributed to lattice dynamics, is strongly dependent on temperature. In contrast, the ED emission feature, associated with the static structure, is remarkably stable with temperature. This particular data was measured from crystals of $(C_8H_9NH_3)_2PbI_4$ (phenethylammonium lead iodide) due to its enhanced stability with temperature and lack of structural phase transitions in the temperature range of interest.

Chapter 6

Conclusions and Outlook

We have demonstrated that Fourier imaging principles can be applied to the excitation process, allowing for quantification of linear *absorption* dipole moments in thin-film systems. Analyzing polarized reflection over *in-plane momenta* (and at a single wavelength), rather than over wavelength (and at a single in-plane momentum), obviates modeling uncertainties inherent to state-of-the-art techniques, e.g., VASE. A universal "Fresnel model" is used, which thus introduces only two free parameters (per polarization state) which are the sole parameters of interest for material characterization. In comparison, in a typical VASE analysis, dozens of free parameters must be refined simultaneously. Specifically — and of particular interest for fundamental materials science — these momentum-resolved spectroscopies performed with a high-NA imaging system provide unique sensitivity to distinct *out-of-plane* excitations. In Chap. 3, we demonstrated the ability to resolve subtle variations in the optical absorption anisotropies in organic thin films with two distinct morphologies, but comprised of the same polymer species.

Previous reports have used the basic Fourier imaging technique to study near-field coupling of localized excitations to plasmonic dipole antennas [165] and nano-scale Yagi-Uda arrays [166], luminescence of extended emitters through photonic-crystal modes of

uniform dielectric arrays [167], exciton-polariton condensation [168, 169], emission dipole orientations in 2D transition metal dichalcogenides [99], and magnetic dipole emission from lanthanide [116] and transition metal atoms [150]. The results demonstrated here further extend these capabilities; Fourier imaging principles, in combination with traditional spectroscopy methods, applied to now to both emission and *excitation* processes leads to an incredibly versatile suite of optical spectroscopy techniques that can be performed with a single experimental setup. These techniques may be immediately generalized to study two-photon polarization-dependent optical selection rules [170], Raman scattering tensor elements [171], and momentum-dependent non-linear mixing processes.

In Chap. 4, we used the unique capabilities of momentum-resolved reflectometry to resolve a long-standing conflict about variations of optical anisotropies in 2D HOIPs. Namely, while quantum-mechanical calculations suggest the semiconductor polarizability is invariant to the organic barrier length [103, 104], several experimental reports reveal variations that are seemingly in direct conflict with these calculations [20, 21]. This conflict is resolved by taking into account the significant dielectric inhomogeneity of these systems. Namely, by applying a layered effective-medium model, we showed that the variations arise predominantly through *classical* electromagnetics effects, enforced by polarization-dependent matching conditions between the semiconducting and insulating layers of the material.

Chap. 5 described the discovery of first-ever fast multipolar emission from a bulk crystal, i.e., 2D HOIPs. Specifically, by exploiting the highly-oriented thin-film structure of butylammonium lead iodide, we identified the origins of the emission as an out-of-plane oriented magnetic dipole transition. Quantum-mechanical considerations suggest that the highly oriented nature of this magnetic dipole transition arises from the two-dimensional nature of the electronic states. First-principles considerations suggest that the magnetic dipole transition rates in semiconductors may be $\sim 10^3$ times greater than

those for atoms in free-space. This new realization may have profound consequences in the interpretation of optical spectroscopy data, which is currently assumed to be completely governed by electric dipole processes. Although this process was observed in *emission*, the reciprocity principle suggests that *absorption* may also be mediated via magnetic dipole interactions at a similar rate. This could potentially be resolved, for example, by exciting the sample with azimuthally polarized vector vortex beams [172] or by searching for systematic deviations in the high-momentum s-polarized reflectance. If observed in these systems, 2D perovskites may thus provide many interesting avenues for future studies of strong magnetic light-matter interactions, e.g., by placing thin exfoliated flakes in high-quality optical cavities to generate polaritons driven by the magnetic component of light.

Appendix A

Detailed instructions for the mR technique

This Appendix is primarily intended as a practical guide for researchers to measure and analyze momentum-resolved reflectometry data.

A.1 Measurement procedure

A.1.1 Preliminary considerations

The purpose of the mR technique is to quantify *uniaxial* optical constants of a thin film sample without the need for dispersion models. We therefore should begin with a sample we suspect is uniaxial. The technique may be used for a sample that is suspected to be optically isotropic, but it is likely not necessary and ellipsometry might be just fine. Regardless, for practical purposes, the sample geometry should approximate that of an ideal two interface system with planar parallel interfaces, so that we can utilize Fresnel's reflection equations. To this end, the sample substrate should be a high-quality, well-known material. For practical purposes, the thin film should be *very thin*, such that

its thickness, t, is much shorter than the wavelength, λ, of light in the material with refractive index, n: $t << \lambda/n$. Further, to be approximately represented by an ideal two-interface system, the surface roughness should be minimal. There is no problem fundamentally with the measurement or the analysis in the case of a very rough film, or even one with pin-holes. However, in this case, the model becomes less applicable and the results thus don't contain the physical meaning we are hoping to extract. In a common "good" scenario for a spin-cast film, we might have total surface roughness layer of ≈5-10nm (i.e., the z distance between the maxima and minima of the film thickness). This is fine, unavoidable, and I have developed my analysis code to account for this type of roughness. This will all be discussed in more detail later.

A.1.2 Set up the excitation sources

For efficiency, we want to "flood" the BFP with light of *all* wavelengths. This allows us to measure all $\mathbf{k}_{||}$ and wavelengths, λ, simultaneously. (This is in contrast to the point-by-point procedure described in [16].) The light source can in principle be anything. It should be broadband. For example, to cover approx. 500-750nm almost uniformly, I typically use the "Cool-white" ThorLabs LED (see Fig. A.1) for the blue end of the spectrum and the table-top white-light source for the red end of the spectrum (will be demonstrated later). Ideally, we'll have a single very broadband source with uniform intensity over all wavelengths in the visible, into the UV.

The basic setup is illustrated in Fig. A.1. A lens with a focal length f ('Lens 1', typically f=25mm in our case, but may generally differ if needed) images the BFP of the objective to a distance f from the lens.[1] (All BFPs and focal planes (FPs) are specified as a dashed line in the schematic aerial view.) This BFP is labeled 'BFP 1' in the schematic.

[1] Alternatively, one can conceive of this as follows: Lens 1 performs a Fourier transform of the sample image plane (at a distance f 'behind' the lens, ideally at the microscope exit port; see dashed lines in Fig. A.1) to another plane at a distance f 'in front' of the lens.

This is the plane where we would put a point source (e.g., optical fiber tip) if we wanted to do plane-wave illumination of the sample with a particular $\mathbf{k}_{||}$ (e.g., as in ref. [16]). In the current case, we want to illuminate over *all* momenta simultaneously and uniformly. For this purpose, we put a diffuser film at 'BFP 1', i.e., a distance f from a 'Lens 1'.[2] Ultimately, we want *polarized* reflectance data. A linear polarizer (LP) is thus placed an arbitrary distance between the microscope and 'Lens 1'.

Because of the light is spread out over all momenta (due to the diffuser film), the light intensity at the CCD/spectrometer will be relatively weak. For example, I typically run the Thorlabs LEDs at 0.15A to get a visible signal of 500 counts per pixel with an integration time of 2s in LightField (to be discussed further later). See Fig. A.1 for an example of the illumination setup with the Thorlabs 'Cool-white' LED on. For a broader range of wavelengths, I add additional sources. (See the note two paragraphs above about additional sources.)

To continue, we need a sample oil-coupled to the 100x oil-immersion objective. Bring the *upper* interface of this sample into visual focus, as usual, using the eyepiece.[3] For the rest of this document, I'll use a quartz substrate (SPI Supplies, 0.18 mm thick, 1 in^2 area) as a reference.

A.1.3 Balancing the k distribution of excitation light

Turn the filter wheel to 'R' (for 'reflection') so that we're using the 50/50 beam splitter. Put the output to 'L' so that the collected light is projected out the left side of the microscope to the spectrometer. Open the spectrometer aperture so that the slit is

[2] I believe the precise distance from lens to diffuser film is *not* critical in this case. It should be *close* to f, but variation will likely only cause differences in the k-space distribution of excitation light which we normalize out during the data analysis anyway. What's most important is that the BFP image, e.g., Fig. A.2, *looks* like the polarized Fresnel reflection functions along the vertical and horizontal linecuts.

[3] I highly suggest starting with a clean quartz substrate, since this is an 'ideal' reference. This is what I've used since day 1, but it does have it's caveats (described later). Some day, a high-quality silver film might be used as a good reference sample.

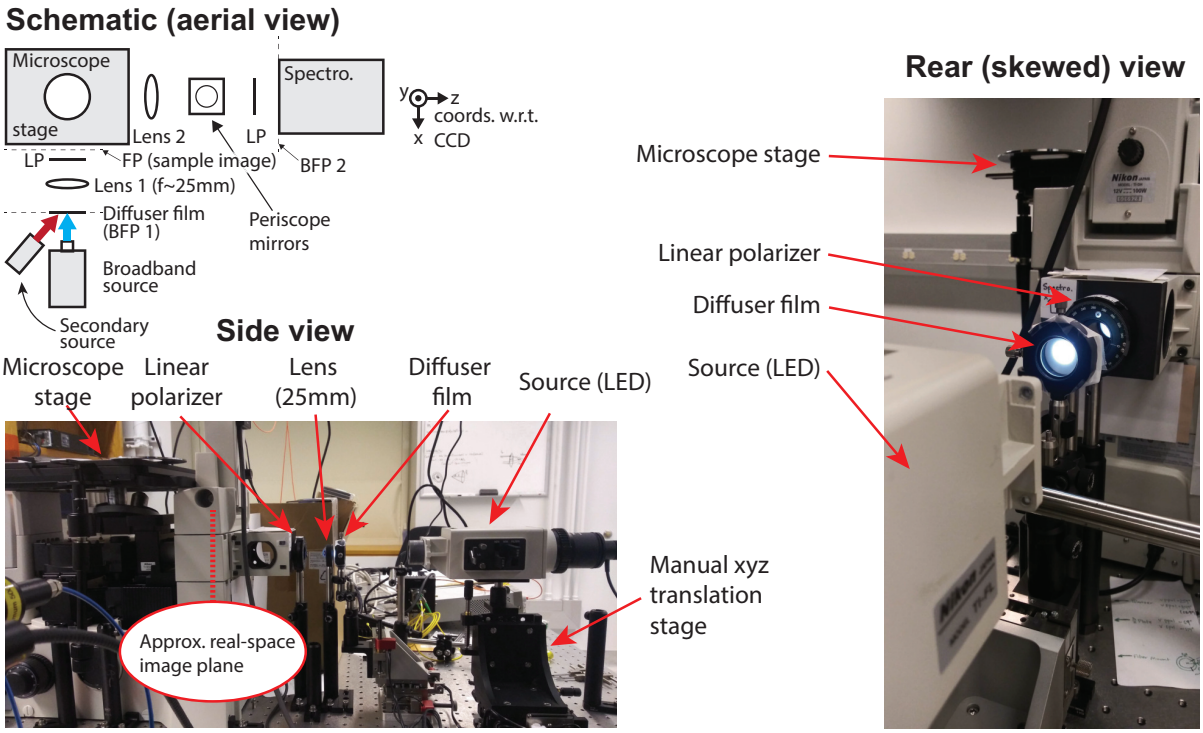

Figure A.1: Setup for momentum-resolved reflectometry. Top left is an aerial-view schematic. Bottom left is a real side-view image. Right side is a real skewed rear view image. In the schematic, two light sources are shown. Incident light is represented by colored arrows. BFPs ('conjugate BFPs') and real-space focal planes ('FP') are represented by dashed lines.

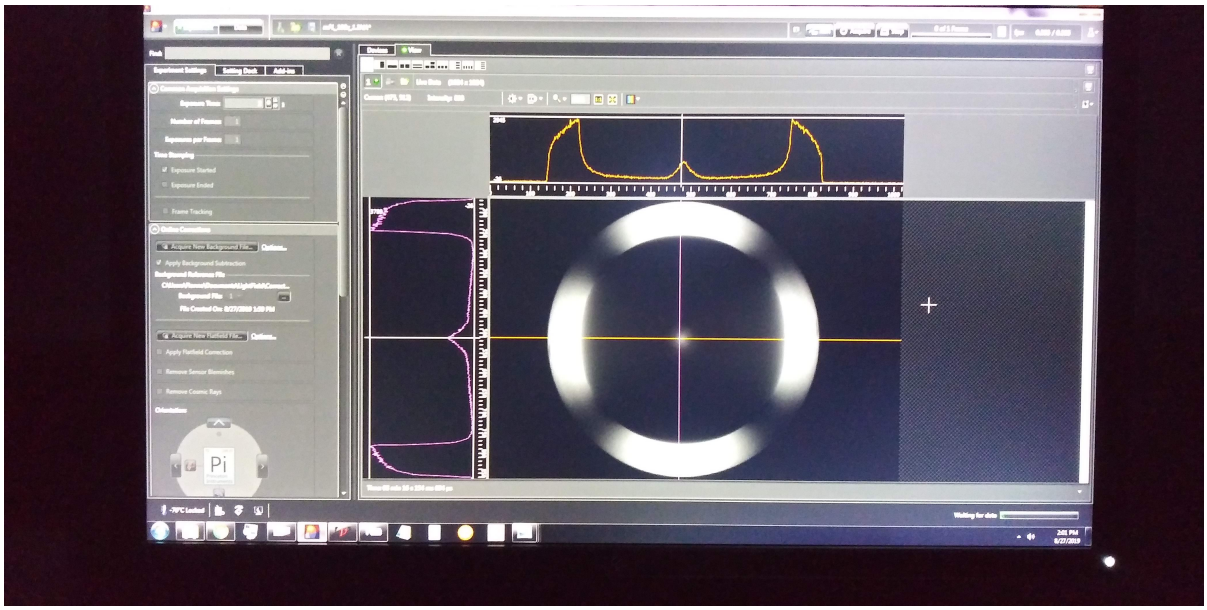

Figure A.2: Screenshot of LightField after much illumination alignment. This image was captured with 2s integration time, the 800nm blaze grating and a center wavelength of 0 nm. The spectrometer slit is not in place (duh). This image was taken with two linear polarizers in place — one near the source, and one immediately in front of the spectrometer entrance (see Fig. A.1); the one near the spectrometer entrance is y-oriented. The polarizer near the source is in the corresponding x orientation.

not in place. **In LightField, set the 'center wavelength' to 0 nm (i.e., reflection-mode) and the exposure time to 1s.** Start exposing repeated exposures with the 'Run' command. You should see an image like that in Fig. A.2. Click on the center of the image to view both horizontal and vertical linecuts of the image. Your image will likely *not* be as nice as the one in Fig. A.2... yet. Your image will likely be asymmetric both in the horizontal and vertical linecuts.

We will now balance the k-space distribution of excitation light. This is done by moving the source to change the distribution of light on the diffuser film (e.g., see Fig. A.1, lower right). For this purpose, I have put the LED on an manual xyz translation stage (Fig. A.1). I stand near the source while running continuous 1-2s exposures in LightField. I translate the source in x and y until the the horizontal and vertical linecuts look balanced to the best of my ability. 'Good alignment' is exemplified in Fig. A.2. The

image in Fig. A.2 was captured with an y-oriented LP at the entrance of the spectrometer. (The LP near the source is in the corresponding x orientation.) Notice that the vertical and horizontal linecuts thus strongly resemble the p- and s-polarized Fresnel reflection coefficients from a quartz/air interface. Good! If you are using multiple light sources, make sure ALL of them are balanced independently.

A.1.4 Make sure BFP is in focus

Though your image may be 'balanced', it may not yet be in prime focus. *Ensure your sample/air interface is still in focus through the eyepiece.*[4] We'll move the lens at the *output* of the microscope ('Lens 2' in Fig. A.1) in the z dimension to get the features as sharp as possible. The lens is on a z translation stage to make this easy. Don't be afraid to scan the z position over the whole range of the translation stage (about 5-10 mm) to ensure the best focus. Similar to balancing the light intensity, I run continuous 1-2 s exposures in LightField, pay close attention to the screen, and rotate the knob on the translation stage until the optimal focus is reached.

The p-polarized linecut is a very good feature for focusing; it should have a null (i.e., ideally zero counts) at the Brewster angle, a sharp maximum at the critical angle of total internal reflection (TIR; approx. 268 pixels above the center[5]), and a nearly vertical transition between these two points. (In reality, you'll see ∼20 counts at the Brewster angle with the current setup. At *best*, I've had about a 0.5-1.0% ratio between counts at the Brewster angle vs. counts at the critical angle maximum.) Simultaneously, the numerical aperture (NA) edge should be sharp (should span no more than 2-3 pixels).[6]

[4] I have noticed that changing temperatures and/or time lead to the system going out of focus over the course of several minutes. This seems to happen until everything is in equilibrium. I tend to keep the excitation sources illuminating the sample the whole time to keep things in this equilibrium.

[5] when using the 100x NA=1.3 objective and the 400 nm Bertrand lens between the spectrometer and the left port of the microscope

[6] The NA edge will likely look sharper on one side than it does on the other. In our setup, it typically

E.g., see Fig. A.2. Note that there is always a bright spot in the center (which we believe to be from internal reflections in the microscope); this is not a major problem for us.

A.1.5 Align the BFP to the entrance slit of the spectrometer

Now that the light source is set up and the system is focused, we will proceed to the crux of the measurement; collecting energy-momentum spectra. Ultimately we will be using the imaging spectrometer to separate the incoming light into its constituent wavelength components. To collect meaningful spectra, *the entrance slit of the spectrometer must be "in position".*[7] I will call this "up" since, for our Princeton IsoPlane spectrometer, we must pull the knob (at the entrance slit) up to put the aperture in place. In particular, we ultimately want an image such that the y-coordinate represents the k_y momentum (k_x=0) and the x-coordinate represents wavelength.

The aperture is a vertical slit. It is centered at some well-defined x-position with respect to the CCD camera. This x-position (basically) *cannot* be changed (unless by some delicate repositioning that should only be done by Princeton technician). The width of this slit, however, *can* be changed easily by rotating the Vernier dial/knob. We'll discuss this more a bit later.

We will now align the BFP to the center of this aperture slit. *Without changing anything further from the previous setup*, run short exposures (∼1-2 seconds) so that you can see a nice circular BFP image like in Fig. A.2. While running, *pull the aperture up* (into position). Now, on the monitor you should see only a vertical slit of light entering the spectrometer; see Fig. A.3. Make a mental note of the x-coordinate of this line. (It is typically *not* at the x-center of the CCD. Also likely, the up-down intensity distribution

looks sharper on the right side than on the left. In any case, up-down balance is more important than left-right balance, as ultimately the spectrometer aperture takes only a narrow vertical linecut about the center of the image.

[7]Please note that this is a common, if not essential, feature of all optical spectrometers!!!

will no longer be balanced; this is because the slit is not perfectly even in width from top to bottom. Later, we'll reposition the source to re-balance this.) Better yet, click on the screen and leave the cross-hairs at this x-position. We will now left/right center the 2D circular BFP over this slit. To do this, push the slit back down to see the whole circular 2D BFP. Use the upper periscope mirror knobs (see Fig. A.1 and Fig. A.4) to move the periscope mirror. This ultimately moves the BFP with respect to the CCD; one knob moves the BFP up/down, one knob moves the BFP left/right. Don't worry so much about up/down alignment, as long as the whole NA is visible on the CCD. *What is critical is the left/right alignment of the BFP relative to the slit x-position; get the x-center of the BFP precisely over the x-center of the slit.*

A.1.6 Measuring energy-momentum spectra

The system should now be in focus, aligned, and almost intensity-balanced. Put the entrance slit back up to see the vertical linecut once again. In the software, change the center wavelength to some range appropriate for the intended measurement. It is best to choose some center wavelength such that we can see the entire range of wavelengths used to illuminate the sample. For example, with the Thorlabs "cool-white" LED and the tabletop white light source, I use the 800nm grating with a center wavelength of 630 nm. With such settings, an energy-momentum reflection spectra should be visible. This energy-momentum spectrum should look something like that in Fig. A.5. In Fig. A.5, the two aforementioned light sources are being used, and the up/down intensity distribution has been re-balanced. Figs. A.6-A.7 show the contributions from each light source independently. For this illumination setup, I have the tabletop white-light source output connected to a fiber collimator; it is illuminating the diffuser film from just below the output of the "cool-white" LED. See schematic in Fig. A.1. *Run repeated ∼2s*

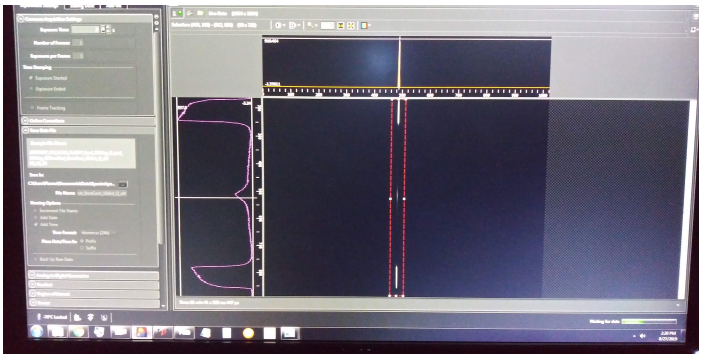

Figure A.3: Screenshot of LightField with spectrometer entrance slit in position. Notice that the up/down intensity distribution (see vertical linecut, on left of screen) is no longer balanced. We believe this is because the slit is not quite perfectly even in width from top to bottom.

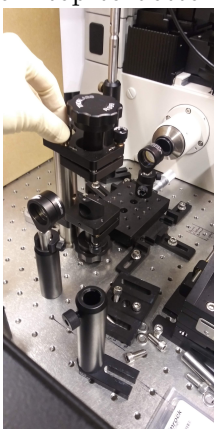

Figure A.4: Knobs on periscope mirrors. These can be used to carefully change the position of the BFP with respect to the CCD camera.

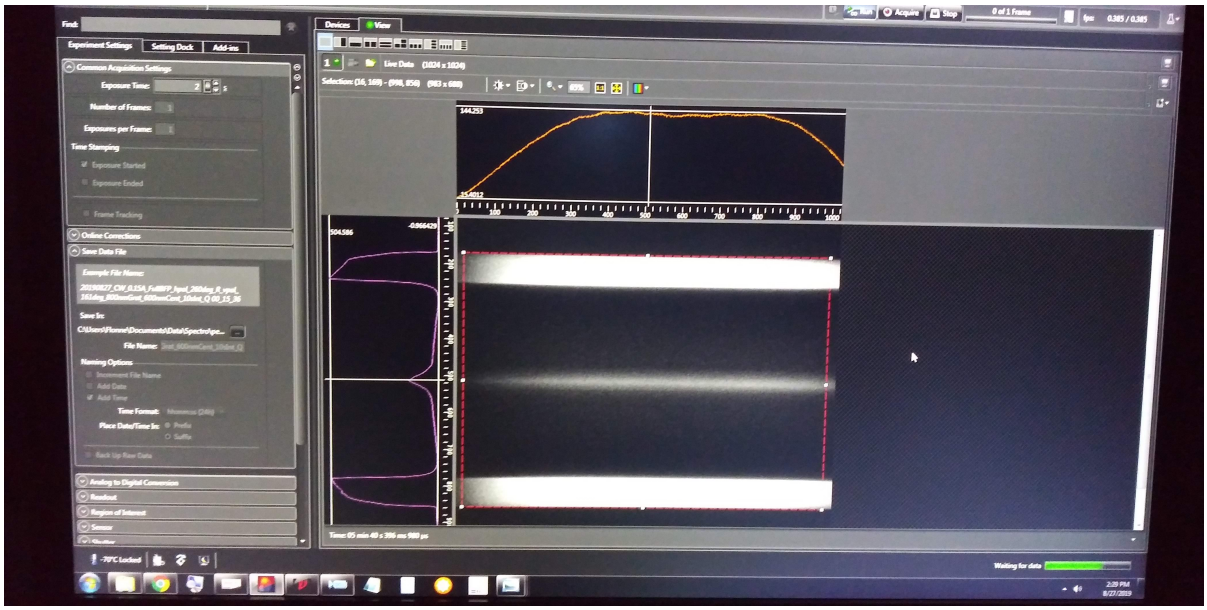

Figure A.5: Screenshot of a well-aligned p-polarized energy-momentum spectrum. This image was recorded with a 2s integration time. Two light sources were used: the "cool-white" LED (at ∼0.1A driving current) and the tabletop white-light source (intensity controlled to get the intensity balanced across all wavelengths). E.g., see Figs. A.6-A.7.

exposures and re-balance the up/down distribution of counts for all sources independently by moving the sources as you did the first time. Then get the intensity balanced across all wavelengths by varying the incident powers of each source carefully. For both of these processes, I tend to average over all columns and over all rows by dragging a box over the whole region of interest (see Fig. A.5).

The system is ready to acquire good mR spectra. Two images will be captured for the reference (and analogously for all samples) — one for s-polarization (x-oriented polarizer) and one for p-polarization (y-oriented polarizer). For good spectra, the integration time must be chosen wisely; *the maximum counts at any single pixel must be large, but must never exceed ≈60,000.* E.g., ≈30,000 counts is fine. To determine the integration time, I typically run a 10 second exposure for *both* polarizations. Open these images and find the maximum count rate in the image (it could in principle be at any pixel,

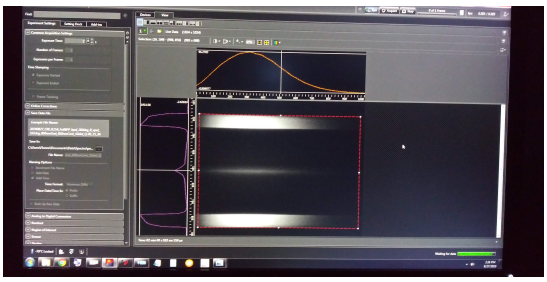

Figure A.6: Same as Fig. A.5, but using only the "cool-white" LED.

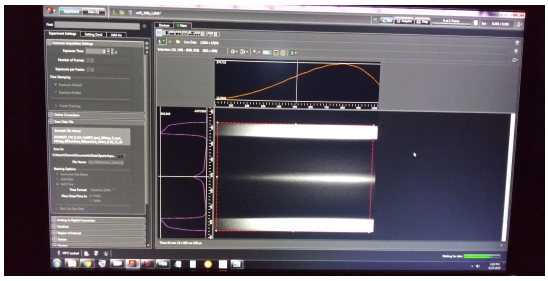

Figure A.7: Same as Fig. A.5, but using only the tabletop white light source.

and is likely somewhere along the row representing the critical angle of TIR for both polarizations). *Use this count rate and the known integration time to estimate how long you must integrate to get ≈30,000 max counts at the same pixel. (This is not complicated math, just do it in your head; you're better to undershoot than get too close.)* I often find that I need several hundred seconds of integration (∼5-10 minutes) for a good image with ≈30,000-50,000 counts. Acquire the spectra, one for each polarization. Make sure the computer monitor is *off* during this exposure.[8]

Now that you have two good mR spectra for the reference with two unique polarizations, ***without moving or changing anything else whatsoever (this part is extremely important!!) remove the reference, put the sample in place****, and perform the identical process for the sample. For such long exposures, it is important to use preventative measures against sample degradation under ambient conditions. Use N2 gas flow over the sample.* At the current time, the lab has a cute little N2 purge box for this purpose. When used properly, I will see no obvious signs of light-induced degradation over the course of ≈10 min. exposures. As a sanity check after any given measurement, you should check the mR image of the sample; *at y-coordinates within*

[8]It's a very good idea to collect an up-to-date good background reference file for the particular setup. That is, with no excitation light entering the spectrometer (by whatever means necessary), collect and apply a background reference file in the software. For this, there is no need to do a very long exposure; keep it to several seconds long. The system apparently scales with longer/shorter integration times accordingly.

the region of TIR, the maximum counts for the sample should ***never*** *exceed that of the reference, anywhere*![9] If you find something weird in this regard, you probably have no choice but to re-measure both the reference and sample again, taking greater precaution to keep things in focus and to not change anything else in the system. Do this again for any other samples you have; no need for a new reference unless you change anything about the illumination or collection conditions.

There you go, your measurements are complete! Next we'll discuss how to analyze this data using a Python script that I have written, using the package *spe2py*.[10] I won't describe how to implement *spe2py* since this is well documented on the web and/or requires some finesse and/or personal preference re. where to install, etc...

A.2 Analyzing the data to extract optical constants

A.2.1 Film thickness

To analyze this data, we need to know the film thicknesses. The analysis code also takes into account some degree of surface roughness (to be described later), so it is ideal to have an estimate of the thickness of the "surface roughness layer". For both purposes, I use atomic force microscopy (AFM) with a "needle-scratch" method; I use a needle and literally scratch a line into the film with a medical-quality needle (delicately, but firmly and controllably). Assuming the sample is on a good substrate (e.g., Si, fused silica, sapphire) and that you aren't completely reckless, this should not damage the substrate. These scratches are typically ∼20-40 μm across, and are easily seen under AFM camera (or any microscope). I then measure directly over the step created by the

[9] This is because TIR with a non-absorbing reference *defines* R=1, and no reflection can ever be larger than 1. In practice, you might find a few pixels with several hundred excess counts over the reference, but this excess should be very very small, like ∼100/30,000≈0.3%.

[10] https://pypi.org/project/spe2py/#description

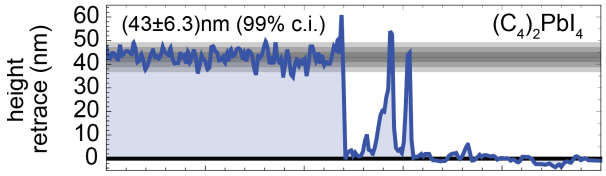

Figure A.8: AFM data and summary analysis. Film thickness is defined as the z-distance from the substrate (z=0 nm) to the *average* film height (center of gray band at 43 nm). The max. and min. film thicknesses over the scanned range are ≈43+6.3nm and ≈43-6.3nm, respectively. From ref. [17].

scratch so that I can see the very flat substrate *and* the film surface in a single image. Beyond these details, getting this information is into AFM skill territory and thus won't be described much more in this document. The critical point is you need to know the film thickness and the surface roughness. AFM data and typical thickness/roughness analysis of a perovskite thin film is shown in Fig. A.8.

A.2.2 Using the Python code

The analysis code (available as thesis Supplemental Files; please note that it requires the spe2py package, available on GitHub) has been written for Python 3 (it has been successfully running in IPython 5.3.0 with Python 3.5.3). This code has been developed using a Mac, and I cannot say how to use it on Windows. In principle is should work, but there are almost *always* issues with syntax when using across platforms. The code is not particularly pretty, but it gives good results and has a little bit of interactive user functionality to it. Here, we'll go over the most basic operation on the "user's" end, and not worry much about the inner workings of the code.

Overview of the logic flow of the code

Here's a basic workflow of the code:

1. We start with 2D images that represents reflected counts, $C(x, y)$, as a function of

pixel coordinates, (x, y).

2. These data are pushed into a function called 'do()'. (This 'does' everything we need to have done.)

3. By analyzing vertical (i.e., y- or, ultimately, k_y dimension) linecuts from both the reference and sample data, the user identifies the y-coordinate of certain physical features (specifically, the critical angles of TIR) that are used to scale from y (pixels) to k_y (the in-plane momentum of the collected light). The wavelengths corresponding the various x-values are already known from the .spe image data. $C(x, y)$ is thus converted to $C(\lambda, k_y)$. We have one such function for each file (one for each polarization for the reference, one for each polarization for the sample).

4. $C(\lambda, k_y)$ is vertically scaled by a *constant* according to the reference data. For s-polarization, the scaling is defined to set the *maximum* counts (around the critical angle of total internal reflection) to a value of 1.0. E.g., let the maximum value of $C(\lambda, k_y)$ be called v. A new scaled function $c(\lambda, k_y)$ is defined by $c(\lambda, k_y) = C(\lambda, k_y)/v$. This is appropriate for the reference data only, since at (and beyond) the critical angle of TIR, the reflectance is formally equal to 1.0. For p-polarization and using a dielectric single-interface reference (e.g., a quartz coverslip as used in all of the data presented in this document), it is convenient to define the constant scaling factor for some specific $k_{||}$ near normal. This is because "corrections" (discussed below) around the Brewster angle are, practically speaking, not well-defined since the reference data formally goes to zero there. In this way, the data is not corrected around the Brewster angle, yet the measured reflectance is still the best representation of the theoretical reflectance. (Empirically, experimenting with various scaling methods indicates that this is indeed the best way.)

5. By comparing $c(\lambda, k_y)$ of the *reference* to theoretical curves for the reference,[11] $c(\lambda, k_y)$ is converted into an experimental *reflectance* function, $R(\lambda, k_y)$. Values of R lie within the range {0,1}. This is performed individually for each polarization.

6. The relationship between C and R defines a "scaling function" (or "correction function"), $s(\lambda, k_y)$, defined by $s(\lambda, k_y) = c(\lambda, k_y)/R(\lambda, k_y)$. One such function exists for each polarization. These scaling functions are then applied to the *sample's* $c(\lambda, k_y)$ (again, one for each polarization) in order to get the *sample's* reflectance $R(\lambda, k_y)$ (again, one for each polarization). Let us call these $R^s_{\text{sample}}(\lambda, k_y)$ and $R^p_{\text{sample}}(\lambda, k_y)$. Again, this correction is not applied around the Brewster angle in p-polarization because the theoretical reflectance goes to zero there.

7. $R^s_{\text{sample}}(\lambda, k_y)$ is compared to theoretical reflectance lineshapes for the thin-film (two-interface) geometry.[12] Because the user inputs thickness information, and because the measurement uses purely s-polarized light, the only two free parameters in this problem are the two components of the in-plane (IP) complex refractive index (equivalently, permittivity): $\tilde{n}_{\text{o}} = n_{\text{o}} + ik_{\text{o}}$. Using (currently) *scipy.optimize.curve_fit*, the best fit is found by numerical minimization with respect to the two parameters $(n_{\text{o}}, k_{\text{o}})$. The Python-savvy user should feel free to try other fitting algorithms. Confidence intervals are determined from the covariance matrix of the fits.

8. $R^p_{\text{sample}}(\lambda, k_y)$ is then compared to theoretical reflectance lineshapes for the thin-film

[11] The theoretical reflection functions are "smeared" in the k_y dimension to account for finite imaging resolution. Practically speaking, what this means is the that $R(\lambda, k_y)$ is convoluted with a gaussian in the k_y coordinate, corresponding to approximately three pixels at the level of the sensor. This three-pixel value is an estimate from years of experience with the system, from which I've convinced myself that no features are ever resolved within three pixels.

[12] Again, these lineshapes are "smeared". As before, they're smeared in the k_y dimension. The sample reflectance function is also "smeared" across thicknesses to account for the surface roughness in an incoherent manner; this again amounts to a convolution with a gaussian in *thickness*, with a width according to user input from the surface RMS measurements.

(two-interface) geometry. IP optical constants are *input*[13], and the remaining two free parameters — the OP optical constants, $\tilde{n}_e = n_e + ik_e$ — are fit. Confidence intervals are determined from the covariance matrix of the fits.[14]

9. The results are saved in both tabulated form (a .csv file with fits and confidence intervals for all wavelengths included in the fit routine) and visual form (.eps images of the individual fits as well as dispersion plots).

Comments re. fitting

The IP fits from *s*-polarized reflectance are quite robust at any wavelength, even outside absorption bands. However, OP fits from *p*-polarized reflectance sometimes still struggle, especially outside of absorptive regions. However, the most recent developments of this analysis suggest that more robust OP fits can be obtained by re-defining the scaling function (described as point #4 above) and fitting both IP and OP constants simultaneously (described in point #8 above). This is presumably because the only unique feature is Brewster's angle, fits around which (I suppose) are quite sensitive to inevitable experimental errors. Further, there is a bit of a fundamental "problem" with the function $s(\lambda, k_y)$ around the Brewster's angle, since counts *theoretically* go to zero there. Because of this, the current implementation does *not* correct the function $c^p(\lambda, k_y)$ in that region for *p*-polarization. It would be ideal to someday have a better reference, e.g., high-quality Ag thick film that does not have these issues. In general, the *p*-polarized reflectance is maximally sensitive to $\tilde{n}_e$ in some region around the critical

[13]This is performed automatically — the user does not need to manually do this.

[14]I will note that there *may* be some "theoretical" issues with determining confidence intervals via the covariance matrix for the case at hand, since there *seems* to be some parameter correlation between n_e and k_e. See Appendix C of ref. [16]. All of the work presented in this document were performed in this manner. More recent developments of this technique show that better fits may be obtained by simultaneously fitting *p*-polarized data for both IP and OP optical constants simultaneously. In this case, one may put in the *s*-polarized IP fits as initialization values. It is interesting to see how the two results compare.

angle of TIR, and weakly sensitive outside this region. When fitting for p-polarized data for OP permittivities only, fits of $R^p(\lambda, k_y)$ should thus only be performed at angles around TIR, e.g., $k_{||}/k_0 \in [0.85, 1.05]$. When fitting p-polarized data for both IP and OP permittivities simultaneously, one may include the entire NA for robust fits. One final subtlety — counts in the immediate vicinity of TIR are excluded for *both* polarizations because the theoretical function becomes infinitely steep at $k_{||}/k_0 = 1$. The specific ranges that are excluded/included can be found in the dictionary *exp_params* and in the function *norm_and_truncate_single_dataset()*, and can, of course, be varied for the case at hand at the user's desire. I have found that the current values work well under most circumstances.

Detailed overview of code from a user's perspective

For this guide, I'll be using a code that is used to analyze HA_2PbI_4 thin film optical constants. I always begin by making a new full directory with all working code within. I.e., copy and paste a working example, and rename the new directory with something specific to the project/material/etc. In a terminal, go into the directory with the analysis code. Start Python. In the script, all of the sample-specific variables are included in the dictionary *exp_params*. The most important sample-specific inputs here are the data file names (*"spol_ref_file"*, *"spol_sample_file"*, *"ppol_ref_file"*, and *"ppol_sample_file"*), the sample thickness (*"thickness"*) and rms thickness (*"rms_thickness"*). Specify the latter two according to AFM measurements; *"thickness"* is defined as the *average* sample thickness; *rm_thickness* is defined to be the $+/-3\sigma$ range (e.g., Fig. A.8). Optional, but beneficial, input the x-coordinates corresponding to the min. and max. wavelengths of the data you'd like to analyze in the definition *"cols"*. E.g., using Fig. A.5 as an example, I would use the full horizontal range and set *"cols"*=(0,1023). For a narrower illumination range, just to save time and later processing, I would specify these differently.

The user can also choose the number of wavelengths to subsample in the definition *"num_wavelengths"*.

Upon first use of the code for any given sample, comment out the definitions *"crits_s"* and *"crits_p"*. In Python, run the analysis script:

```
In [1]: run analyze_reflection_spectral.py
```

If all is fine, this should return no errors and offer a new input line 'In [2]'. Run the 'do()' method to begin the analysis:

```
In [3]: do()
```

If there are no problems, you should see in the terminal a message confirming the loading of the four files, followed by a prompt to begin data scaling:

```
x-coordinate (min, max): (45, 1023)
Identify the RIGHT critical angle...
```

Simultaneously, a Python interface should pop up with a plot that looks like a vertical linecut of the s-polarized reflectance, e.g., Fig. A.9. As the instructions suggest, identify the x-coordinate of the *right* critical angle (i.e., the critical angle on the *right* half of the image). From experience (just trust me here for now), *the critical angle is not necessarily the obvious peak*.[15] To this end, the *upper* horizontal black dashed line is intended to *approx* intersect the curve at the critical angle. (This is not a hard rule, but a guide.) I typically zoom in to find this coordinate (Fig. A.10); for example, in the example data, it is at x=793. Once you have made a mental note of this coordinate, close the window and the terminal will prompt:

```
Specify the RIGHT critical angle:
```

[15]This can be understood by the convolution effect mentioned earlier; an infinitely sharp feature with R=1 on the right side and R very small on the left side is will be pushed to smaller values.

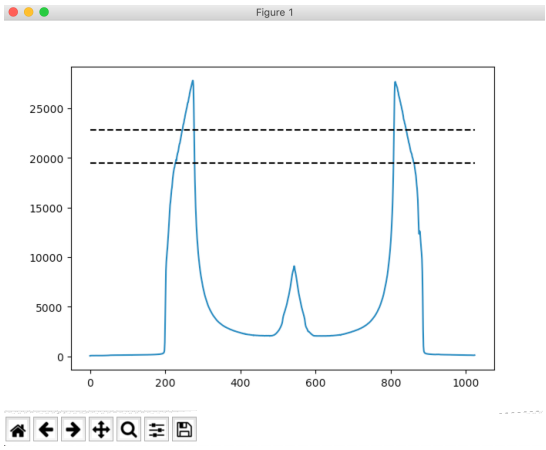

Figure A.9:

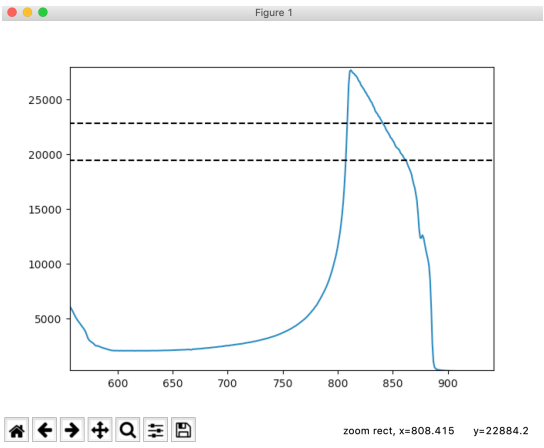

Figure A.10:

Type in the x-coordinate, e.g., 793, and press enter. You will then be prompted to do the same for the *left* side, and then for both sides of the sample data. This needs no further instruction. Note that in the sample data, your choice of x-coordinates *may* (but need not necessarily) vary from the reference data. (Often, it is a bit *closer* to the peak than in the reference case.) An alternative good option — just input the same coordinates from the reference. If the measurement was performed properly, the coordinates should be the same. For this example, I input 793 and 239 for the right and left side, respectively, for both sample and reference.

Immediately after this, you'll have to do the same for p-polarized data. Follow the same instructions; however, in this case, the *lower* dashed black line is intended as the guide. (Based upon arguments in the footnote, can you explain why it's lower in this case?) In principle, x-coordinates from the s-polarized analysis can be used, however, I often notice non-negligible differences between the two. I'd suggest uniquely picking out the x-coordinates for the p-polarized data. For this example, I input 673.8 and 239.1 for the right and left side, respectively, for both sample and reference.

After entering this information, the code will print some information into the terminal based upon user input. Of particular interest are the lines that read:

```
Center and Averaged critical angle: crits = (516, 277)
```

When I'm done with this initialization, I copy and paste these coordinates into the Python script under the dictionary definitions *"crits_s"* and *"crits_p"* as such (and after refining a bit):

```
``crits_s" : ((516.007, 277.075), (515.700, 277.075)),
``crits_p" : ((516.507, 277.375), (515.957, 276.875)),
```

You'll notice this form of 'crits*' is different than what you input; these are in the form (center, critical angle in pixels). This copy-and-paste step is for record-keeping, as well as ease later if I need to re-run the code. These values can, of course, be modified as needed if something in the fits looks obvious wrong.

The code should begin to run and will not need any more input from the user. There is some verbose output to inform the user about the current status. You will see that the process roughly follows the steps outlined above. On my computer, the normalization steps take a few (≈3-4) minutes and the fitting takes ≈1-5 seconds per wavelength (and varies significantly amongst different wavelengths). If all goes well, the code should chug along until all wavelengths have been fit, and then produce a bunch of plots and a .csv file, all saved into the working directory. The .csv file is called 'perms_fits.csv'; it contain many columns corresponding to, e.g., film thicknesses (nm), wavelengths (nm), Re. and Im. parts of optical constants (both in terms of refractive index and permittivity), and confidence intervals. This files can/should be renamed with a unique label appropriate for the particular sample/analysis. There you have it! Optical constants!

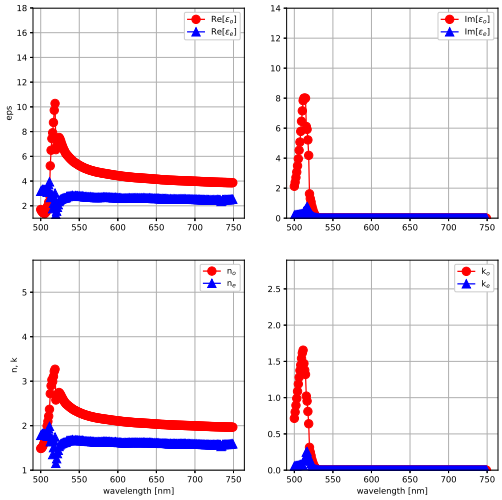

Figure A.11:

A.3 Incorporating mR fits into VASE

This section describes how to combine mR results with variable-angle spectroscopic ellipsometry (VASE) modeling techniques. This will be referred to as the 'joint' method. According to VASE analysis techniques, 'Model' will refer to the layer structure and specific anisotropies assumed for each layer within, e.g., CompleteEASE; 'Material' will refer to the 3-column .mat files used to represent the wavelength- or energy-dependent optical constants (derived by whatever method). There are a few distinct stages including: collecting ellipsometry data; performing infrared Cauchy fits; combining VASE and mR data; deriving an oscillator model from the combined data; refining the model. (An alternative outline of this procedure is described in ref. [17] in Supporting Information Sect. S2, especially around Fig. S2.)

A.3.1 Fitting deeply sub-bandgap uniaxial optical constants with ellipsometry

Fit deeply sub-bandgap uniaxial optical constants from films spun on Si substrates using a Cauchy material for both IP and OP directions. Identical measurements should be made on both 'bare' Si substrates (including native oxide) and identical Si substrates with films. Films for this particular analysis should be *relatively* thick (e.g., ≈100-200 nm vs. ≈50 nm used for mR), *unless this makes the surface roughness dramatically worse*; surface roughness should still ideally be no greater than ≈10-20 nm total. While thick films are prohibitive for mR (measurements over the absorptive regions yield very small values for R), the range of interest for initial ellipsometry fits is deeply sub-bandgap, around ≈1000-1500 nm, where there is very little absorption. Further, the greater optical path length seems to improve the sensitivity of the ellipsometry technique. Namely, some light "Fabry-Perot"-like fringes help the fit. E.g., see ref. [21] Fig. S11.[16] For each sample, I will measure at about 4-5 different locations/rotations to ensure consistency, and for later statistical analyses.

Fit the bare substrate (Si + oxide) data to a two-layer model including both ('Substrate') Si and ('Layer #1') native oxide (typically ≈2.5 nm thick). Refer to the lower two layers in the schematic structure in Fig. A.12. For this, use built-in Si (e.g., I typically use Si_JAW) and SiO2 models (e.g., SiO2_JAW). (I believe then only the oxide thickness in this model is fit.) This fit can be performed over an arbitrarily large range of wavelengths. This removes the one free parameter associated with the substrate.

For thin-film samples, the ellipsometry analysis/model should include an interfacial (roughness) layer with a non-linear (exponential/gaussian) grade type. I use the Bruggeman effective medium approximation with an "Exponent" = 3 for this layer. This model

[16]Note that with films ≈200 nm thick, you will never see so many reflectance fringes. You might see just one with a film of 200 nm thickness.

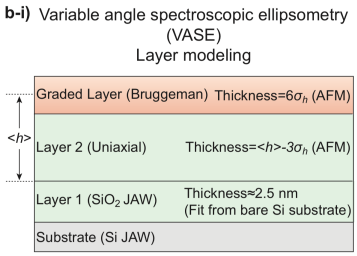

Figure A.12:

can be loaded from a previously constructed *.SESnap file.[17] The essential fit parameters between the interface and film layers must be properly coupled; to couple parameters unambiguously, layer parameters must be renamed uniquely. This parameters can be coupled by the following: *For both layers #2 (film) #3 (roughness), expand the 'Material' tab to show both 'Ordinary OC' and 'Extra-ordinary OC' materials. Right-click on each of these materials and select "Rename Layer and Fit Parameters".* I typically *uncheck* the 'Rename Layer' option, so that only the parameters associated with that layer are renamed. Call them something like '*_Layer_3_IP' and '*_Layer_3_OP', respectively. Then, in 'MODEL Options', expand the 'Parameter Coupling' tab. Click 'Add'. The goal is to *equate* (i.e., using a ratio of 1.0) the Layer #3 and Layer #2 parameters, since they should represent the same material. An example for Cauchy fits of the thin film with graded interface layer is shown in Fig. A.13. Select the fit range so that we absolutely exclude absorptive regions of the film; e.g., for an absorption onset at 500 nm, I would exclude wavelengths shorter than 750 nm. There's still plenty of infrared data to fit.

This fitting technique works best when the graded layer thickness is *assumed* (i.e., *not fit*) to take the value of the roughness as determined by, e.g., AFM. Specifically, the thickness should be set and locked to the z-distance between max. and min. of the surface roughness.[18] To minimize the number of free parameters, thin film samples should

[17]Note: loading a Snapshot also loads the data associated with that SESnap; manually load new data after loading the SESnap.

[18]Keep in mind that Layer #2 thickness in the VASE model should be approx. equivalent to (mean

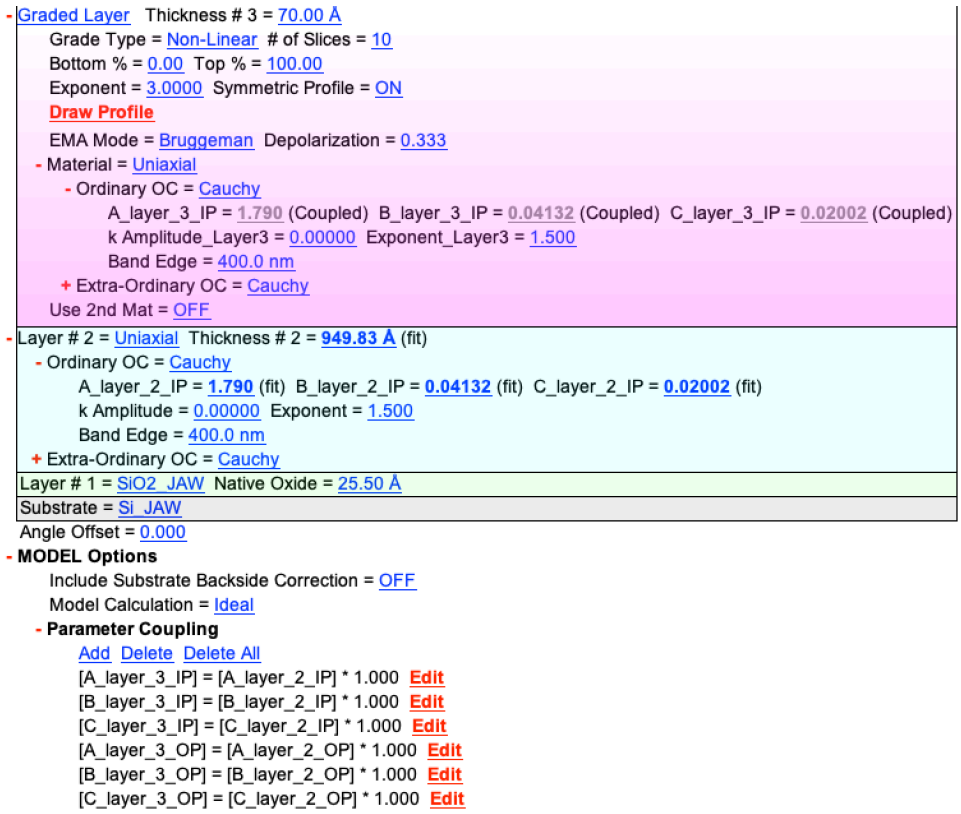

Figure A.13: Screenshot demonstrating parameter coupling of IP and OP parameters of a uniaxial Cauchy model fit to a thin film with a surface roughness layer (i.e., 'graded interface layer'). Notice in the purple box ('Layer #3') that the three parameters are grayed out with the label '(Coupled)' after the fit value. In contrast, the ones in the green box ('Layer #2') are labeled with '(fit)'.

be modeled/fit with *input* substrate parameters (determined from the above steps). *Film thicknesses should be input* (e.g., from AFM), but can then be allowed to vary within a reasonable range (e.g., 1-3 RMS thickness) during fitting.[19] Typically, many such measurements on the same sample at/with different positions/rotations return very similar IP constants; in contrast, OP constants *may* vary substantially. (In a few cases, however, I've found some very consistent results.) Fit all such data (e.g., above I suggested measuring the same film 4-5 times with different rotations) to the same model.

Save these Cauchy optical constants by right-clicking on the material and 'Save Layer Optical Constants' as 'Tabulated'. The Ordinary and Extraordinary components can be saved individually (I typically do this) or as a single uniaxial material. These can/should be saved into a user-created directory within '*/CompleteEASE/MAT/'. The resulting files are by default saved in terms of (Angstrom, E1E2).[20] If the IP or OP constants vary significantly, multiple such files can be saved and one should then perform (as specified later) parameterized fits using, e.g., max. and min. of these values or as otherwise deemed statistically appropriate.

A.3.2 Converting mR results into a .mat material file

Save the desired mR results into a tab-delimited 3-column text file with the extension '.mat' (e.g., 'nk_BAMAPbI-n1_IP_mR.mat') in the directory '*/CompleteEASE/MAT/'. **THERE ARE SOME IMPORTANT IDIOSYNCRACIES TO MAKE THIS WORK PROPERLY!** Here's one way that works: Open 'perms_fits_*.csv' from the Python 'analyze_reflection' script. In the desired '*/MAT/' directory, create a new .csv with the desired 3 columns (e.g., wavelength, re_eo, im_eo), and save this file as a .csv.

thickness) − (1/2)×(total surface roughness thickness.

[19] I have found in the best cases that the thicknesses returned from ellipsometry with this technique agree within +/-5 nm of those measured by AFM, which likely lies within the range of typical variations of the sample thickness with position.

[20] I do not know if this can be changed.

Change the extension to '.mat'. Open this in a standard text editor and perform a find/replace operation, converting all ',' into ' '.[21] *Note: saving as a tab-delimited straight from Excel does not seem to work properly!* These .mat files allow (require?) various header formats. The preferred one for my purposes is a 3-row header including: (1) a basic description of the material that can be literally anything you'd like; (2) units for horizontal axis (i.e., nm or eV); (3) the quantities associated with the following two columns (e.g., nk or E1E2). Since CompleteEASE saves the Cauchy material as E1E2, it is most convenient to use re_e and im_e columns from 'perms_fits.csv'. An example header is as follows:

```
RAD input - BA2PbI4 IP 0.07M 8k RPM on fused silica 2019/03/03
nm
E1E2
```

One such file is created for OP constants and one such file is created for OP constants.

A.3.3 Combining mR and ellipsometry into a unified model

For both IP and OP constants, create another .mat that includes *both* mR and SE Cauchy fits, e.g., 'nk_BAMAPbI-n1_IP_mR+Cauchy.mat'. *Ensure wavelength units are the same between both files!* CompleteEASE exports optical constants in units of Angstrom; I don't yet know how to export material optical constants in units of nm. Because of this, I only include ∼5-10 data points from the Cauchy material (e.g., every 100 nm), and change the units manually by moving the decimal place. The Cauchy values won't align perfectly well with the mR values, but, they should agree reasonably well if we're doing our measurements correctly. This doesn't matter so much, as this file is primarily intended to later help us construct an oscillator model, which will eventually

[21] Tab can be used as a replace character by copying/pasting a tab from any window.

be refined.[22]

A.3.4 Parameterizing the material into an oscillator model

Load your material into any CompleteEASE model, preferably the one you have constructed for the Cauchy fitting routine. Load the desired new material (created in previous steps).[23] Visualize (n,k vs. nm) by right-clicking on the material. Both IP and OP can be visualized simultaneously by using a Uniaxial layer (e.g., the one used to fit the Cauchy model in the first place) and choosing for 'Ordinary OC' and 'Extra-Ordinary OC' the IP and OP materials, respectively, that you just constructed. *Ensure that these plots make sense*, at least approximately. E.g., ensure the range being viewed includes only the range of the results included in the .mat file. (View range is changed by changing the 'Limit Wvl. for Fit' Range in 'FIT Options' and clicking 'Fit' to activate it.) Otherwise, the viewed results will be interpolated and likely will not make sense.) If desired, save these steps as CompleteEASE Snapshots.

Right click on a specific material (e.g., 'Ordinary OC' or 'Extra-Ordinary OC', the ones you just created and loaded). Select 'Parameterize Layer'. A new window should pop up, and all of the tools of SE analyses are available to construct a material model (Fig. A.14). If one is analyzing similar materials, previously parameterized materials may be loaded and re-fit. E.g., for PEA2PbI4, I load a Tauc-Lorentz parameterized material previously determined for BA2PbI4 and immediately find a decent representation. In general, at this point, the user must take full advantage of whatever cunning and artistry is available to them. Typically, IP constants should be fit first, as they are most accurately determined a priori (i.e., from mR). Save this new material in both Parameterized and Tabulated forms in the respective folder. As usual, the tabulated form is in terms of

[22]Note: Cauchy OP fits usually differ significantly from those of mR. Do not be alarmed.
[23]This is done by selecting your .mat file to represent one of the layers.

(Angstrom, E1E2).

Perform such a parameterization for both IP and OP materials. Typically (but *not* always) OP materials are well described by the same *model* as the corresponding IP materials, related simply by changes in amplitudes, broadening, Einf, and UV Pole Amps.[24] Unfortunately, the Re. part of the OP constants is typically spurious from mR, and thus the OP parameterization requires significantly more work. For example, one should fit the model parameters to *only* the imaginary part to determine the broadening and amplitude of the OP oscillator (Fig. A.15). In line with my general philosophy — *start with the fewest fit parameters possible.* For this purpose, Einf and other parameters not directly related to E2 should *not* be fit at this stage. In Fig. A.15, you can see how to fit to the imaginary component only. In this example, you can see that the only active fit parameter is the OP oscillator amplitude. For the time being, manually vary Einf, etc... to constant values to get E1 to agree with the infrared values of the material (Fig. A.16). Again, some artistry is needed here. The remaining values can later be "globally" fit, as described later.

Finally, refine the model. Einf and UV Pole Amps. can be refined by fitting these parameters to the entire SE dataset. *Again, if you desire to go this route, start with the minimal set of fit parameters.* We might consider Einf's (for both IP and OP materials) as the "minimal set"; include thickness again if you're feelin' a bit energetic; include oscillator amplitudes if you want to make things *really* zesty. To fit the whatever free parameters you choose, ensure parameters are properly coupled between interface and film layers as described in the previous section. Typically, at this point, Delta and Psi are reasonably well represented by this model and you might call it a day. Stay simple, at least to begin.

[24]UV Pole energies seem to be fairly insignificant and should be left invariant between IP and OP materials, again just to minimize fit parameters.

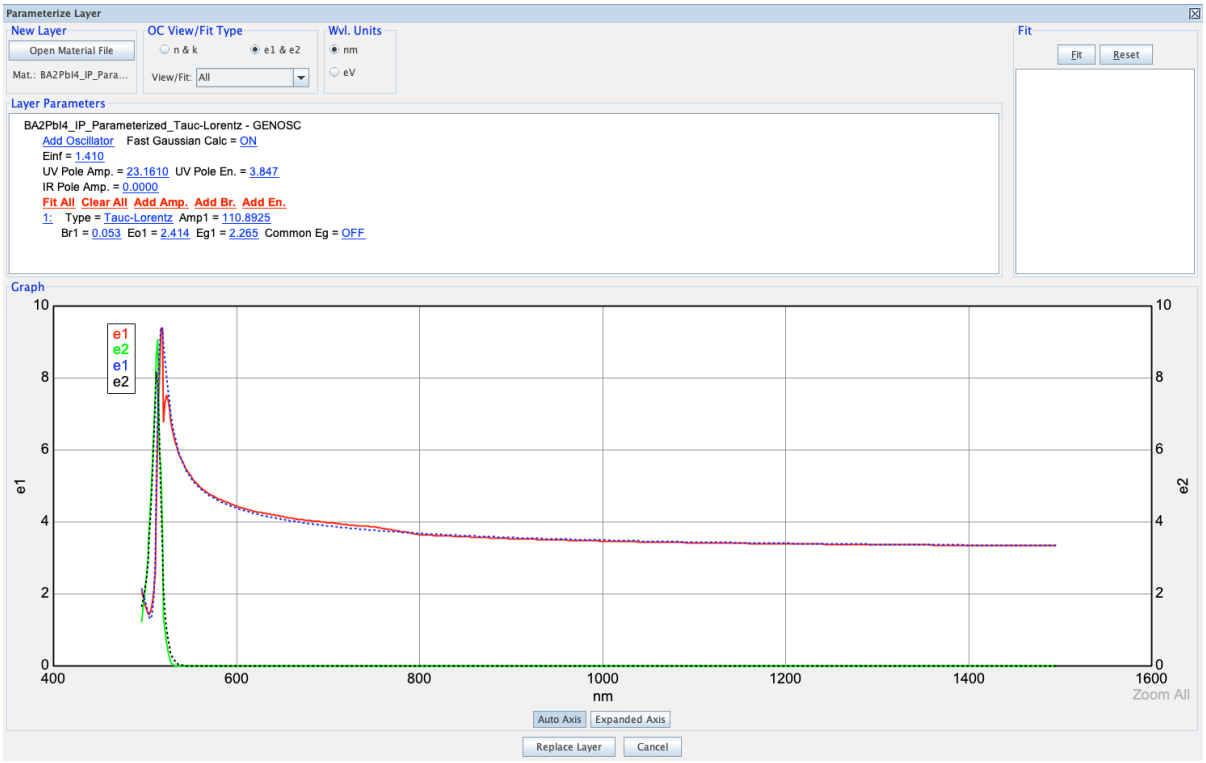
Parameterize Layer
New Layer
Open Material File
Mat.: BA2PbI4_IP_Para...
OC View/Fit Type
n & k
e1 & e2
View/Fit: All
Wvl. Units
nm
eV
Fit
Fit
Reset
Layer Parameters
BA2PbI4_IP_Parameterized_Tauc-Lorentz - GENOSC
Add Oscillator Fast Gaussian Calc = ON
Einf = 1.410
UV Pole Amp. = 23.1610 UV Pole En. = 3.847
IR Pole Amp. = 0.0000
Fit All Clear All Add Amp. Add Br. Add En.
1: Type = Tauc-Lorentz Amp1 = 110.8925
Br1 = 0.053 Eo1 = 2.414 Eg1 = 2.265 Common Eg = OFF
Graph
e1
e2
e1
e2
e1
e2
nm
Zoom All
Auto Axis
Expanded Axis
Replace Layer
Cancel

Figure A.14:

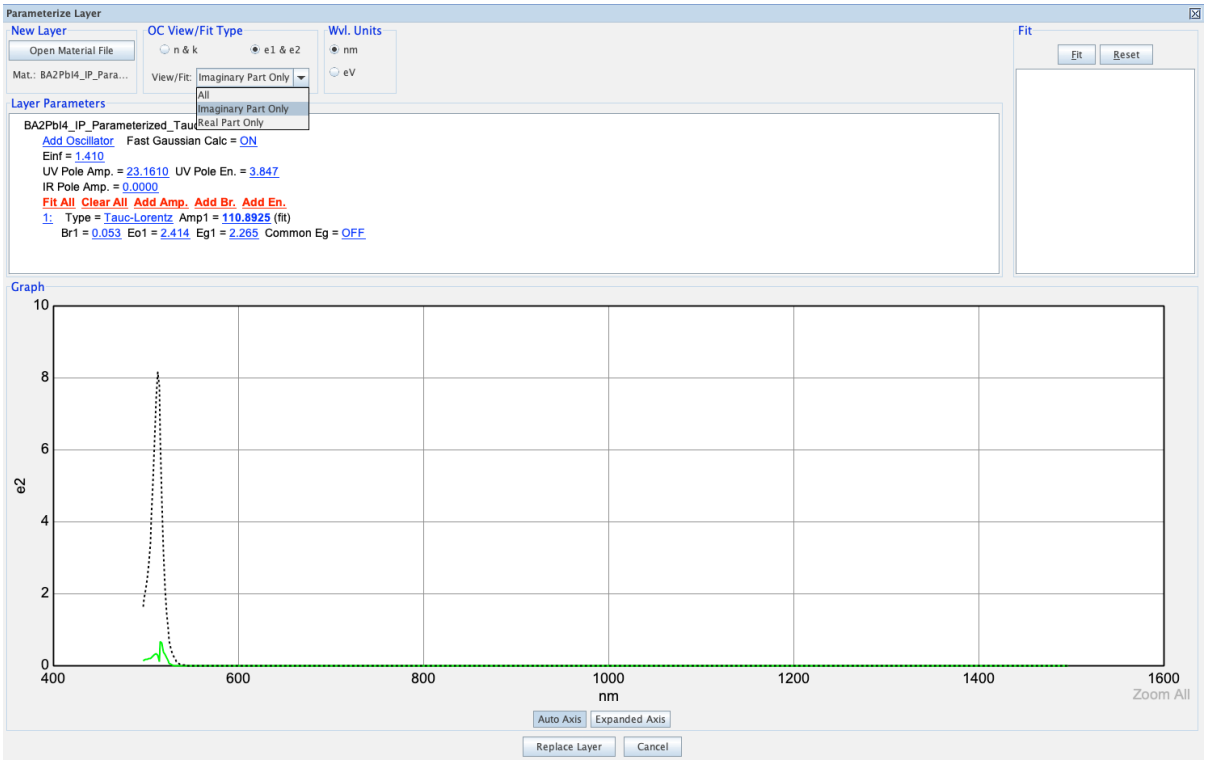
Parameterize Layer
New Layer
Open Material File
Mat.: BA2PbI4_IP_Para...
OC View/Fit Type
n & k
e1 & e2
View/Fit: Imaginary Part Only
All
Imaginary Part Only
Real Part Only
Wvl. Units
nm
eV
Fit
Fit
Reset
Layer Parameters
BA2PbI4_IP_Parameterized_Tauc
Add Oscillator Fast Gaussian Calc = ON
Einf = 1.410
UV Pole Amp. = 23.1610 UV Pole En. = 3.847
IR Pole Amp. = 0.0000
Fit All Clear All Add Amp. Add Br. Add En.
1: Type = Tauc-Lorentz Amp1 = 110.8925 (fit)
Br1 = 0.053 Eo1 = 2.414 Eg1 = 2.265 Common Eg = OFF
Graph
e2
nm
Zoom All
Auto Axis
Expanded Axis
Replace Layer
Cancel

Figure A.15:

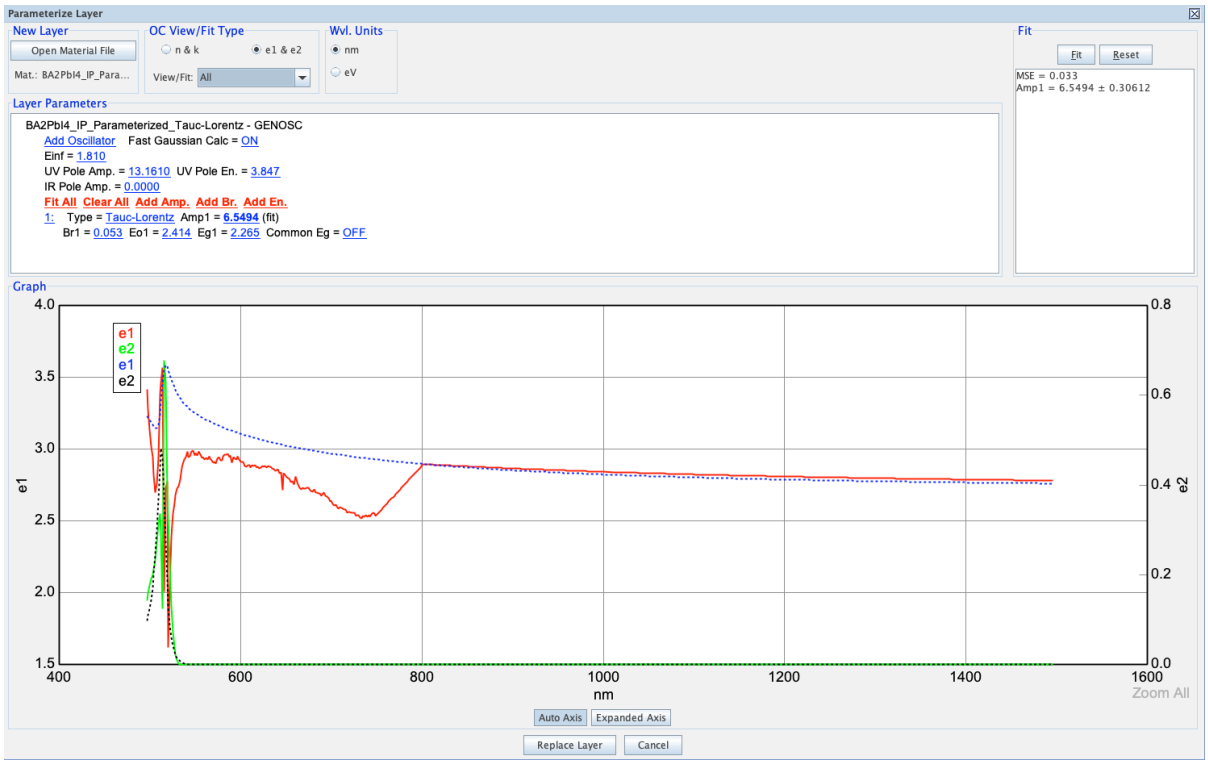
Parameterize Layer
New Layer
Open Material File
Mat.: BA2PbI4_IP_Para...
OC View/Fit Type
n & k
e1 & e2
View/Fit: All
Wvl. Units
nm
eV
Fit
Fit
Reset
MSE = 0.033
Amp1 = 6.5494 ± 0.30612
Layer Parameters
BA2PbI4_IP_Parameterized_Tauc-Lorentz - GENOSC
Add Oscillator Fast Gaussian Calc = ON
Einf = 1.810
UV Pole Amp. = 13.1610 UV Pole En. = 3.847
IR Pole Amp. = 0.0000
Fit All Clear All Add Amp. Add Br. Add En.
1: Type = Tauc-Lorentz Amp1 = 6.5494 (fit)
Br1 = 0.053 Eo1 = 2.414 Eg1 = 2.265 Common Eg = OFF
Graph
e1
e2
e1
e2
4.0
3.5
3.0
2.5
2.0
1.5
e1
0.8
0.6
0.4
0.2
0.0
e2
400
600
800
1000
1200
1400
1600
nm
Zoom All
Auto Axis
Expanded Axis
Replace Layer
Cancel

Figure A.16:

Sure, often the SE quantities in the complicated regions around optical resonances will *not* be perfectly well represented by this model. You can try to "correct" this ultimately by fitting other parameters *as needed* to the entire SE dataset. Do be aware that things go crazy with too many fit parameters. To this end, a brutal number of parameter couplings between the roughness layer and film layer must be defined. Sometimes the resulting fits are reasonable and lead to only small deviations from the previously determined model values; often I find this can be unfruitful and even dangerous. While Delta and Psi often *look* better after including new parameters, upon closer inspection you'll find crazy model parameter values and spurious optical constants. Have fun, but be safe. Intuitive understanding comes with much experimentation and trial and error. The technique does have its strengths, as I believe are demonstrated in ref. [17].

Appendix B

Reflectance functions for uniaxial thin-film systems

The single-interface polarized reflection coefficients between neighboring media i and j are derived by applying Maxwell's matching conditions at the interface, assuming incident, reflected, and transmitted waves. They take the following form [99]:

$$s\text{-polarized:} \quad r_{ij}^{s} = \frac{k_{zi} - k_{zj}}{k_{zi} + k_{zj}} \tag{B.1}$$

$$p\text{-polarized:} \quad r_{ij}^{p} = \frac{\epsilon_{ix} k_{zj} - \epsilon_{jx} k_{zi}}{\epsilon_{ix} k_{zj} + \epsilon_{jx} k_{zi}} \tag{B.2}$$

Here, k_{zi} is the z-component of the wave vector in medium i which, in the case of an anisotropic medium, also depends upon the polarization. These can be derived by Fourier transforming the fields appearing in the inhomogenous wave equation and solving the resulting algebraic eigenvalue problem relating the components of the wave vector $\vec{k} = k_x \hat{x} + k_z \hat{z}$ in terms of the frequency ω. In the case of a uniaxial medium (with z oriented along the optic axis), these take the following simple forms:

$$s\text{-polarized:} \quad k_{zi}^{(s)} = \sqrt{\epsilon_{ix} k_0^2 - k_x^2} \tag{B.3}$$

$$p\text{-polarized:} \quad k_{zi}^{(p)} = \sqrt{\epsilon_{ix} k_0^2 - \frac{\epsilon_{ix}}{\epsilon_{iz}} k_x^2}, \tag{B.4}$$

Here, k_0 is the free-space wave number $k_0 = 2\pi/\lambda$ (with free-space wavelength λ) and $\epsilon_{ix(z)}$ is the ordinary (extraordinary) component of the electric permittivity of medium i. The total wave number in medium i is given by $k_i = \sqrt{k_x^2 + k_z^2}$. The in-plane wave number, k_x, is always taken to be the conserved quantity in the planar stratified system.

The generic reflection coefficient from an n-layered stratified system can be determined from well-established transfer-matrix methods. The total polarized reflection coefficient for the common three-layer (two-interface) system is given specifically by:

$$r_{\text{3-layer}}^{s,p} = \frac{r_{12}^{s,p} + e^{2ihk_{z2}} r_{23}^{s,p}}{1 + e^{2ihk_{z2}} r_{12}^{s,p} r_{23}^{s,p}} \tag{B.5}$$

where h is the thickness of the central layer (e.g., thin film). The k_{zi} are implicitly polarization dependent according to the expressions above.

Appendix C

Effective-medium model expressions

C.1 Derivation of relevant expressions

Here we develop the effective medium model appropriate for a thin film system composed of layered crystallites with mixed orientation. In the manuscript, our effective medium derivation focused upon isotropic material constituents for simplicity. Here, we provide the generalized treatment for the case of *intrinsically* uniaxial constituents and films composed of crystallites with mixed orientation. For related treatments, see refs. [117, 173].

Let the plane z'=0 define a sharp interface between two distinct uniaxial dielectric media, 'medium 1' and 'medium 2' (Fig. C.1a). Let medium 1 exist in the region $z' < 0$ and medium 2 exist in the region $z' > 0$. Maxwell's equations applied at this interface provide a set of expressions relating the (complex) amplitudes of the electric field (E-field) at two positions infinitesimally close to, but on opposite sides of, the interface. Call these positions z'=0^- and z'=0^+. In this coordinate system, the optical response of *each* uniaxial medium can be described by a dielectric tensor with distinct elements in the

perpendicular-to-interface ($\perp$) and parallel-to-interface ($||$) directions:

$$\epsilon_1 = \mathrm{diag}(\epsilon_{1,||}, \epsilon_{1,||}, \epsilon_{1,\perp}) \tag{C.1}$$

$$\epsilon_2 = \mathrm{diag}(\epsilon_{2,||}, \epsilon_{2,||}, \epsilon_{2,\perp}) \tag{C.2}$$

For *isotropic* media, $\epsilon_{i,||}$=$\epsilon_{i,||}$, and the above tensors are described equally well as scalar values. Here we work the more general case of uniaxial constituent media, with which the permittivities are given by the tensors in Eqns. C.1-C.2. The permittivities of the constituent layers (Eqns. C.1-C.2) will be referred to as the "intrinsic" permittivites. In general, the elements in the above tensors depend on the frequency (ω=$2\pi c/\lambda$) of the electromagnetic field, and are thus complex.

The $||$ and $\perp$ matching conditions are distinct; $E_{||}$ is continuous immediately across the interface,

$$E_{||}(z' = 0^-) = E_{||}(z' = 0^+), \tag{C.3}$$

while $E_\perp$, witnesses a sharp discontinuity depending on the dielectric contrast,

$$\epsilon_{1,\perp} E_\perp(z' = 0^-) = \epsilon_{2,\perp} E_\perp(z' = 0^+). \tag{C.4}$$

By the constitutive relation, $\mathbf{D}$=$\epsilon\mathbf{E}$, Eqn. C.4 is equivalent to continuity of $D_\perp$:

$$D_{\perp}(z = 0^{-}) = D_{\perp}(z = 0^{+}) \tag{C.5}$$

For a system comprised of alternating layers of medium 1 and medium 2, each with a thickness that is deeply subwavelength, as in layered perovskite crystallites (Fig. C.1b), we can algebraically define average fields, $\overline{\mathbf{E}}$ and $\overline{\mathbf{D}}$, in each 'unit cell' comprised of a single medium 1 and a single medium 2 layer. Let the thickness of medium 1 (medium 2) be t_1 (t_2). Volumetric fill fractions of medium 1 (medium 2) can be defined as $f_{1(2)}{=}t_{1(2)}/(t_1 + t_2)$. Because the phase variation of the electric field due to propagation is negligible over the length scale of the unit cell ($t_1{+}t_2{\ll}\lambda$), the average fields can be easily determined from Eqns. C.3-C.5. By Eqn. C.3:

$$\overline{E}_{||} = \frac{1}{t_1 + t_2} \int_{-t_1}^{t_2} E_{||}(z)dz \approx E_{||}(0) \equiv E_{||} \tag{C.6}$$

By Eqn. C.3 and $\mathbf{D}{=}\epsilon\mathbf{E}$:

$$\begin{aligned}
\overline{D}_{||} &= \frac{1}{t_1 + t_2} \int_{-t_1}^{t_2} D_{||}(z)dz \\
&= \frac{1}{t_1 + t_2} \left[\int_{-t_1}^{0} \epsilon_{1,||} E_{||}(z)dz + \int_{0}^{t_2} \epsilon_{2,||} E_{||}(z)dz \right] \\
&\approx \frac{1}{t_1 + t_2} \left[t_1 \epsilon_{1,||} E_{||}(0) + t_2 \epsilon_{2,||} E_{||}(0) \right] \\
&\equiv (f_1 \epsilon_{1,||} + f_2 \epsilon_{2,||}) E_{||}
\end{aligned} \tag{C.7}$$

Relating Eqns. C.6 and C.7 *via* a constitutive relation, and using $f_2{=}1 - f_1$, gives a

definition for the average, or "effective", || dielectric constant, $\overline{\epsilon}_{||}$:

$$\overline{\epsilon}_{||} \equiv \overline{D}_{||}/\overline{E}_{||} = f_1\epsilon_{1,||} + (1-f_1)\epsilon_{2,||} \tag{C.8}$$

The effective dielectric constant associated with the $\perp$ direction is derived analogously. By Eqn. C.5 and $\mathbf{D}$=$\epsilon\mathbf{E}$:

$$\begin{aligned}
\overline{E}_\perp &= \frac{1}{t_1+t_2}\int_{-t_1}^{t_2} E_\perp(z)dz \\
&= \frac{1}{t_1+t_2}\left[\int_{-t_1}^{0}\frac{D_\perp(z)}{\epsilon_{1,\perp}}dz + \int_0^{t_2}\frac{D_\perp(z)}{\epsilon_{2,\perp}}dz\right] \\
&\approx \frac{1}{t_1+t_2}\left[t_1\frac{D_\perp(0)}{\epsilon_{1,\perp}} + t_2\frac{D_\perp(0)}{\epsilon_{2,\perp}}\right] \\
&\equiv \left(\frac{f_1}{\epsilon_{1,\perp}} + \frac{f_2}{\epsilon_{2,\perp}}\right) D_\perp
\end{aligned} \tag{C.9}$$

By Eqn. C.5:

$$\overline{D}_\perp = \frac{1}{t_1+t_2}\int_{-t_1}^{t_2} D_\perp(z)dz \approx D_\perp(0) \equiv D_\perp \tag{C.10}$$

Relating Eqns. C.9 and C.10 *via* a constitutive relation, and using f_2=$1-f_1$, gives a definition for the effective $\perp$ dielectric constant, $\overline{\epsilon}_\perp$:

$$\overline{\epsilon}_\perp \equiv \overline{D}_\perp/\overline{E}_\perp = \frac{1}{f_1/\epsilon_{1,\perp} + (1-f_1)/\epsilon_{2,\perp}} \tag{C.11}$$

Each crystallite is thus associated with an effective permittivity tensor, $\overline{\epsilon}$=diag$(\overline{\epsilon}_{||}, \overline{\epsilon}_{||}, \overline{\epsilon}_\perp)$,

defined in relation to a local set of coordinates "fixed" to the crystallite. Spin-cast thin films of $(C_4)_2(C_1)_{N-1}Pb_NI_{3N+1}$are comprised of a statistical mixture of oriented crystallites (Fig. C.1c), each of which is assumed to be described by Eqns. C.8 and C.11. For a thin film system with crystalline domains ($\sim$500 nm) on the order of the wavelength of the light (*i.e.*, much larger than the characteristic layer thicknesses, $t\sim$1 nm), the optical response of the thin film is well described as a volumetric average of the oriented crystallites. Let the z-axis define the direction perpendicular to the plane of the substrate interface. If we let η_z represent the volume fraction of the film composed of crystallites with $z'||z$, the elements of the dielectric tensor describing the thin film optical response are given by

$$\overline{\epsilon}_x = \frac{1}{2}(1-\eta_z)\overline{\epsilon}_\perp + \frac{1}{2}(1-\eta_z)\overline{\epsilon}_{||} + \eta_z\overline{\epsilon}_{||} \tag{C.12}$$

$$\overline{\epsilon}_y = \frac{1}{2}(1-\eta_z)\overline{\epsilon}_{||} + \frac{1}{2}(1-\eta_z)\overline{\epsilon}_\perp + \eta_z\overline{\epsilon}_{||} \tag{C.13}$$

$$\overline{\epsilon}_z = (1-\eta_z)\overline{\epsilon}_{||} + \eta_z\overline{\epsilon}_\perp \tag{C.14}$$

Note that when η_z=1, as in the case of R_2PbI_4, $\overline{\epsilon}_{||}$=$\overline{\epsilon}_x$=$\overline{\epsilon}_y$ and $\overline{\epsilon}_\perp$=$\overline{\epsilon}_z$. The value $\eta_z\approx1/3$ represents the limit at which the effective medium is optically isotropic. The complex ordinary (in-plane) ($\tilde{n}_o$) and extraordinary (out-of-plane) ($\tilde{n}_e$) refractive index of the thin

film is given by:

$$\tilde{n}_{\mathrm{o}} = \sqrt{\overline{\epsilon}_x} = \sqrt{\overline{\epsilon}_y} \tag{C.15}$$

$$\tilde{n}_{\mathrm{e}} = \sqrt{\overline{\epsilon}_z} \tag{C.16}$$

Definitions C.12-C.16 assume rotational symmetry of the thin-film about the z-axis (in-plane isotropy), η_x=η_y=$(1-\eta_z)/2$, and is well-justified for spin-cast thin films. Consequently, $\overline{\epsilon}_x$ and $\overline{\epsilon}_y$ take identical values. Eqns. C.8, C.11-C.16 are the essential expressions relating the *effective* medium optical response ($\overline{\epsilon}_{x,y}$, $\overline{\epsilon}_z$ and $\tilde{n}_{\mathrm{o}}$, $\tilde{n}_{\mathrm{e}}$; those measured directly in experiment) (Fig. C.1d) to the *intrinsic* optical response of the constituent layers ($\epsilon_{1,||}$, $\epsilon_{1,\perp}$, $\epsilon_{2,||}$, $\epsilon_{2,\perp}$) for a given morphology (f_1, η_z). We note that these produce results very similar to, if not identical to, the results from ref. [173] in the limit when the volume fraction of inclusions $f \to \infty$ (*i.e.*, when there is no "host" material). To obtain the results presented in Fig. 4.7, we solve, at each wavelength, the equations

$$\overline{\epsilon}_x(\lambda) = \overline{\epsilon}_y(\lambda) = \overline{\epsilon}_x(\lambda)^{\mathrm{measured}}(\lambda) = \overline{\epsilon}_y(\lambda)^{\mathrm{measured}}(\lambda) \tag{C.17}$$

$$\overline{\epsilon}_z(\lambda) = \overline{\epsilon}_z^{\mathrm{measured}}(\lambda) \tag{C.18}$$

for the *intrinsic* permittivities of the lead iodide layers.

We note that the relationship for the OP components is particularly sensitive to input parameters (*e.g.*, f_{PbI}, $\epsilon_{2,\perp}$; see Eqn. C.11). We assume isotropic organic refractive index values from ref. [103, 104]. Considering the average OP orientation of the organic cations, the IP permittivity of these layers is likely slightly smaller (by ≈0.1-0.2) than that assumed for our calculations. Consequently, the resulting *intrinsic*

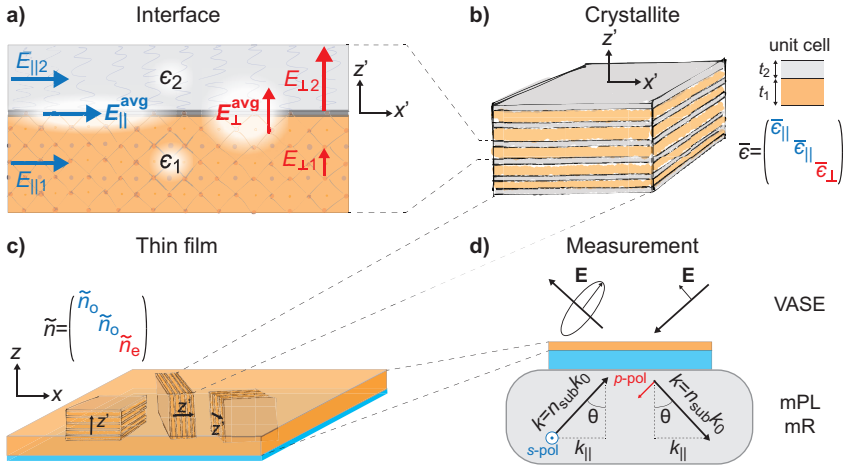

Figure C.1: ***Schematic of effective medium theory for spin-cast thin films of $(C_4)_2(C_1)_{N-1}Pb_NI_{3N+1}$.*** **(a)** Electric field matching conditions at the level of a single interface. **(b)** A layered crystal adopts a uniaxial permittivity tensor due to nano-scale dielectric inhomogeneity. This permittivity tensor is defined with respect to a local set of coordinates "fixed" to the crystallite. **(c)** Spin-cast thin films are composed of a statistical mixture of oriented crystallites. **(d)** Conventional optical measurements probe only the macroscopic, orientation-averaged optical response.

IP oscillator strength is likely slightly underestimated. Using Eqns. C.8 we estimate that such errors amount to $\approx 4\%$. The resulting *intrinsic* OP:IP ratio is thus likely somewhat overestimated. The relationship between $\bar{\epsilon}_\perp$, $\epsilon_{1,2}$, and the other input system parameters is more sensitive, and thus errors in the OP permittivity are more significant. Nonetheless, these considerations tell us that the $\perp$ component is *always* significantly underestimated in cases in which the barrier layer has a relatively low permittivity.

C.2 Model parameters used for EMM calculations

The EMM expressions derived in the previous section relate the *effective* (measured) optical constants ($\tilde{n}_o$, $\tilde{n}_e$) to the intrinsic optical constants (ϵ_1, ϵ_2), with two additional parameters describing the internal structure the system: the volumetric fill fraction of

lead iodide layers, f_{PbI}, and the volume fraction of z-oriented crystallites, η_z. Values for f_{PbI} were taken from our X-ray diffraction data (see Methods in manuscript) and compared to previous published reports.[105, 82, 174, 83] η_z was taken from ref. [102]. Input parameters used in our calculations are summarized in Table S1:

N	1 (C_4)	1 (C_6)	1 (C_8)	1 (PEA)	2	3
f_{PbI}	0.462	0.391	0.341	0.390	0.64	0.73
η_z	1.0	1.0	1.0	1.0	0.76	0.25
n_{organic}	1.5	1.49	1.48	1.6	1.58	1.58

Table S1: Volumetric fill fractions of lead iodide layers (f_{PbI}) and volume fraction of z-oriented crystallites (η_z) in thin films of $(C_m)_2PbI_4$ (N=1, m=4, 6, and 8), PEA_2PbI_4, and $(C_4)_2(C_1)_{N-1}Pb_NI_{3N+1}$ (m=4, N=2,3).

The refractive index values of the organic spacer layers used in this study were assumed to be isotropic and wavelength-independent in the visible wavelength region of interest. We take values for n_{organic} inferred from ref. [104] with insight from a number of other reports [20, **?**, 79, 80, 103, 138] We allow slight variation in the organic refractive index to account for the approach to more bulk-like organic refractive index values as the length of the molecule increases, motivated by the results of ref. [104].

Appendix D

Radiation patterns for oriented electric and magnetic dipoles and electric quadrupoles

D.1 Calculating normalized intrinsic multipolar emission rates

In energy-momentum spectroscopy, the s- or p-polarized PL counts, $N^{s,p}(\omega, \mathbf{k}_{||})$, measured at a given frequency (ω=$2\pi c/\lambda$, where λ is the free-space wavelength) and a given (conserved) in-plane electromagnetic wave momentum, $\mathbf{k}_{||}$=$k_x\hat{x}$+$k_y\hat{y}$, is given by

$$N^{s,p}(\omega, \mathbf{k}_{||}) = C_{\exp}\Big[\Gamma^{s,p}_{ED_x}(\omega, \mathbf{k}_{||}) + \Gamma^{s,p}_{ED_y}(\omega, \mathbf{k}_{||}) + \Gamma^{s,p}_{ED_z}(\omega, \mathbf{k}_{||}) \tag{D.1}$$

$$+\Gamma^{s,p}_{MD_z}(\omega, \mathbf{k}_{||}) + \Gamma^{s,p}_{EQ_{xy}}(\omega, \mathbf{k}_{||}) + \Gamma^{s,p}_{EQ_{x'y'}}(\omega, \mathbf{k}_{||})\Big] \tag{D.2}$$

Here, the Γ_{M_o} correspond to the photon emission rates of a multipole, M (i.e., ED, MD, EQ), with an orientation (or "configuration", for EQs) o, positioned in the thin film (an inhomogeneous environment), and C_{exp} is a constant accounting for experimental collection efficiencies. As in the manuscript, we focus on in-plane (IP) and out-of-plane (OP) oriented EDs, OP-oriented MDs, and the two degenerate IP transverse EQs (EQ_{xy} and $\text{EQ}_{x'y'}$). According to refs [116, 99], the multipolar emission rates, $\Gamma^{s,p}_{M_o}(\omega, \mathbf{k}_{||})$, are related to the intrinsic emission rates, A_{M_o}, in a bulk (infinite) homogeneous medium of refractive index n by the normalized local density of optical states (LDOS), $\rho^{s,p}_{M_o}$, according to

$$\Gamma^{s,p}_{M_o}(\omega, \mathbf{k}_{||}) = A_{M_o}(\omega)\tilde{\rho}^{s,p}_{M_o}(\omega, \mathbf{k}_{||}) \tag{D.3}$$

giving

$$\begin{aligned} N^{s,p}(\omega,\mathbf{k}_{||}) = C_{\text{exp}} \Big[& A_{ED_x}(\omega)\tilde{\rho}^{s,p}_{ED_x}(\omega, \mathbf{k}_{||}) + A_{ED_y}(\omega)\tilde{\rho}^{s,p}_{ED_y}(\omega, \mathbf{k}_{||}) + A_{ED_z}(\omega)\tilde{\rho}^{s,p}_{ED_z}(\omega, \mathbf{k}_{||}) \\ & + A_{MD_z}(\omega)\tilde{\rho}^{s,p}_{MD_z}(\omega, \mathbf{k}_{||}) + A_{EQ_{xy}}(\omega)\tilde{\rho}^{s,p}_{EQ_{xy}}(\omega, \mathbf{k}_{||}) + A_{EQ_{x'y'}}(\omega)\tilde{\rho}^{s,p}_{EQ_{x'y'}}(\omega, \mathbf{k}_{||}) \Big] \end{aligned} \tag{D.4}$$

We allow the intrinsic multipolar emission rates, A_{M_o}, to vary with orientation since it is possible, in general, to have different oriented species [99]. However, we will assume A_{ED_x}=A_{ED_y} and $A_{EQ_{xy}}$=$A_{EQ_{x'y'}}$, as necessary for a rotationally invariant system. By absorption-emission reciprocity, the enhanced (or suppressed) emission rate into each mode can be determined by the enhanced (or suppressed) absorption rate for illumination by that mode:

$$\tilde{\rho}^{s,p}_{M_o,\text{emit}} \equiv \frac{\Gamma^{s,p}_{M_o}}{A_{M_o}} = \tilde{\rho}^{s,p}_{M_o,\text{absorb}} \equiv \frac{\alpha^{s,p}_{M_o}}{B_{M_o}} \tag{D.5}$$

in which we have defined two multipolar absorption rates analogous to the emission rates: $\alpha^{s,p}_{M_o}(\omega,\mathbf{k}_{||})$ is the absorption rate in the thin film when illuminated by an s- or p-polarized plane wave of frequency ω and IP wave vector $\mathbf{k}_{||}$; $B_{M_o}(\omega)$ is the total absorption rate in a homogeneous environment (i.e., integrated over all electromagnetic modes with wave vector k=$|\mathbf{k}|$=$n\omega/c$). Particularly,

$$\tilde{\rho}^{s,p}_{ED_i}(\omega,\mathbf{k}_{||}) = \frac{|\mu_{ED,i}E^{s,p}_i(\omega,\mathbf{k}_{||})|^2}{\sum_{s,p}\int d^2k|\mu_{ED,i}E^{s,p}_{0,i}(\omega,\mathbf{k}_{||})|^2} = \frac{|\tilde{E}^{s,p}_i(\omega,\mathbf{k}_{||})|^2}{\sum_{s,p}\int d^2k|\hat{e}^{s,p}_i(\mathbf{k}_{||})|^2} \tag{D.6}$$

$$\tilde{\rho}^{s,p}_{MD_i}(\omega,\mathbf{k}_{||}) = \frac{|\mu_{MD,i}\tilde{B}^{s,p}_i(\omega,\mathbf{k}_{||})|^2}{\sum_{s,p}\int d^2k|\mu_{MD,i}B^{s,p}_{0,i}(\omega,\mathbf{k}_{||})|^2} = \frac{|\tilde{B}^{s,p}_i(\omega,\mathbf{k}_{||})|^2}{\sum_{s,p}\int d^2k|\hat{b}^{s,p}_i(\mathbf{k}_{||})|^2} \tag{D.7}$$

$$\tilde{\rho}^{s,p}_{EQ_{xy}}(\omega,\mathbf{k}_{||}) = \frac{|Q_{xy}\partial_x E^{s,p}_y(\omega,\mathbf{k}_{||}) + Q_{yx}\partial_y E^{s,p}_x(\omega,\mathbf{k}_{||})|^2}{\sum_{s,p}\int d^2k|Q_{xy}\partial_x E^{s,p}_{y,0}(\omega,\mathbf{k}_{||}) + Q_{yx}\partial_y E^{x,p}_{x,0}(\omega,\mathbf{k}_{||})|^2} \tag{D.8}$$

$$= \frac{|\partial_x \tilde{E}^{s,p}_y(\omega,\mathbf{k}_{||}) + \partial_y E^{s,p}_x(\omega,\mathbf{k}_{||})|^2}{\sum_{s,p}\int d^2k|\partial_x \hat{e}^{s,p}_y(\mathbf{k}_{||}) + \partial_y \hat{e}^{x,p}_x(\mathbf{k}_{||})|^2} \tag{D.9}$$

Here, $\tilde{E}^{s,p}_i$=$E^{s,p}_i/E_0$ ($\tilde{B}^s_z$=B^s_z/B_0) is the electric (magnetic) field amplitude, projected along the $\hat{i}$ direction, at the position of the emitter, normalized by the field amplitude, E_0 (B_0), of the incident wave. The fields $\hat{e}^{s,p}_i$ and $\hat{b}^{s,p}_i$ are the frequency-independent unit-amplitude electric and magnetic field vectors projected along the Cartesian $\hat{i}$ direction ($\hat{x}_i$): $\hat{e}^{s,p}_i$=$(\hat{x}_i \cdot \vec{E}^{s,p}_0)/E_0$. The EQ coefficients cancel because Q_{yx}=Q_{xy}. Notice that s-polarized radiation from ED emitters ($\Gamma^s_{ED,i}$) is uniquely determined by up to a constant scale factor since only IP EDs contribute to this emission, i.e., $\tilde{\rho}^s_{ED,z}$=0.

D.1.1 ED LDOS Denominators

The numerators for the ED LDOS are readily available in the literature [99] and can be expressed by matrix methods [121]. We evaluate the denominators for the three unique

dipole orientations using cylindrical coordinates in the variable $\mathbf{k}_{||}$ ($|\mathbf{k}_{||}|{=}k_{||}$). In projecting the spherical integration surface (radius $k{=}|\mathbf{k}|{=}n\omega/c$) to the circular integration surface over the variable $\mathbf{k}_{||}$ ($0{\leq}|\mathbf{k}_{||}|{\leq}k$), we must include a factor of $1/\cos\theta{=}k/(k^2-k_{||}^2)^{1/2}$ in the integrand to ensure that all waves carry equivalent power in $\hat{z}$:

$$i=x: \quad 2\iint \frac{k_{||}dk_{||}d\phi}{\cos\theta}(|\hat{e}_x^s(\mathbf{k}_{||})|^2+|\hat{e}_x^p(\mathbf{k}_{||})|^2) = 2\iint \frac{k_{||}dk_{||}d\phi}{\cos\theta}(\sin^2\phi+\cos^2\theta\cos^2\phi) = \frac{8\pi k^2}{3} \tag{D.10}$$

$$i=y: \quad 2\iint \frac{k_{||}dk_{||}d\phi}{\cos\theta}(|\hat{e}_y^s(\mathbf{k}_{||})|^2+|\hat{e}_y^p(\mathbf{k}_{||})|^2) = 2\iint \frac{k_{||}dk_{||}d\phi}{\cos\theta}(\cos^2\phi+\cos^2\theta\sin^2\phi) = \frac{8\pi k^2}{3} \tag{D.11}$$

$$i=z: \quad 2\iint \frac{k_{||}dk_{||}d\phi}{\cos\theta}(|\hat{e}_z^s(\mathbf{k}_{||})|^2+|\hat{e}_z^p(\mathbf{k}_{||})|^2) = 2\iint \frac{k_{||}dk_{||}d\phi}{\cos\theta}(0+\sin^2\theta) = \frac{8\pi k^2}{3} \tag{D.12}$$

where $\cos\phi{=}k_x/k_{||}$ ($0{<}\phi{<}2\pi$), and the factor of 2 is included for integration over $0{<}\theta{<}\pi/2$ to account for the full 4π steradians. Equality of the three integrals is expected on the grounds that the reference space is isotropic. Identical results are obtained by performing integration over spherical coordinates (θ,ϕ) and eliminating the factor of $1/\cos\theta$ from the integrand.

D.1.2 MD LDOS

The quantities $|\tilde{B}_i^{s,p}|^2$ in the slab (thin film) can be calculated analytically [116]. Here we use S-Matrix methods to directly relate these terms to $|\tilde{E}_i^{s,p}|^2$. Note that, for a plane wave propagating with a wave vector $\mathbf{k}$, the electric and magnetic fields are related by

$\mathbf{k} \times \mathbf{E}=\omega\mathbf{B}$. Component by component,

$$B_x = \frac{1}{\omega}\left(k_y E_z - k_z E_y\right) \tag{D.13}$$

$$B_y = \frac{1}{\omega}\left(-k_x E_z + k_z E_x\right) \tag{D.14}$$

$$B_z = \frac{1}{\omega}\left(k_x E_y - k_y E_x\right) \tag{D.15}$$

$$\tag{D.16}$$

To express the fields corresponding to s- and p-polarized plane waves, take $\mathbf{k}_{||}=k_x\hat{x}=k_{||}\hat{x}$. With this geometry, $\mathbf{E}^s=E_y\hat{y}$ ($\mathbf{B}^s=B_x\hat{x}+B_z\hat{z}$) and $\mathbf{E}^p=E_x\hat{x}+E_z\hat{z}$ ($\mathbf{B}^p=B_y\hat{y}$). In the slab (thin film), the total field is comprised of both '+' (upward propagating) and '-' (downward propagating) components. The law of reflection gives $(k_z^{s,p})^-=-(k_z^{s,p})^+\equiv -k_z^{s,p}$.

$$p\text{-pol.}: \quad B_x^p = B_z^p = 0 \tag{D.17}$$

$$\begin{aligned} B_y^p &= (B_y^p)^+ + (B_y^p)^- \\ &= \frac{1}{\omega}\{[-k_x(E_z^p)^+ + k_z^p(E_x^p)^+] + [-k_x(E_z^p)^- + (k_z^p)^-(E_x^p)^-]\} \\ &= -\frac{1}{\omega}\{k_x[(E_z^p)^+ + (E_z^p)^-] - k_z^p[(E_x^p)^+ - (E_x^p)^-]\} \\ &= -\frac{1}{\omega}\{k_x E_z^p - k_z^p[(E_x^p)^+ - (E_x^p)^-]\} \\ &= -\frac{1}{\omega}\{k_{||} E_z^p - k_z^p[(E_{||}^p)^+ - (E_{||}^p)^-]\} \end{aligned} \tag{D.18}$$

$$B_z^p = 0 \tag{D.19}$$

$$\tag{D.20}$$

$$
\begin{aligned}
s\text{-pol.}: \quad B_x^s &= (B_x^s)^+ + (B_x^s)^- \\
&= \frac{1}{\omega}[-(k_z^s)^+(E_y^s)^+ - (k_z^s)^-(E_y^s)^-] \\
&= -\frac{1}{\omega}k_z^s[(E_y^s)^+ - (E_y^s)^-] \\
&= -\frac{1}{\omega}k_z^s[(E_{||}^s)^+ - (E_{||}^s)^-] \qquad \text{(D.21)} \\
B_y^s &= 0 \qquad \text{(D.22)} \\
B_z^s &= (B_z^s)^+ + (B_z^s)^- \\
&= \frac{1}{\omega}[k_{||}(E_{||}^s)^+ + k_{||}(E_{||}^s)^-] \qquad \text{(D.23)} \\
&= \frac{1}{\omega}k_{||}E_{||}^s
\end{aligned}
$$

where we have defined $E_{||}^s$=E_y^s and $E_{||}^p$=E_x^p as in in-plane component of the s- and p-polarized fields for the illumination configuration with $\mathbf{k}_{||}$=$k_{||}\hat{x}$ as a matter of convenience. Evaluating the normalized field magnitude squared (numerators in Eqn. D.7) with the relation B_0=$(k/\omega)E_0$ for each Cartesian component,

$$
\begin{aligned}
|\tilde{B}_{x,z}^p|^2 &= 0 \qquad \text{(D.24)} \\
|\tilde{B}_y^p|^2 &= \frac{1}{k^2}\left|k_{||}\tilde{E}_z^p - k_z^p[(\tilde{E}_{||}^p)^+ - (\tilde{E}_{||}^p)^-]\right|^2 \qquad \text{(D.25)} \\
|\tilde{B}_x^s|^2 &= \frac{|k_z^s|^2}{k^2}\left|(\tilde{E}_{||}^s)^+ - (\tilde{E}_{||}^s)^-\right|^2 \qquad \text{(D.26)} \\
|\tilde{B}_y^s|^2 &= 0 \qquad \text{(D.27)} \\
|\tilde{B}_z^s|^2 &= \frac{k_{||}^2}{k^2}|\tilde{E}_{||}^s|^2 \qquad \text{(D.28)}
\end{aligned}
$$

The denominators of Eqn. D.7 are simply related to the denominators of Eqn. D.6

by acknowledging the following relations:

$$\hat{b}_x^p(\mathbf{k}_{||}) = \hat{e}_x^s(\mathbf{k}_{||}) \quad \hat{b}_x^s(\mathbf{k}_{||}) = -\hat{e}_x^p(\mathbf{k}_{||}) \tag{D.29}$$

$$\hat{b}_y^p(\mathbf{k}_{||}) = \hat{e}_y^s(\mathbf{k}_{||}) \quad \hat{b}_y^s(\mathbf{k}_{||}) = -\hat{e}_y^p(\mathbf{k}_{||}) \tag{D.30}$$

$$\hat{b}_z^p(\mathbf{k}_{||}) = \hat{e}_z^s(\mathbf{k}_{||}) = 0 \quad \hat{b}_z^s(\mathbf{k}_{||}) = -\hat{e}_z^p(\mathbf{k}_{||}) \tag{D.31}$$

Therefore, the denominators of Eqn. D.7 evaluate to the same values as those of Eqn. D.6:

$$\sum_{s,p} \int d^2k |\hat{b}_i^{s,p}(\mathbf{k}_{||})|^2 = \frac{8\pi k^2}{3} \quad \text{for all } i \tag{D.32}$$

which is again just the statement that MDs of all orientations in a homogenous and isotropic environment emit at equal rates.

D.1.3 EQ LDOS

Of interest here are the two distinct EQ terms (EQ_{xy} and $\mathrm{EQ}_{x'y'}$). The denominators are equivalent in both cases due to the azimuthal symmetry of the reference system:

$$\begin{aligned}
B_{EQ_{xy}} &= 2\iint \frac{k_{||}dk_{||}d\phi}{\cos\theta}(|\partial_x\hat{e}_y^s(\mathbf{k}_{||}) + \partial_y\hat{e}_x^s(\mathbf{k}_{||})|^2 + |\partial_x\hat{e}_y^p(\mathbf{k}_{||}) + \partial_y\hat{e}_x^p(\mathbf{k}_{||})|^2) \\
&= 2\iint \frac{k_{||}dk_{||}d\phi}{\cos\theta}(|ik_x\hat{e}_y^s(\mathbf{k}_{||}) + ik_y\hat{e}_x^s(\mathbf{k}_{||})|^2 + |ik_x\hat{e}_y^p(\mathbf{k}_{||}) + ik_y\hat{e}_x^p(\mathbf{k}_{||})|^2) \\
&= 2\iint \frac{k_{||}dk_{||}d\phi}{\cos\theta}k_{||}^2(|\cos\phi\hat{e}_y^s(\mathbf{k}_{||}) + \sin\phi\hat{e}_x^s(\mathbf{k}_{||})|^2 + |\cos\phi\hat{e}_y^p(\mathbf{k}_{||}) + \sin\phi\hat{e}_x^p(\mathbf{k}_{||})|^2) \\
&= 2\iint \frac{k_{||}^3dk_{||}d\phi}{\cos\theta}(|-\cos^2\phi + \sin^2\phi|^2 + |-\cos\phi\cos\theta\sin\phi - \sin\phi\cos\theta\cos\phi|^2) \\
&= \frac{4\pi k^4}{3}
\end{aligned} \tag{D.33}$$

where we have again evaluated the integral in cylindrical coordinates with the same angle conventions as in the previous section. Other EQ configurations can be analyzed analogously.

For EQ_{xy}, we work out the numerator with $\mathbf{k}_{||}=k_{||}\hat{x}$, noting that the only x dependence in the problem is contained in the phase factor $\exp(ik_{||}x)$:

$$|\partial_x\tilde{E}_y^s(\omega,k_{||})|^2 = |ik_{||}\tilde{E}_y^s(\omega,k_{||})|^2 = k_{||}^2|\tilde{E}_y^s(\omega,k_{||})|^2 \tag{D.34}$$

For $\mathrm{EQ}_{x'y'}$, which is equivalent to EQ_{xy} rotated by $\pi/4$ radians in-plane, we consider again $\mathbf{k}_{||}=k_{||}\hat{x}$ and define rotated coordinates $x'=(x+y)/\sqrt{2}$ and $y'=(x-y)/\sqrt{2}$ which

are "square" with $\mathrm{EQ}_{x'y'}$ and write the driving term:

$$\begin{aligned}
&|\partial_{x'}\tilde{E}^p_{y'}(\omega,k_{||})+\partial_{y'}\tilde{E}^p_{x'}(\omega,k_{||})|^2 \\
&\qquad=\left|(\frac{1}{\sqrt{2}}\partial_x+\frac{1}{\sqrt{2}}\partial_y)\tilde{E}^p_{y'}(\omega,k_{||})+(-\frac{1}{\sqrt{2}}\partial_y+\frac{1}{\sqrt{2}}\partial_x)\tilde{E}^p_{x'}(\omega,k_{||})\right|^2 \\
&\qquad=\frac{k_{||}^2}{2}|\tilde{E}^p_{y'}(\omega,k_{||})+\tilde{E}^p_{x'}(\omega,k_{||})|^2 \\
&\qquad=\frac{k_{||}^2}{2}\left|\frac{2}{\sqrt{2}}\tilde{E}^p_{x}(\omega,k_{||})\right|^2 \\
&\qquad=k_{||}^2|\tilde{E}^p_{x}(\omega,k_{||})|^2
\end{aligned} \tag{D.35}$$

(Note that this calculation is equivalent to considering EQ_{xy} with an incident wave propagating with $\mathbf{k}_{||}=k_{||}(\hat{x}+\hat{y})/\sqrt{2}$.) Finally,

$$\tilde{\rho}^s_{EQ_{xy}}(\omega,k_{||})=\frac{3}{4\pi k^4}k_{||}^2|\tilde{E}^s_{||}(\omega,k_{||})|^2 \tag{D.36}$$

$$\tilde{\rho}^p_{EQ_{x'y'}}(\omega,k_{||})=\frac{3}{4\pi k^4}k_{||}^2|\tilde{E}^p_{||}(\omega,k_{||})|^2 \tag{D.37}$$

where we have defined $\tilde{E}^s_{||}\equiv\tilde{E}^s_y$ and $\tilde{E}^p_{||}\equiv\tilde{E}^p_x$ as the in-plane component of the s- and p-polarized fields for the illumination configuration with $\mathbf{k}_{||}=k_{||}\hat{x}$ as a matter of convenience. Note that $\tilde{\rho}^s_{EQ_{xy}}$ is functionally equivalent to $\tilde{\rho}^s_{MD_z}$.

D.1.4 Producing x- and y-polarized BFP images

With the above expressions, x- and y-polarized 2D BFP radiation profiles for any emitting species (e.g., ED, MD, EQ) are produced by projecting the s- and p-polarized expressions onto a Cartesian basis. Explicitly:

$$x\text{-pol.:} \quad \rho^x(k_x, k_y) = \sin^2\phi \ \rho^s(k_{||}) + \cos^2\phi \ \rho^p(k_{||}) \tag{D.38}$$

$$= \frac{k_y^2}{k_x^2 + k_y^2}\rho^s\left(\sqrt{k_x^2 + k_y^2}\right) + \frac{k_x^2}{k_x^2 + k_y^2} \ \rho^p\left(\sqrt{k_x^2 + k_y^2}\right) \tag{D.39}$$

$$y\text{-pol.:} \quad \rho^y(k_x, k_y) = \cos^2\phi \ \rho^s(k_{||}) + \sin^2\phi \ \rho^p(k_{||}) \tag{D.40}$$

$$= \frac{k_x^2}{k_x^2 + k_y^2}\rho^s\left(\sqrt{k_x^2 + k_y^2}\right) + \frac{k_y^2}{k_x^2 + k_y^2}\rho^p\left(\sqrt{k_x^2 + k_y^2}\right) \tag{D.41}$$

Bibliography

[1] M. Pope and C. Swenberg, *Electronic Processes in Organic Crystals and Polymers*. Monographs on the physics and chemistry of materials. Oxford University Press, 1999.

[2] O. Ostroverkhova, *Organic Optoelectronic Materials: Mechanisms and Applications*, *Chemical Reviews* **116** (Nov., 2016) 13279–13412.

[3] Y. Diao, L. Shaw, Z. Bao, and S. C. B. Mannsfeld, *Morphology control strategies for solution-processed organic semiconductor thin films*, *Energy Environ. Sci.* **7** (2014), no. 7 2145–2159.

[4] LG Corporation, *LG Electronics: OLED TVs*, *Online* (2020). Accessed 2020-02-25. `https://www.lg.com/us/oled-tvs`.

[5] H. Wang, Y. Xu, X. Yu, R. Xing, J. Liu, and Y. Han, *Structure and Morphology Control in Thin Films of Conjugated Polymers for an Improved Charge Transport*, *Polymers* **5** (Nov., 2013) 1272–1324.

[6] C. Liao, M. Zhang, M. Y. Yao, T. Hua, L. Li, and F. Yan, *Flexible Organic Electronics in Biology: Materials and Devices*, *Advanced Materials* **27** (Dec., 2015) 7493–7527.

[7] M. Campoy-Quiles, P. G. Etchegoin, and D. D. C. Bradley, *On the optical anisotropy of conjugated polymer thin films*, *Phys. Rev. B* **72** (July, 2005) 045209.

[8] S. Das, J. A. Robinson, M. Dubey, H. Terrones, and M. Terrones, *Beyond Graphene: Progress in Novel Two-Dimensional Materials and van der Waals Solids*, *Annual Review of Materials Research* **45** (July, 2015) 1–27.

[9] S. J. Brown, *Morphology-dependent optical anisotropies in organic semiconductors*, *Ph. D. thesis* (2017). ProQuest ID: Brown_ucsb_0035D_13420. Merritt ID: ark:/13030/m5rv5mm7. Retrieved from `https://escholarship.org/uc/item/3f05q931`.

[10] J. Rivnay, R. Steyrleuthner, L. H. Jimison, A. Casadei, Z. Chen, M. F. Toney, A. Facchetti, D. Neher, and A. Salleo, *Drastic Control of Texture in a High*

Performance n-Type Polymeric Semiconductor and Implications for Charge Transport, *Macromolecules* **44** (July, 2011) 5246–5255.

[11] C. J. Takacs, N. D. Treat, S. Krmer, Z. Chen, A. Facchetti, M. L. Chabinyc, and A. J. Heeger, *Remarkable Order of a High-Performance Polymer*, *Nano Letters* **13** (June, 2013) 2522–2527.

[12] M. R. Filip, G. E. Eperon, H. J. Snaith, and F. Giustino, *Steric engineering of metal-halide perovskites with tunable optical band gaps*, *Nat. Commun.* **5** (Dec., 2014) ncomms6757.

[13] X. Hong, T. Ishihara, and A. V. Nurmikko, *Dielectric confinement effect on excitons in PbI_4-based layered semiconductors*, *Phys. Rev. B* **45** (Mar., 1992) 6961–6964.

[14] J. Goodman, *Introduction to Fourier Optics*. McGraw-Hill Series in Electrical and Computer Engineering: Communications and Signal Processing. McGraw-Hill, 1996.

[15] J. A. Kurvits, M. Jiang, and R. Zia, *Comparative analysis of imaging configurations and objectives for Fourier microscopy*, *JOSA A* **32** (Nov., 2015) 2082–2092.

[16] R. A. DeCrescent, S. J. Brown, R. A. Schlitz, M. L. Chabinyc, and J. A. Schuller, *Model-blind characterization of thin-film optical constants with momentum-resolved reflectometry*, *Opt. Express* **24** (Dec., 2016) 28842–28857.

[17] R. A. DeCrescent, N. R. Venkatesan, C. J. Dahlman, R. M. Kennard, M. L. Chabinyc, and J. A. Schuller, *Optical Constants and Effective-Medium Origins of Large Optical Anisotropies in Layered Hybrid Organic/Inorganic Perovskites*, *ACS Nano* (Sept., 2019).

[18] S. J. Brown, R. A. Schlitz, M. L. Chabinyc, and J. A. Schuller, *Morphology-dependent optical anisotropies in the n-type polymer P(NDI2od-T2)*, *Phys. Rev. B* **94** (Oct., 2016) 165105.

[19] M. Campoy-Quiles, M. I. Alonso, D. D. C. Bradley, and L. J. Richter, *Advanced Ellipsometric Characterization of Conjugated Polymer Films*,Adv. Funct. Mater., **24**(15), 2116-2134 (2014).

[20] T. Ishihara, J. Takahashi, and T. Goto, *Optical properties due to electronic transitions in two-dimensional semiconductors $(C_nH_{2n+1}NH_3)_2PbI_4$*, *Phys. Rev. B* **42** (Dec., 1990) 11099–11107.

[21] A. Fieramosca, L. De Marco, M. Passoni, L. Polimeno, A. Rizzo, B. L. T. Rosa, G. Cruciani, L. Dominici, M. De Giorgi, G. Gigli, L. C. Andreani, D. Gerace, D. Ballarini, and D. Sanvitto, *Tunable out-of-plane excitons in 2D single-crystal perovskites*, *ACS Photonics* (2018).

[22] G. Hass, *preparation, properties and optical applications of thin films of titanium dioxide*, Vacuum, **2**(4), 331-345 (1952).

[23] B. G. Lewis and D. C. Paine, *Applications and Processing of Transparent Conducting Oxides*, MRS Bulletin, **25**(08), 22-27 (2000).

[24] P. Siciliano, *Preparation, characterisation and applications of thin films for gas sensors prepared by cheap chemical method*, Sensors and Actuators B: Chemical, **70**(1-3), 153-164 (2000).

[25] C. R. Kagan and P. Andry, Thin-Film Transistors. CRC Press (2003).

[26] K. N. Chopra and A. K. Maini, *Thin Films and Their Applications in Military and Civil Sectors*, Defence Research and Development Organization (2010).

[27] P. Peumans, A. Yakimov, and S. R. Forrest, *Small molecular weight organic thin-film photodetectors and solar cells*, Journal of Applied Physics, **93**(7), 3693 (2003).

[28] C. A. Wächter, N. Danz, D. Michaelis, M. Flämmich, S. Kudaev, A. H. Bräuer, M. C. Gather, K. Meerholz, *Intrinsic OLED emitter properties and their effect on device performance*, Proc. SPIE **6910**, Light-Emitting Diodes: Research, Manufacturing, and Applications XII, 691006 (2008).

[29] C. W. Chen, S. Y. Hsiao, C. Y. Chen, H. W. Kang, Z. Y. Huang, and H. W. Lin, *Optical properties of organometal halide perovskite thin films and general device structure design rules for perovskite single and tandem solar cells*, J. Mater. Chem. A, **3**(17), 9152-9159 (2015).

[30] F. L. McCrackin, E. Passaglia, R. R. Stromberg, and H. L. Steinberg, *Measurement of the thickness and refractive index of very thin films and the optical properties of surfaces by ellipsometry*, J. Res. Nat. Bur. Sec. A 67 (1963).

[31] G. E. Jellison Jr., *Generalized ellipsometry for materials characterization*, Thin Solid Films, **450**(1), 42-50 (2004).

[32] G. E. Jellison Jr., V. I. Merkulov, A. A. Puretzky, D. B. Geohegan, G. Eres, D. H. Lowndes, and J. B. Caughman, *Characterization of thin-film amorphous semiconductors using spectroscopic ellipsometry*, Thin Solid Films, **377-378**, 68-73 (2000).

[33] R. A. Synowicki, *Spectroscopic ellipsometry characterization of indium tin oxide film microstructure and optical constants*, Thin Solid Films, **313-314**, 394-397 (1998).

[34] Tompkins, Harland G., *A User's Guide to Ellipsometry*, (Dover Publications, 2006.).

[35] T. E. Jenkins, *Multiple-angle-of-incidence ellipsometry*, Journal of Physics D: Applied Physics, **32**(9), R45 (1999).

[36] M. Campoy-Quiles, P. G. Etchegoin, and D. D. C. Bradley, *On the optical anisotropy of conjugated polymer thin films*, Physical Review B, **72**, 045209 (2005).

[37] G. E. Jellison, *The calculation of thin film parameters from spectroscopic ellipsometry data*, Thin Solid Films, **290-291**, 40-45 (1996).

[38] G. H. Bu-Abbud, *Parameter correlation and precision in multiple-angle ellipsometry*, Appl. Opt., **20**(17), 3020-3026 (1981).

[39] G. H. Bu-Abbud, *Variable Wavelength, Variable Angle Ellipsometry Including a Sensitivities Correlation Test*, Thin Solid Films, **138**(1), 27-41 (1986).

[40] W. A. McGahan, B. Johs, and J. A. Woollam, *Techniques for ellipsometric measurement of the thickness and optical constants of thin absorbing films*, Thin Solid Films, **234**(1), 443-446 (1993).

[41] C. M. Ramsdale and N. C. Greenham, *Ellipsometric Determination of Anisotropic Optical Constants in Electroluminescent Conjugated Polymers*, Adv. Mater., **14**(3), 212-215 (2002).

[42] H. Arwin, M. Poksinski, and K. Johansen, *Total internal reflection ellipsometry: principles and applications*, Applied Optics, **43**(15), 3028-3036 (2004).

[43] D. Poelman and P. F. Smet, *Methods for the determination of the optical constants of thin films from single transmission measurements: a critical review*, Journal of Physics D: Applied Physics, **36**(15), 1850 (2003).

[44] J. I. Cisneros, *Optical characterization of dielectric and semiconductor thin films by use of transmission data*, Applied Optics, **37**(22), 5262-5270 (1998).

[45] Y. Laaziz, A. Bennouna, N. Chahboun, A. Outzourhit, and E. L. Ameziane, *Optical characterization of low optical thickness thin films from transmittance and back reflectance measurements*, Thin Solid Films, **372**(1-2), 149-155 (2000).

[46] M. Flämmich, N. Danz, D. Michaelis, A. Bräuer, M. C. Gather, H.-W. K. Jonas, and K. Meerholz, *Dispersion-model-free determination of optical constants: application to materials for organic thin film devices*, Applied optics, **48**(8), 1507-1513 (2009).

[47] Metricon Corporation, *Model 2010/M Overview*, http://www.metricon.com.

[48] W. Knoll, *Optical Characterization of Organic Thin Films and Interfaces with Evanescent Waves*, MRS Bulletin, **16**(07), 29-39 (1991).

[49] S. J. Bai, R. J. Spry, D. E. Zelmon, U. Ramabadran, and J. Jackson, *Optical anisotropy of polymeric films measured by waveguide propagation mode determination*, J. Polym. Sci. B Polym. Phys., **30**(13), 1507-1514 (1992).

[50] C. J. Takacs, N. D. Treat, S. Krämer, Z. Chen, A. Facchetti, M. L. Chabinyc, and A. J. Heeger, *Remarkable Order of a High-Performance Polymer*, Nano Letters, **13**(6), 2522-2527 (2013).

[51] E. Giussani, D. Fazzi, L. Brambilla, M. Caironi, and C. Castiglioni, *Molecular Level Investigation of the Film Structure of a High Electron Mobility Copolymer via Vibrational Spectroscopy*, Macromolecules, **46**(7), 2658-2670 (2013).

[52] T. Schuettfort, L. Thomsen, and C. R. McNeill, *Observation of a Distinct Surface Molecular Orientation in Films of a High Mobility Conjugated Polymer*, J. Am. Chem. Soc., **135**(3), 1092-1101 (2013).

[53] M. Brinkmann, E. Gonthier, S. Bogen, K. Tremel, S. Ludwigs, M. Hufnagel, and M. Sommer, *Segregated versus Mixed Interchain Stacking in Highly Oriented Films of Naphthalene Diimide Bithiophene Copolymers*, ACS Nano, **6**(11), 10319-10326 (2012).

[54] S. J. Brown, R. A. Schlitz, M. L. Chabinyc, and J. A. Schuller, *Morphology dependent optical anisotropies in the n-type polymer P(NDI2OD-T2)*, Phys. Rev. B **94**, 165105 (2016).

[55] M. K. Debe, *Variable angle spectroscopic ellipsometry studies of oriented phthalocyanine films. II. Copper phthalocyanine*, Journal of Vacuum Science & Technology A: Vacuum, Surfaces, and Films, **10**, 2816 (1992).

[56] O. D. Gordan, M. Friedrich, and D. R. T. Zahn, *The anisotropic dielectric function for copper phthalocyanine thin films*, Organic Electronics, **5**(6), 291-297 (2004).

[57] W. M. P. Jr and D. J. Luca, *The origin of the optical anisotropy of solvent cast polymeric films*, Journal of Applied Physics, **50**(10), 6067-6071 (1979).

[58] C. J. Takacs, S. D. Collins, J. A. Love, A. A. Mikhailovsky, D. Wynands, G. C. Bazan, T.-Q. Nguyen, and A. J. Heeger, *Mapping Orientational Order in a Bulk Heterojunction Solar Cell with Polarization-Dependent Photoconductive Atomic Force Microscopy*, ACS Nano, **8**(8), 8141-8151 (2014).

[59] L. A. A. Pettersson, S. Ghosh, and O. Inganäs, *Optical anisotropy in thin films of poly(3,4-ethylenedioxythiophene)—poly(4-styrenesulfonate)*, Organic Electronics, **3**(3-4), 143-148 (2002).

[60] R. R. Grote, S. J. Brown, J. B. Driscoll, R. M. Osgood, and J. A. Schuller, *Morphology-dependent light trapping in thin-film organic solar cells*, Optics Express, **21**(S5), A847-A863 (2013).

[61] F. Wang, K. Hashimoto, and K. Tajima, *Optical Anisotropy and Strong H-Aggregation of Poly(3-Alkylthiophene) in a Surface Monolayer*, Adv. Mater., **27**(39), 6014-6020 (2015).

[62] M. E. Sykes, A. Barito, J. A. Amonoo, P. F. Green, and M. Shtein, *Broadband Plasmonic Photocurrent Enhancement in Planar Organic Photovoltaics Embedded in a Metallic Nanocavity*, Adv. Energy Mater., **4**, 1301937, (2014).

[63] C. E. Petoukhoff, Z. Shen, M. Jain, A. Chang, and D. M. O'Carroll, *Plasmonic electrodes for bulk-heterojunction organic photovoltaics: a review*, J. Photon. Energy, **5**(1), 057002-057002 (2015).

[64] M. A. Lieb, J. M. Zavislan, and L. Novotny, *Single-molecule orientations determined by direct emission pattern imaging*, J. Opt. Soc. Am. B, **21**(6), 1210-1215 (2004).

[65] J. A. Schuller, S. Karaveli, T. Schiros, K. He, S. Yang, I. Kymissis, J. Shan, and R. Zia, *Orientation of luminescent excitons in layered nanomaterials*, Nature Nanotechnology, **8**(4), 271-276 (2013).

[66] J. A. Kurvits, M. Jiang, and R. Zia, *Comparative analysis of imaging configurations and objectives for Fourier microscopy*, Journal of the Optical Society of America A, **32**(11), 2082 (2015).

[67] A. L. Mattheyses and D. Axelrod, *Fluorescence emission patterns near glass and metal-coated surfaces investigated with back focal plane imaging*, J. Biomed. Opt, **10**(5), 054007 (2005).

[68] T. H. Taminiau, F. D. Stefani, F. B. Segerink, and N. F. van Hulst, *Optical antennas direct single-molecule emission*, Nat Photon, **2**(4), 234-237 (2008).

[69] K. Hassan, A. Bouhelier, T. Bernardin, G. Colas-des-Francs, J.-C. Weeber, A. Dereux, and R. Espiau de Lamaestre, *Momentum-space spectroscopy for advanced analysis of dielectric-loaded surface plasmon polariton coupled and bent waveguides*, Phys. Rev. B, **87**(19), 195428 (2013).

[70] B. Efron and R. Tibshirani, *Bootstrap Methods for Standard Errors, Confidence Intervals, and Other Measures of Statistical Accuracy*, Statistical Science, **1**(1), 54-75 (1986).

[71] SciPy.org, *SciPy v0.17.1 Reference Guide: scipy.optimize.least_squares*, http://docs.scipy.org/doc/scipy/reference/generated/scipy.optimize.least_squares.html.

[72] M. Branch, T. Coleman, and Y. Li, *A Subspace, Interior, and Conjugate Gradient Method for Large-Scale Bound-Constrained Minimization Problems*, SIAM J. Sci. Comput., **21**(1), 1-23 (1999).

[73] M. C. Gurau, D. M. Delongchamp, B. M. Vogel, E. K. Lin, D. A. Fischer, S. Sambasivan, and L. J. Richter, *Measuring Molecular Order in Poly(3-alkylthiophene) Thin Films with Polarizing Spectroscopies*, Langmuir, **23**(2), 834-842 (2007).

[74] X. Song, J. Hu, and H. Zeng, *Two-dimensional semiconductors: Recent progress and future perspectives*, *J. Mater. Chem. C* **1** (Apr., 2013) 2952–2969.

[75] M. Bernardi, C. Ataca, M. Palummo, and J. C. Grossman, *Optical and Electronic Properties of Two-Dimensional Layered Materials*, *Nanophotonics* **6** (2016), no. 2 479–493.

[76] H. Tian, J. Tice, R. Fei, V. Tran, X. Yan, L. Yang, and H. Wang, *Low-symmetry two-dimensional materials for electronic and photonic applications*, *Nano Today* **11** (Dec., 2016) 763–777.

[77] J. S. Ponraj, Z.-Q. Xu, S. C. Dhanabalan, H. Mu, Y. Wang, J. Yuan, P. Li, S. Thakur, M. Ashrafi, K. McCoubrey, Y. Zhang, S. LI, H. Zhang, and Q. Bao, *Photonics and optoelectronics of two-dimensional materials beyond graphene*, *Nanotechnology* **27** (Oct., 2016) 462001.

[78] V. W. Brar, M. C. Sherrott, and D. Jariwala, *Emerging photonic architectures in two-dimensional opto-electronics*, *Chem. Soc. Rev.* **47** (Aug., 2018) 6824–6844.

[79] K. Tanaka and T. Kondo, *Bandgap and exciton binding energies in lead-iodide-based natural quantum-well crystals*, *Sci. Technol. Adv. Mater.* **4** (Jan., 2003) 599–604.

[80] L. Pedesseau, D. Sapori, B. Traore, R. Robles, H.-H. Fang, M. A. Loi, H. Tsai, W. Nie, J.-C. Blancon, A. Neukirch, S. Tretiak, A. D. Mohite, C. Katan, J. Even, and M. Kepenekian, *Advances and Promises of Layered Halide Hybrid Perovskite Semiconductors*, *ACS Nano* **10** (Nov., 2016) 9776–9786.

[81] C. Katan, N. Mercier, and J. Even, *Quantum and Dielectric Confinement Effects in Lower-Dimensional Hybrid Perovskite Semiconductors*, *Chem. Rev.* **119** (Mar., 2019) 3140–3192.

[82] D. G. Billing and A. Lemmerer, *Synthesis, characterization and phase transitions in the inorganic-organic layered perovskite-type hybrids [$(C_nH_{2n+1}NH_3)_2PbI_4$], n = 4, 5 and 6*, *Acta Crystallogr., Sect. B: Struct. Sci.* **63** (Oct., 2007) 735–747.

[83] C. C. Stoumpos, D. H. Cao, D. J. Clark, J. Young, J. M. Rondinelli, J. I. Jang, J. T. Hupp, and M. G. Kanatzidis, *Ruddlesden-Popper Hybrid Lead Iodide Perovskite 2d Homologous Semiconductors*, *Chem. Mater.* **28** (Apr., 2016) 2852–2867.

[84] H. Tsai, W. Nie, J.-C. Blancon, C. C. Stoumpos, R. Asadpour, B. Harutyunyan, A. J. Neukirch, R. Verduzco, J. J. Crochet, S. Tretiak, L. Pedesseau, J. Even, M. A. Alam, G. Gupta, J. Lou, P. M. Ajayan, M. J. Bedzyk, M. G. Kanatzidis, and A. D. Mohite, *High-efficiency two-dimensional Ruddlesden-Popper perovskite solar cells*, *Nature* **536** (Aug., 2016) 312–316.

[85] F. Lédée, G. Trippé-Allard, H. Diab, P. Audebert, D. Garrot, J.-S. Lauret, and E. Deleporte, *Fast growth of monocrystalline thin films of 2d layered hybrid perovskite*, *Crystengcomm* **19** (2017), no. 19 2598–2602.

[86] T. Fujita, Y. Sato, T. Kuitani, and T. Ishihara, *Tunable polariton absorption of distributed feedback microcavities at room temperature*, *Phys. Rev. B* **57** (May, 1998) 12428–12434.

[87] G. Lanty, A. Bréhier, R. Parashkov, J. S. Lauret, and E. Deleporte, *Strong exciton-photon coupling at room temperature in microcavities containing two-dimensional layered perovskite compounds*, *New J. Phys.* **10** (June, 2008) 065007.

[88] O. Yaffe, A. Chernikov, Z. M. Norman, Y. Zhong, A. Velauthapillai, A. Van der Zande, J. S. Owen, and T. F. Heinz, *Excitons in ultrathin organic-inorganic perovskite crystals*, *Phys. Rev. B* **92** (July, 2015) 045414.

[89] L. Dou, A. B. Wong, Y. Yu, M. Lai, N. Kornienko, S. W. Eaton, A. Fu, C. G. Bischak, J. Ma, T. Ding, N. S. Ginsberg, L.-W. Wang, A. P. Alivisatos, and P. Yang, *Atomically thin two-dimensional organic-inorganic hybrid perovskites*, *Science* **349** (Sept., 2015) 1518–1521.

[90] D. H. Cao, C. C. Stoumpos, O. K. Farha, J. T. Hupp, and M. G. Kanatzidis, *2d Homologous Perovskites as Light-Absorbing Materials for Solar Cell Applications*, *J. Am. Chem. Soc.* **137** (June, 2015) 7843–7850.

[91] H. Tsai, W. Nie, J.-C. Blancon, C. C. Stoumpos, C. M. M. Soe, J. Yoo, J. Crochet, S. Tretiak, J. Even, A. Sadhanala, G. Azzellino, R. Brenes, P. M. Ajayan, V. Buloviä, S. D. Stranks, R. H. Friend, M. G. Kanatzidis, and A. D. Mohite, *Stable Light-Emitting Diodes Using Phase-Pure Ruddlesden-Popper Layered Perovskites*, *Adv. Mater.* **30** (Feb., 2018) 1704217.

[92] R. Yang, R. Li, Y. Cao, Y. Wei, Y. Miao, W. L. Tan, X. Jiao, H. Chen, L. Zhang, Q. Chen, H. Zhang, W. Zou, Y. Wang, M. Yang, C. Yi, N. Wang, F. Gao, C. R. Mcneill, T. Qin, J. Wang, and W. Huang, *Oriented Quasi-2d Perovskites for High Performance Optoelectronic Devices*, *Adv. Mater.* **30** (2018), no. 51 1804771.

[93] C. M. Raghavan, T.-P. Chen, S.-S. Li, W.-L. Chen, C.-Y. Lo, Y.-M. Liao, G. Haider, C.-C. Lin, C.-C. Chen, R. Sankar, Y.-M. Chang, F.-C. Chou, and C.-W. Chen, *Low-Threshold Lasing from 2d Homologous Organic-Inorganic Hybrid Ruddlesden-Popper Perovskite Single Crystals*, *Nano Letters* **18** (May, 2018) 3221–3228.

[94] L. Zhang, Y. Liu, Z. Yang, and S. Liu, *Two dimensional metal halide perovskites: Promising candidates for light-emitting diodes*, *J. Energy Chem.* **37** (Oct., 2019) 97–110.

[95] J. A. Woollam, B. D. Johs, C. M. Herzinger, J. N. Hilfiker, R. A. Synowicki, and C. L. Bungay, *Overview of variable-angle spectroscopic ellipsometry (VASE): I. Basic theory and typical applications*, in *Optical Metrology: A Critical Review*, vol. 10294, p. 1029402, International Society for Optics and Photonics, July, 1999.

[96] J. N. Hilfiker, N. Singh, T. Tiwald, D. Convey, S. M. Smith, J. H. Baker, and H. G. Tompkins, *Survey of methods to characterize thin absorbing films with Spectroscopic Ellipsometry*, *Thin Solid Films* **516** (Sept., 2008) 7979–7989.

[97] G. H. Bu-Abbud and N. M. Bashara, *Parameter correlation and precision in multiple-angle ellipsometry*, *Appl. Opt.* **20** (Sept., 1981) 3020–3026.

[98] M. Campoy-Quiles, M. I. Alonso, D. D. C. Bradley, and L. J. Richter, *Advanced Ellipsometric Characterization of Conjugated Polymer Films*, *Adv. Funct. Mater.* **24** (2014), no. 15 2116–2134.

[99] J. A. Schuller, S. Karaveli, T. Schiros, K. He, S. Yang, I. Kymissis, J. Shan, and R. Zia, *Orientation of luminescent excitons in layered nanomaterials*, *Nat. Nanotechnol.* **8** (Mar., 2013) 271–276.

[100] S. J. Brown, R. A. DeCrescent, D. M. Nakazono, S. H. Willenson, N. A. Ran, X. Liu, G. C. Bazan, T.-Q. Nguyen, and J. A. Schuller, *Enhancing Organic Semiconductor-Surface Plasmon Polariton Coupling with Molecular Orientation*, *Nano Letters* **17** (Oct., 2017) 6151–6156.

[101] J. Dong and R. Lu, *Characterization of weakly absorbing thin films by multiple linear regression analysis of absolute unwrapped phase in angle-resolved spectral reflectometry*, *Opt. Express* **26** (Apr., 2018) 12291–12305.

[102] N. R. Venkatesan, J. G. Labram, and M. L. Chabinyc, *Charge-Carrier Dynamics and Crystalline Texture of Layered Ruddlesden-Popper Hybrid Lead Iodide Perovskite Thin Films*, *ACS Energy Lett.* (Jan., 2018) 380–386.

[103] D. Sapori, M. Kepenekian, L. Pedesseau, C. Katan, and J. Even, *Quantum confinement and dielectric profiles of colloidal nanoplatelets of halide inorganic and hybrid organic-inorganic perovskites*, *Nanoscale* **8** (2016), no. 12 6369–6378.

[104] B. Traore, L. Pedesseau, L. Assam, X. Che, J.-C. Blancon, H. Tsai, W. Nie, C. C. Stoumpos, M. G. Kanatzidis, S. Tretiak, A. D. Mohite, J. Even, M. Kepenekian, and C. Katan, *Composite Nature of Layered Hybrid Perovskites: Assessment on Quantum and Dielectric Confinements and Band Alignment*, *ACS Nano* **12** (Apr., 2018) 3321–3332.

[105] T. Ishihara, J. Takahashi, and T. Goto, *Exciton state in two-dimensional perovskite semiconductor* $(c_{10}h_{21}nh_3)_2pbi_4$, *Solid State Commun.* **69** (Mar., 1989) 933–936.

[106] K. Tanaka, F. Sano, T. Takahashi, T. Kondo, R. Ito, and K. Ema, *Two-dimensional Wannier excitons in a layered-perovskite-type crystal* $(C_6H_{13}NH_3)_2PbI_4$, *Solid State Commun.* **122** (May, 2002) 249–252.

[107] J. Even, L. Pedesseau, and M. Kepenekian, *Electronic surface states and dielectric self-energy profiles in colloidal nanoscale platelets of CdSe*, *Phys. Chem. Chem. Phys.* **16** (Oct., 2014) 25182–25190.

[108] M. A. Lieb, J. M. Zavislan, and L. Novotny, *Single-molecule orientations determined by direct emission pattern imaging*, *J. Opt. Soc. Am. B* **21** (2004), no. 6 1210–1215.

[109] R. Scott, J. Heckmann, A. V. Prudnikau, A. Antanovich, A. Mikhailov, N. Owschimikow, M. Artemyev, J. I. Climente, U. Woggon, N. B. Grosse, and A. W. Achtstein, *Directed emission of CdSe nanoplatelets originating from strongly anisotropic 2D electronic structure*, *Nat. Nanotechnol.* **12** (Dec., 2017) 1155–1160.

[110] K. Kikuchi, Y. Takeoka, M. Rikukawa, and K. Sanui, *Structure and optical properties of lead iodide based two-dimensional perovskite compounds containing fluorophenethylamines*, *Current Applied Physics* **4** (Nov., 2004) 599–602.

[111] G. Bastard, *Wave Mechanics Applied to Semiconductor Heterostructures*. EDP SCIENCES, 1988.

[112] P. Guo, W. Huang, C. C. Stoumpos, L. Mao, J. Gong, L. Zeng, B. T. Diroll, Y. Xia, X. Ma, D. J. Gosztola, T. Xu, J. B. Ketterson, M. J. Bedzyk, A. Facchetti, T. J. Marks, M. G. Kanatzidis, and R. D. Schaller, *Hyperbolic Dispersion Arising from Anisotropic Excitons in Two-Dimensional Perovskites*, *Phys. Rev. Lett.* **121** (Sept., 2018) 127401.

[113] V. M. Agranovich and V. E. Kravtsov, *Notes on crystal optics of superlattices*, *Solid State Commun.* **55** (July, 1985) 85–90.

[114] A. Poddubny, I. Iorsh, P. Belov, and Y. Kivshar, *Hyperbolic metamaterials*, *Nat. Photonics* **7** (Dec., 2013) 948–957.

[115] A. Thorne, *Spectrophysics*. Springer Netherlands, 1988.

[116] T. H. Taminiau, S. Karaveli, N. F. Van Hulst, and R. Zia, *Quantifying the magnetic nature of light emission*, *Nat. Commun.* **3** (July, 2012) 979.

[117] A. J. A. El-Haija, *Effective medium approximation for the effective optical constants of a bilayer and a multilayer structure based on the characteristic matrix technique*, *J. Appl. Phys.* **93** (Mar., 2003) 2590–2594.

[118] N. R. Venkatesan, R. M. Kennard, R. A. DeCrescent, H. Nakayama, C. J. Dahlman, E. E. Perry, J. A. Schuller, and M. L. Chabinyc, *Phase Intergrowth and Structural Defects in Organic Metal Halide Ruddlesden-Popper Thin Films*, *Chem. Mater.* **30** (Dec., 2018) 8615–8623.

[119] C. J. Dahlman, A. Agrawal, C. M. Staller, J. Adair, and D. J. Milliron, *Anisotropic Origins of Localized Surface Plasmon Resonance in n-Type Anatase TiO_2 Nanocrystals*, *Chem. Mater.* **31** (Jan., 2019) 502–511.

[120] R. A. DeCrescent, N. R. Venkatesan, C. J. Dahlman, R. M. Kennard, X. Zhang, W. Li, X. Du, M. L. Chabinyc, R. Zia, and J. A. Schuller, *Bright magnetic dipole radiation from two-dimensional lead-halide perovskites*, *Science Advances* **6** (Feb., 2020) eaay4900.

[121] R. Azzam and N. Bashara, *Ellipsometry and Polarized Light*. North-Holland Personal Library. North-Holland Pub. Co., 1977.

[122] v. Y. Aleshkin, B. N. Zvonkov, I. G. Malkina, Y. N. Saf'yanov, A. L. Chernov, and D. O. Filatov, *Polarization of in-plane photoluminescence from InAs/Ga(In)As quantum-well layers grown by metallorganic vapor-phase epitaxy*, *Semiconductors* **32** (1998), no. 10 1119–1124.

[123] H. Masui, H. Yamada, K. Iso, S. Nakamura, and S. P. DenBaars, *Optical polarization characteristics of m-oriented InGaN/GaN light-emitting diodes with various indium compositions in single-quantum-well structure*, *J. Phys. D: Appl. Phys.* **41** (2008), no. 22 225104.

[124] D.-E. Yoon, W. D. Kim, D. Kim, D. Lee, S. Koh, W. K. Bae, and D. C. Lee, *Origin of Shape-Dependent Fluorescence Polarization from CdSe Nanoplatelets*, *J. Phys. Chem. C* **121** (Nov., 2017) 24837–24844.

[125] J. Hu, L.-S. Li, W. Yang, L. Manna, L.-W. Wang, and A. P. Alivisatos, *Linearly Polarized Emission from Colloidal Semiconductor Quantum Rods*, *Science* **292** (June, 2001) 2060–2063.

[126] R. Cowan, *The Theory of Atomic Structure and Spectra*. University of California Press, 1981.

[127] C. M. Dodson and R. Zia, *Magnetic dipole and electric quadrupole transitions in the trivalent lanthanide series: Calculated emission rates and oscillator strengths*, *Phys. Rev. B* **86** (Sept., 2012) 125102.

[128] V. M. Shalaev, *Optical negative-index metamaterials*, *Nat. Photonics* **1** (Jan., 2007) 41.

[129] M. L. Andersen, S. Stobbe, A. S. Srensen, and P. Lodahl, *Strongly modified plasmon-matter interaction with mesoscopic quantum emitters*, *Nat. Phys.* **7** (Mar., 2011) 215–218.

[130] A. Vaskin, S. Mashhadi, M. Steinert, K. E. Chong, D. Keene, S. Nanz, A. Abass, E. Rusak, D.-Y. Choi, I. Fernandez-Corbaton, T. Pertsch, C. Rockstuhl, M. A. Noginov, Y. S. Kivshar, D. N. Neshev, N. Noginova, and I. Staude, *Manipulation of magnetic dipole emission from Eu^{3+} with Mie-resonant dielectric metasurfaces*, *Nano Lett.* **19** (Feb., 2019) 1015–1022.

[131] T. M. Brenner, D. A. Egger, L. Kronik, G. Hodes, and D. Cahen, *Hybrid organic-inorganic perovskites: low-cost semiconductors with intriguing charge-transport properties*, *Nat. Rev. Mater.* **1** (Jan., 2016) 15007.

[132] M. E. Kamminga, H.-H. Fang, M. R. Filip, F. Giustino, J. Baas, G. R. Blake, M. A. Loi, and T. T. M. Palstra, *Confinement Effects in Low-Dimensional Lead Iodide Perovskite Hybrids*, *Chem. Mater.* **28** (July, 2016) 4554–4562.

[133] D. N. Congreve, M. C. Weidman, M. Seitz, W. Paritmongkol, N. S. Dahod, and W. A. Tisdale, *Tunable light-emitting diodes utilizing quantum-confined layered perovskite emitters*, *ACS Photonics* **4** (Mar., 2017) 476–481.

[134] X. Yang, X. Zhang, J. Deng, Z. Chu, Q. Jiang, J. Meng, P. Wang, L. Zhang, Z. Yin, and J. You, *Efficient green light-emitting diodes based on quasi-two-dimensional composition and phase engineered perovskite with surface passivation*, *Nat. Commun.* **9** (Feb., 2018) 570.

[135] D. B. Mitzi, *Synthesis, crystal structure, and optical and thermal properties of $(C_4H_9NH_3)_2MI_4$ (M = Ge, Sn, Pb)*, *Chem. Mater.* **8** (Jan., 1996) 791–800.

[136] K. Gauthron, J.-S. Lauret, L. Doyennette, G. Lanty, A. A. Choueiry, S. J. Zhang, A. Brehier, L. Largeau, O. Mauguin, J. Bloch, and E. Deleporte, *Optical spectroscopy of two-dimensional layered $(C_6H_5C_2H_4\text{-}NH_3)_2\text{-}PbI_4$ perovskite*, *Opt. Express* **18** (Mar., 2010) 5912–5919.

[137] M. D. Smith and H. I. Karunadasa, *White-Light Emission from Layered Halide Perovskites*, *Acc. Chem. Res.* **51** (Mar., 2018) 619–627.

[138] J.-C. Blancon, A. v. Stier, H. Tsai, W. Nie, C. C. Stoumpos, B. Traor, L. Pedesseau, M. Kepenekian, F. Katsutani, G. T. Noe, J. Kono, S. Tretiak, S. A. Crooker, C. Katan, M. G. Kanatzidis, J. J. Crochet, J. Even, and A. D. Mohite, *Scaling law for excitons in 2d perovskite quantum wells*, *Nat. Commun.* **9** (June, 2018) 2254.

[139] B. Wu, H. Yuan, Q. Xu, J. A. Steele, D. Giovanni, P. Puech, J. Fu, Y. F. Ng, N. F. Jamaludin, A. Solanki, S. Mhaisalkar, N. Mathews, M. B. J. Roeffaers, M. Grtzel, J. Hofkens, and T. C. Sum, *Indirect tail states formation by thermal-induced polar fluctuations in halide perovskites*, *Nat. Commun.* **10** (Jan., 2019) 484.

[140] K. Tanaka, T. Takahashi, T. Kondo, K. Umeda, K. Ema, T. Umebayashi, K. Asai, K. Uchida, and N. Miura, *Electronic and excitonic structures of inorganic-organic perovskite-type quantum-well crystal $(C_4H_9NH_3)_2PbBr_4$*, *Jpn. J. Appl. Phys.* **44** (Aug., 2005) 5923.

[141] J. Even, L. Pedesseau, M.-A. Dupertuis, J.-M. Jancu, and C. Katan, *Electronic model for self-assembled hybrid organic/perovskite semiconductors: Reverse band edge electronic states ordering and spin-orbit coupling*, *Phys. Rev. B* **86** (Nov., 2012) 205301.

[142] M. A. Becker, R. Vaxenburg, G. Nedelcu, P. C. Sercel, A. Shabaev, M. J. Mehl, J. G. Michopoulos, S. G. Lambrakos, N. Bernstein, J. L. Lyons, T. Stferle, R. F. Mahrt, M. V. Kovalenko, D. J. Norris, G. Rain, and A. L. Efros, *Bright triplet excitons in caesium lead halide perovskites*, *Nature* **553** (Jan., 2018) 189–193.

[143] W. K. Chong, K. Thirumal, D. Giovanni, T. W. Goh, X. Liu, N. Mathews, S. Mhaisalkar, and T. C. Sum, *Dominant factors limiting the optical gain in layered two-dimensional halide perovskite thin films*, *Phys. Chem. Chem. Phys.* **18** (May, 2016) 14701–14708.

[144] D. B. Straus, S. Hurtado Parra, N. Iotov, J. Gebhardt, A. M. Rappe, J. E. Subotnik, J. M. Kikkawa, and C. R. Kagan, *Direct observation of electron-phonon coupling and slow vibrational relaxation in organic-inorganic hybrid perovskites*, *J. Am. Chem. Soc.* **138** (Oct., 2016) 13798–13801.

[145] S. Neutzner, F. Thouin, D. Cortecchia, A. Petrozza, C. Silva, and A. R. Srimath Kandada, *Exciton-polaron spectral structures in two-dimensional hybrid lead-halide perovskites*, *Phys. Rev. Mater.* **2** (June, 2018) 064605.

[146] M. Kepenekian and J. Even, *Rashba and Dresselhaus couplings in halide perovskites: Accomplishments and opportunities for spintronics and spin-orbitronics*, *J. Phys. Chem. Lett.* **8** (July, 2017) 3362–3370.

[147] X. Zhang, J.-X. Shen, W. Wang, and C. G. Van de Walle, *First-principles analysis of radiative recombination in lead-halide perovskites*, *ACS Energy Lett.* **3** (Oct., 2018) 2329–2334.

[148] D. Niesner, M. Hauck, S. Shrestha, I. Levchuk, G. J. Matt, A. Osvet, M. Batentschuk, C. Brabec, H. B. Weber, and T. Fauster, *Structural fluctuations cause spin-split states in tetragonal (CH_3NH_3)PbI_3 as evidenced by the circular photogalvanic effect*, *PNAS* **115** (Sept., 2018) 9509–9514.

[149] C. Zheng, S. Yu, and O. Rubel, *Structural dynamics in hybrid halide perovskites: Bulk Rashba splitting, spin texture, and carrier localization*, *Phys. Rev. Mater.* **2** (Nov., 2018) 114604.

[150] S. Karaveli, S. Wang, G. Xiao, and R. Zia, *Time-resolved energy-momentum spectroscopy of electric and magnetic dipole transitions in Cr^{3+}:MgO*, *ACS Nano* **7** (Aug., 2013) 7165–7172.

[151] G. Wang, C. Robert, M. Glazov, F. Cadiz, E. Courtade, T. Amand, D. Lagarde, T. Taniguchi, K. Watanabe, B. Urbaszek, and X. Marie, *In-Plane Propagation of Light in Transition Metal Dichalcogenide Monolayers: Optical Selection Rules*, *Phys. Rev. Lett.* **119** (July, 2017) 047401.

[152] S. Cueff, D. Li, Y. Zhou, F. J. Wong, J. A. Kurvits, S. Ramanathan, and R. Zia, *Dynamic control of light emission faster than the lifetime limit using VO_2 phase-change*, *Nat. Commun.* **6** (Oct., 2015) 8636.

[153] C. M. Iaru, J. J. Geuchies, P. M. Koenraad, D. Vanmaekelbergh, and A. Y. Silov, *Strong carrier-phonon coupling in lead halide perovskite nanocrystals*, *ACS Nano* **11** (Nov., 2017) 11024–11030.

[154] S. Sugano, Y. Tanabe, and H. Kamimura, *Multiplets of Transition-metal Ions in Crystals*. Academic Press, 1970.

[155] M. E. Kamminga, H.-H. Fang, M. A. Loi, G. H. ten Brink, G. R. Blake, T. T. M. Palstra, and J. E. ten Elshof, *Micropatterned 2D hybrid perovskite thin films with enhanced photoluminescence lifetimes*, *ACS Appl. Mater. Interfaces* **10** (Apr., 2018) 12878–12885.

[156] P. R. Bunker and P. Jensen, *Molecular Symmetry and Spectroscopy, 2nd Ed.* NRC Research Press, Jan., 2006.

[157] D. Cortecchia, J. Yin, A. Bruno, S.-Z. A. Lo, G. G. Gurzadyan, S. Mhaisalkar, J.-L. Brdas, and C. Soci, *Polaron self-localization in white-light emitting hybrid perovskites*, *J. Mater. Chem. C* **5** (Mar., 2017) 2771–2780.

[158] D. Rossi, H. Wang, Y. Dong, T. Qiao, X. Qian, and D. H. Son, *Light-induced activation of forbidden exciton transition in strongly confined perovskite quantum dots*, *ACS Nano* **12** (2018), no. 12 12436–12443.

[159] X. Wang, W. Meng, W. Liao, J. Wang, R.-G. Xiong, and Y. Yan, *Atomistic mechanism of broadband emission in metal halide perovskites*, *J. Phys. Chem. Lett.* **10** (2019), no. 3 501–506.

[160] K. Noba and Y. Kayanuma, *Model for self-trapping of excitons with internal degrees of freedom*, *J. Phys. Soc. Jpn.* **67** (2010), no. 10 3388–3391.

[161] S. Messerschmidt, A. Krampf, F. Freytag, M. Imlau, L. Vittadello, M. Bazzan, and G. Corradi, *The role of self-trapped excitons in polaronic recombination processes in lithium niobate*, *J. Phys.: Condens. Matter* **31** (Dec., 2018) 065701.

[162] E. Poem, Y. Kodriano, C. Tradonsky, N. H. Lindner, B. D. Gerardot, P. M. Petroff, and D. Gershoni, *Accessing the dark exciton with light*, *Nat. Phys.* **6** (Dec., 2010) 993–997.

[163] N. A. Butakov and J. A. Schuller, *Designing multipolar resonances in dielectric metamaterials*, *Sci. Rep.* **6** (Dec., 2016) 38487.

[164] R. Verre, D. G. Baranov, B. Munkhbat, J. Cuadra, M. Kll, and T. Shegai, *Transition metal dichalcogenide nanodisks as high-index dielectric Mie nanoresonators*, *Nat. Nanotechnol.* **14** (July, 2019) 679–683.

[165] T. H. Taminiau, F. D. Stefani, F. B. Segerink, and N. F. van Hulst, *Optical antennas direct single-molecule emission*, *Nature Photonics* **2** (Mar., 2008) 234–237.

[166] A. Curto, *Unidirectional Emission of a Quantum Dot Coupled to a Nanoantenna*, *Science* **329** (2010), no. 5994 930–933.

[167] S. Liu, A. Vaskin, S. Addamane, B. Leung, M.-C. Tsai, Y. Yang, P. P. Vabishchevich, G. A. Keeler, G. Wang, X. He, Y. Kim, N. F. Hartmann, H. Htoon, S. K. Doorn, M. Zilk, T. Pertsch, G. Balakrishnan, M. B. Sinclair, I. Staude, and I. Brener, *Light-Emitting Metasurfaces: Simultaneous Control of Spontaneous Emission and Far-Field Radiation*, *Nano Letters* **18** (Nov., 2018) 6906–6914.

[168] J. Gu, B. Chakraborty, M. Khatoniar, and V. M. Menon, *A room-temperature polariton light-emitting diode based on monolayer WS2*, *Nature Nanotechnology* **14** (Nov., 2019) 1024–1028.

[169] R. Su, S. Ghosh, J. Wang, S. Liu, C. Diederichs, T. C. H. Liew, and Q. Xiong, *Observation of exciton polariton condensation in a perovskite lattice at room temperature*, *Nature Physics* (Jan., 2020).

[170] J. Heckmann, R. Scott, A. V. Prudnikau, A. Antanovich, N. Owschimikow, M. Artemyev, J. I. Climente, U. Woggon, N. B. Grosse, and A. W. Achtstein, *Directed Two-Photon Absorption in CdSe Nanoplatelets Revealed by k -Space Spectroscopy*, *Nano Letters* **17** (Oct., 2017) 6321–6329.

[171] H. Budde, N. Coca-Lpez, X. Shi, R. Ciesielski, A. Lombardo, D. Yoon, A. C. Ferrari, and A. Hartschuh, *Raman Radiation Patterns of Graphene*, *ACS Nano* **10** (Feb., 2016) 1756–1763.

[172] M. Kasperczyk, S. Person, D. Ananias, L. D. Carlos, and L. Novotny, *Excitation of Magnetic Dipole Transitions at Optical Frequencies*, *Physical Review Letters* **114** (Apr., 2015) 163903.

[173] O. Levy and D. Stroud, *Maxwell Garnett theory for mixtures of anisotropic inclusions: Application to conducting polymers*, *Phys. Rev. B* **56** (Oct., 1997) 8035–8046.

[174] A. Lemmerer and D. G.Billing, *Synthesis, characterization and phase transitions of the inorganic-organic layered perovskite-type hybrids [$(c_nh_{2n+1}nh_3)_2pbi_4$], n = 7, 8, 9 and 10*, *Dalton Transactions* **41** (2012), no. 4 1146–1157.